The Astrophysical Journal Supplement Series, 244:39 (37pp), 2019 October https://doi.org/10.3847/1538-4365/ab40b6

PEXO: A Global Modeling Framework for Nanosecond Timing, Microarcsecond Astrometry, and μm s^{-1} Radial Velocities

Fabo Feng[1,2], Maksym Lisogorskyi[2], Hugh R. A. Jones[2], Sergei M. Kopeikin[3], R. Paul Butler[1], Guillem Anglada-Escudé[4], and Alan P. Boss[1]

[1] Department of Terrestrial Magnetism, Carnegie Institution of Washington, Washington, DC 20015, USA; ffeng@carnegiescience.edu
[2] Centre for Astrophysics Research, University of Hertfordshire, College Lane, AL10 9AB, Hatfield, UK
[3] Department of Physics & Astronomy, University of Missouri, Columbia, Missouri 65211, USA
[4] School of Physics and Astronomy, Queen Mary University of London, 327 Mile End Road, E1 4NS, London, UK
Received 2019 April 4; revised 2019 August 24; accepted 2019 August 30; published 2019 October 15

Abstract

The ability to make independent detections of the signatures of exoplanets with complementary telescopes and instruments brings a new potential for robust identification of exoplanets and precision characterization. We introduce PEXO, a package for Precise EXOplanetology to facilitate the efficient modeling of timing, astrometry, and radial velocity data, which will benefit not only exoplanet science but also various astrophysical studies in general. PEXO is general enough to account for binary motion and stellar reflex motions induced by planetary companions and is precise enough to treat various relativistic effects both in the solar system and in the target system. We also model the post-Newtonian barycentric motion for future tests of general relativity in extrasolar systems. We benchmark PEXO with the pulsar timing package TEMPO2 and find that PEXO produces numerically similar results with timing precision of about 1 ns, space-based astrometry to a precision of 1 μas, and radial velocity of 1 μm s^{-1} and improves on TEMPO2 for decade-long timing data of nearby targets, due to its consideration of third-order terms of Roemer delay. PEXO is able to avoid the bias introduced by decoupling the target system and the solar system and to account for the atmospheric effects that set a practical limit for ground-based radial velocities close to 1 cm s^{-1}. Considering the various caveats in barycentric correction and ancillary data Required to realize cm s^{-1} modeling, we recommend the preservation of original observational data. The PEXO modeling package is available at GitHub (https://github.com/phillippro/pexo) and Zenodo (Feng et al. 2019).

Key words: astrometry – ephemerides – relativistic processes – stars: general – techniques: radial velocities – time

1. Introduction

The first decades of exoplanet science have enabled detection and some characterization of exoplanets with a much wider range of properties than anticipated. In turn, this has prompted a reinvention of the formation history of the solar system. However, so far we barely have the capability to be sensitive to the planetary systems, like our own solar system, around nearby stars. New high-precision facilities such as *TESS* (Ricker et al. 2014), *Gaia* (*Gaia* Collaboration et al. 2018), ESPRESSO (González Hernández et al. 2018), and the upcoming *James Webb Space Telescope* (Beichman et al. 2014) bring us to a golden age of exoplanet science where a comprehensive survey of nearby planets becomes feasible and discoveries of nearby Earth-like planets around Sun-like stars (or "Earth twins") become possible. This in turn leads to the ability to detect biosignatures and begin habitability studies and to test planet formation theories. The high precision and overlapping constraints afforded by these new instruments might also suffice for tests of relativity theory (Jordán & Bakos 2008; Mignard & Klioner 2010) analogous to that achieved for pulsar timing (Hulse & Taylor 1975; Weisberg & Taylor 2005; Wex 2014). For example, short-period binaries on eccentric orbits would show strong variation of gravitational Doppler shift.

Five primary methods are used to detect exoplanets: radial velocity, transit, astrometry, microlensing, and direct imaging. We classify these methods into four categories according to the dimension of the data used in them. Modern instruments produce timing, photometric, spectroscopic, and astrometric data. The radial velocity method uses the timing and spectroscopic data; the transit method uses the timing and photometry data; the astrometry method uses the timing and astrometry data; the microlensing method uses the timing and photometry or spectroscopic data; direct imaging typically uses all four types of data. Thus, a general model for exoplanet detection would require a precise modeling of timing, photometry, astrometry, and spectroscopy. Considering that radial velocity and transits are the main working methods for exoplanet detection and the astrometry method will probably be used to find thousands of exoplanets by *Gaia* (Perryman et al. 2014), the immediate need for general and combined analysis of precision exoplanet data is a combined model of timing, radial velocity, and astrometry. In the pulsar timing community, TEMPO2 (Edwards et al. 2006, here "E06"; Hobbs et al. 2006) is currently the only known package used to test general relativity (GR) and indirectly detect gravitational waves due to its unprecedented timing precision at a level of a nanosecond (ns). However, a similar high-precision package is not available for independent pulsar timing analysis and for the search for exoplanets despite various efforts being made to improve the precision in some special cases (Eastman et al. 2010; Wright & Eastman 2014).

In this work, we introduce a new package called "PEXO"[5] to model the timing, radial velocity, and astrometry simultaneously and precisely in order to detect and characterize small

[5] PEXO is an acronym for Precise EXOplanetology.

planets such as Earth twins and test GR. PEXO is able to model timing to a precision of about 1 ns, radial velocity to a precision of 1 μm s^{-1}, and space-based astrometry to a precision of 1 μas. PEXO models the motion of the target star around the target system barycenter (TSB) due to its companion (so-called "reflex motion"), heliocentric motion of the TSB, and the Earth's motion simultaneously to avoid any bias caused by decoupling and separating these motions. PEXO can be used for combined analysis of timing, radial velocity, and astrometry data and to determine the orbital parameters of potential companions, as well as refining the astrometric parameters and the motion of the observing instrument with respect to the barycenter of the solar system. PEXO is also able to model the relativistic effects in the binary motion and thus is able to test GR in systems with multiple stars and companions.

PEXO is developed in particular to address the following issues in previous exoplanet packages and studies:

1. The decoupling of remote and local effects or the so-called "barycentric correction," though efficient for single stars hosting planets, is not appropriate for detection of low-mass planets around stars with massive companions. We will discuss this issue in Section 3.5.
2. The exoplanet community might be more focused on exoplanet detection and characterization than tests of GR, although the classical astrometric effects induced by small planets could be comparable to relativistic effects. In Section 3.6, we address this issue by proposing the companion-induced gravitational redshift as a unique way to test gravity theories.
3. The relativistic effects in extrasolar systems are not well modeled, leading to potential bias in transit timing variation and radial velocity detection of exoplanets. This issue will be addressed in Section 5.1.
4. The current packages are not able to analyze multiple types of exoplanet data in a consistent way, due to a lack of simultaneous modeling of timing, radial velocity, photometry, and astrometry. We will briefly discuss this problem in Section 5.4.

This paper is structured as follows. In Section 2, we introduce the geometric and kinematic model of astrometry and radial velocity. We then introduce the relativistic effects in timing, astrometry, and radial velocity in Section 3. We compare PEXO with TEMPO2 and other packages to examine the precision of PEXO in Section 4. This is followed by assessments of the significance of various relativistic effects on a few key nearby objects using two example transit systems and α Centauri A and B in Section 5. Finally we conclude in Section 6.

2. Geometric and Kinematic Model of Astrometry and Radial Velocity

We follow the *Hipparcos* and *Gaia* team (ESA 1997; Lindegren et al. 2012) and use vectors to model astrometry. In this section, we assume that the speed of light is infinite and ignore the relativistic effects on the light rays. In other words, we consider the kinematics and geometry of stars and observers. We show the propagation of light in Figure 1. As we develop the model, the elements are described, though there are many of these, so we also provide a tabulation in the appendix.

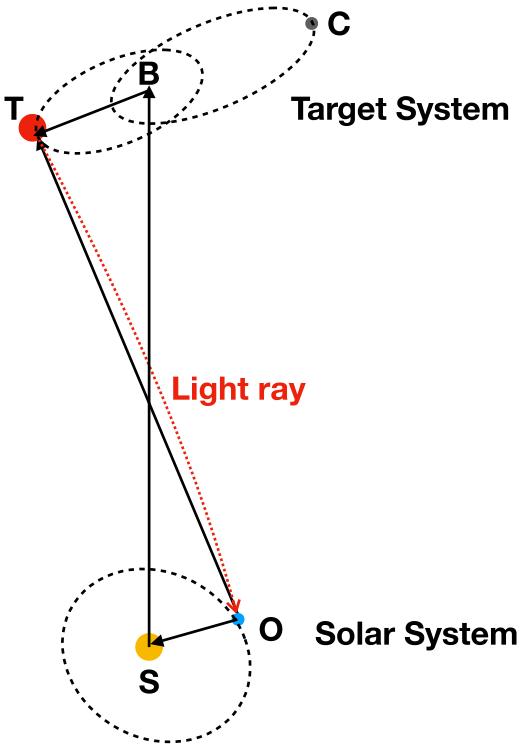

Figure 1. Illustration of the propagation of a photon vastly exaggerated in order to represent the underlying geometry of the model. A photon emitted from the target star (T) is delayed and deflected by other bodies in the target system with barycenter at B and deflected and delayed by solar system bodies with barycenter at S before arriving at the observation site (O). The companion in the target system is denoted by C. The vectors in the diagram are related according to $\boldsymbol{r}_{\rm OT} = \boldsymbol{r}_{\rm OB} + \boldsymbol{r}_{\rm BT}$ and $\boldsymbol{r}_{\rm OB} = \boldsymbol{r}_{\rm OS} + \boldsymbol{r}_{\rm SB}$. The time derivatives of these vectors are corresponding velocities, which are related in the same way.

2.1. Astrometry Model

The observed position of the target star is

$$\boldsymbol{r}_{\rm OT} = \boldsymbol{r}_{\rm OS} + \boldsymbol{r}_{\rm SB} + \boldsymbol{r}_{\rm BT}, \tag{1}$$

where $\boldsymbol{r}_{\rm OS}$ is the position of the solar system barycenter (SSB) with respect to the observer, $\boldsymbol{r}_{\rm SB}$ is the position of the TSB with respect to the SSB, and $\boldsymbol{r}_{\rm BT}$ is the target star with respect to the TSB. We also define the opposite of these vectors as $\boldsymbol{r}_{\rm TO} = -\boldsymbol{r}_{\rm OT}$, $\boldsymbol{r}_{\rm SO} = -\boldsymbol{r}_{\rm OS}$, $\boldsymbol{r}_{\rm BS} = -\boldsymbol{r}_{\rm SB}$, and $\boldsymbol{r}_{\rm TB} = -\boldsymbol{r}_{\rm BT}$. In the following sections, the variable in bold is a vector, while the variable in normal font is a scalar or the mode of the corresponding vector. Denoting the velocity of the TSB relative to the SSB as $\boldsymbol{v}_{\rm SB}$ and assuming $\boldsymbol{v}_{\rm SB}$ to be constant, that is, $\boldsymbol{v}_{\rm SB}(t) = \boldsymbol{v}_{\rm SB}(t_0)$, we find that Equation (1) becomes

$$\begin{aligned}\boldsymbol{r}_{\rm OT}(t) = {} & \boldsymbol{v}_{\rm SB}(t_0)(t - t_0) + \boldsymbol{r}_{\rm SB}(t_0) \\ & + \boldsymbol{r}_{\rm BT}(t) - \boldsymbol{r}_{\rm SO}(t),\end{aligned} \tag{2}$$

where t_0 is a reference time. Here, $\boldsymbol{r}_{\rm BT}$ is determined by the motion of the target star around the TSB (or reflex motion), and $\boldsymbol{r}_{\rm SO}$ is determined by the ephemeris of the observer.

Considering that $\boldsymbol{v}_{\rm SB}(t_0)$ and $\boldsymbol{r}_{\rm SB}(t_0)$ are provided by astrometric observations, we replace them with astrometry, and Equation (2) becomes

$$\begin{aligned}\boldsymbol{r}_{\rm OT}(t) = {} & \boldsymbol{r}_{\rm SB}(t_0) + \frac{A}{\widetilde{\omega}^b}(\boldsymbol{p}_b \mu_\alpha^b + \boldsymbol{q}_b \mu_\delta^b \\ & + \boldsymbol{u}_b \mu_r^b)(t - t_0) + \boldsymbol{r}_{\rm BT}(t) - \boldsymbol{r}_{\rm SO}(t),\end{aligned} \tag{3}$$

where the relevant notations are defined as follows: $\boldsymbol{u}_b$ is the Barycentric Celestial Reference System (BCRS; Rickman 2001) coordinate direction to the TSB at the reference TCB epoch t_0; α^b is the BCRS R.A. of the TSB at the reference epoch; δ^b is the BCRS decl. of the TSB at the reference epoch; ϖ^b is the annual parallax of the TSB at the reference epoch; μ_α^b is the proper motion in R.A. of the TSB at the reference epoch; μ_δ^b is the proper motion in decl. of the TSB at the reference epoch; $\boldsymbol{\mu} = \boldsymbol{p}_b\mu_\alpha^b + \boldsymbol{q}_b\mu_\delta^b$ is the total proper motion of the TSB at the reference epoch; $\mu_r^b = v_r^b\varpi^b/A$ is the so-called "radial proper motion" of the TSB at the reference epoch, where v_r is the radial velocity of the TSB and A is the astronomical unit; the unit vectors of $\boldsymbol{p}_b$, $\boldsymbol{q}_b$, and $\boldsymbol{u}_b$ form a triad, which is

$$[\boldsymbol{p}_b \quad \boldsymbol{q}_b \quad \boldsymbol{u}_b] = \begin{bmatrix} -\sin\alpha^b & -\sin\delta^b\cos\alpha^b & \cos\delta^b\cos\alpha^b \\ \cos\alpha^b & -\sin\delta^b\sin\alpha^b & \cos\delta^b\sin\alpha^b \\ 0 & \cos\delta^b & \sin\delta^b \end{bmatrix}. \quad (4)$$

Here, $\boldsymbol{p}_b$ and $\boldsymbol{q}_b$ are respectively the unit vectors in the directions of increasing α and δ at the reference epoch. The coordinate system determined by the triad $[\boldsymbol{p}_b\ \boldsymbol{q}_b\ \boldsymbol{u}_b]$ is illustrated in Figure 2.

Because astrometric observations measure the direction of a star on the sky, we estimate the observed direction of a star $\hat{\boldsymbol{u}}_o$ from Equation (3), following ESA (1997) and Lindegren et al. (2012):

$$\boldsymbol{u}_{\rm OT}(t) = \langle \boldsymbol{u}_b + (\boldsymbol{p}_b\mu_\alpha^b + \boldsymbol{q}_b\mu_\delta^b + \boldsymbol{u}_b\mu_r^b)(t - t_0) + [\boldsymbol{r}_{\rm BT}(t) - \boldsymbol{r}_{\rm SO}(t)]\varpi^b/A\rangle, \quad (5)$$

where the angular brackets denote vector normalization. Similarly, the BCRS direction of the TSB is

$$\boldsymbol{u}_{\rm SB}(t) = \langle \boldsymbol{u}_b + (\boldsymbol{p}_b\mu_\alpha^b + \boldsymbol{q}_b\mu_\delta^b + \boldsymbol{u}_b\mu_r^b)(t - t_0)\rangle, \quad (6)$$

and the BCRS direction of the target star is

$$\boldsymbol{u}_{\rm ST}(t) = \langle \boldsymbol{u}_b + (\boldsymbol{p}_b\mu_\alpha^b + \boldsymbol{q}_b\mu_\delta^b + \boldsymbol{u}_b\mu_r^b)(t - t_0) + \boldsymbol{r}_{\rm BT}(t)\varpi^b/A\rangle. \quad (7)$$

The only difference between Equation (5) in this paper and the one in Equation (4) of Lindegren et al. (2012) is the inclusion of stellar reflex motion.

Although a robust model of astrometry is typically expressed with vectors, one is typically interested in the variation of the sky position of a star rather than its absolute position. To model the astrometry relative to a reference epoch, we follow ESA (1997) to project the position of a component relative to the TSB onto the offset coordinates (ξ, η), which are defined as rectangular coordinates in the tangent plane at the reference point $\boldsymbol{r}_{\rm SB}(t_0)$, with ξ and η increasing in the directions of $\boldsymbol{p}_b$ and $\boldsymbol{q}_b$. The offset of the target with respect to the TSB in the topocentric reference frame is

$$\sin\xi(t) = \frac{\mu_\alpha^b(t - t_0) + \boldsymbol{p}_b \cdot [\boldsymbol{r}_{\rm BT}(t) - \boldsymbol{r}_{\rm SO}(t)]\varpi^b/A}{1 + \mu_r^b(t - t_0) + \boldsymbol{u}_b \cdot [\boldsymbol{r}_{\rm BT}(t) - \boldsymbol{r}_{\rm SO}(t)]\varpi^b/A},$$
$$\sin\eta(t) = \frac{\mu_\delta^b(t - t_0) + \boldsymbol{q}_b \cdot [\boldsymbol{r}_{\rm BT}(t) - \boldsymbol{r}_{\rm SO}(t)]\varpi^b/A}{1 + \mu_r^b(t - t_0) + \boldsymbol{u}_b \cdot [\boldsymbol{r}_{\rm BT}(t) - \boldsymbol{r}_{\rm SO}(t)]\varpi^b/A}. \quad (8)$$

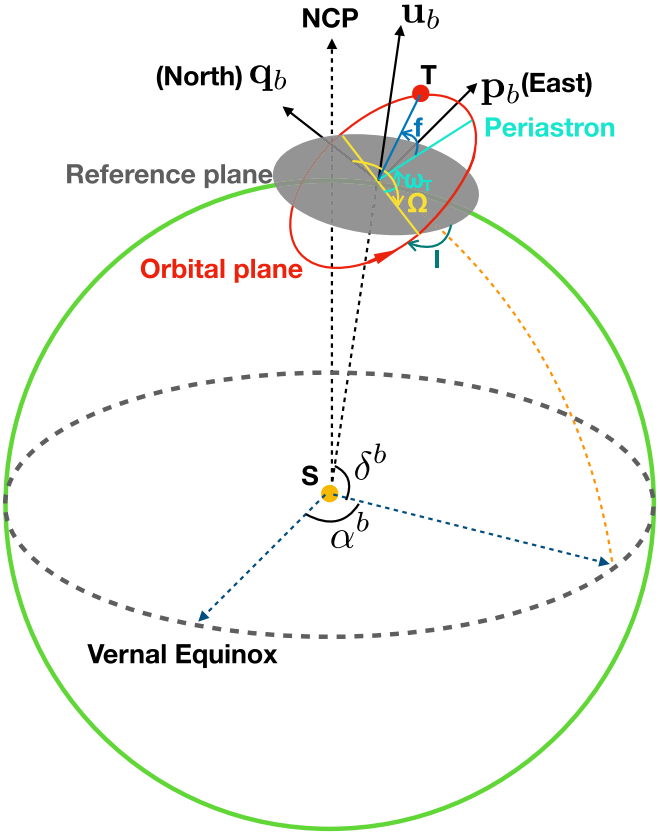

Figure 2. Illustration of the binary motion in the sky-plane reference frame defined by the triad $[\boldsymbol{p}_b\ \boldsymbol{q}_b\ \boldsymbol{u}_b]$. This coordinate system is fixed at the reference epoch and does not rotate as the TSB moves with respect to the Sun. In the orbital-plane coordinate system, the x axis $\boldsymbol{e}_x$ points to the periastron, the y axis $\boldsymbol{e}_y$ is 90° in the direction of orbital motion from $\boldsymbol{e}_y$ in the orbital plane, and the z axis $\boldsymbol{e}_z$ is perpendicular to the orbital plane (parallel to the angular momentum). The three axes form a right-handed Cartesian coordinate system. Here, $\boldsymbol{q}_b$ points to the north while $\boldsymbol{p}_b$ points to the east from the barycentric observer's perspective. The reflex motion of the target star T is determined by the five orbital elements: semimajor axis $a_{\rm T}$, eccentricity e, inclination I (the angle between $-\boldsymbol{u}_b$ and the angular momentum), longitude of ascending node Ω (counterclockwise angle from the north to the ascending node viewed from the observer), and argument of periastron $\omega_{\rm T}$. The true anomaly f is needed to determine the location of the target star. For the orbit of a companion around the barycenter, the semimajor axis is $a_C = \frac{m_T}{m_C}a_T$, where $m_{\rm T}$ and m_C are respectively the masses of the target and the companion. The argument of periastron is $\omega_C = \omega_{\rm T} + \pi$, while the other orbital elements are the same as the reflex orbit of the target star. We call the convention illustrated by this figure the "astrometric convention." This and other conventions of binary motion and the transformation between the orbital-plane frame and the sky-plane frame are explained in detail in Appendix A. According to Equation (4), the sky-plane system can be further transformed into the equatorial coordinate system defined by the Vernal Equinox and the North Celestial Pole (NCP).

In the above equation, $\sin\xi(t)$ and $\sin\eta(t)$ differ from $\xi(t)$ and $\eta(t)$ by about 0.2 mas over 100 yr for the case of α Centauri. The above formula differs from Equation (1.2.26) of ESA (1997) in terms of the consideration of the stellar reflex motion and the use of the sinusoidal function for offset coordinates. Although the companion-induced offset is small, the integration of this offset over time would strongly bias the predicted position of a star. While Equation (8) can provide high-precision geometric modeling in offset coordinates, we need to model absolute astrometry to account for relativistic effects. Thus we model the geometric astrometry in the equatorial coordinate system using Equation (5). We then consider

relativistic effects (Section 3) to form the full astrometry model. This model is formulated in the offset coordinates according to Equation (8) if the astrometric data are given in the offset coordinate system.

To compare Equation (8) with the astrometry model in previous studies, we expand the offsets to second order in a Taylor series. Because all terms in the equations are small quantities compared with 1, the second-order Taylor expansion is

$$\begin{aligned}\xi(t) &= \mu_\alpha^b(t-t_0) + \boldsymbol{p}_b\cdot\boldsymbol{R} - \mu_\alpha^b\mu_r^b(t-t_0)^2 - [\mu_\alpha^b\boldsymbol{u}_b\cdot\boldsymbol{R} \\ &\quad + \mu_r^b\boldsymbol{p}_b\cdot\boldsymbol{R}](t-t_0) - (\boldsymbol{p}_b\cdot\boldsymbol{R})(\boldsymbol{u}_b\cdot\boldsymbol{R}) + \mathcal{O}(\xi^3), \\ \eta(t) &= \mu_\delta^b(t-t_0) + \boldsymbol{q}_b\cdot\boldsymbol{R} - \mu_\delta^b\mu_r^b(t-t_0)^2 - [\mu_\delta^b\boldsymbol{u}_b\cdot\boldsymbol{R} \\ &\quad + \mu_r^b\boldsymbol{q}_b\cdot\boldsymbol{R}](t-t_0) - (\boldsymbol{q}_b\cdot\boldsymbol{R})(\boldsymbol{u}_b\cdot\boldsymbol{R}) + \mathcal{O}(\eta^3),\end{aligned} \tag{9}$$

where $\boldsymbol{R} \equiv [\boldsymbol{r}_{\rm BT}(t) - \boldsymbol{r}_{\rm SO}(t)]\widetilde{\omega}^b/A$. We explain the terms in the above equations as follows:

1. $\mu_\alpha^b(t-t_0)$ and $\mu_\delta^b(t-t_0)$ are linear displacements from the TSB due to proper motions and so are first-order terms.
2. $\boldsymbol{p}_b\cdot\boldsymbol{R}$ and $\boldsymbol{q}_b\cdot\boldsymbol{R}$ are the parallax of a star if there is no companion around the star. If a star hosts companions, these terms reflect the combined effect of the motion of the observer and the reflex stellar motion on the displacement of the star with respect to the TSB. This is a first-order term.
3. $\mu_\alpha^b\mu_r^b(t-t_0)^2$ and $\mu_\delta^b\mu_r^b(t-t_0)^2$ are second-order terms related to the so-called "perspective acceleration." Because this effect is proportional to the square of time, it becomes significant for long-baseline astrometry. For example, μ_α will change by about 6 mas yr^{-1} due to the perspective acceleration over 10 years of observations of α Centauri.
4. $[\mu_\alpha^b\boldsymbol{u}_b\cdot\boldsymbol{R} + \mu_r^b\boldsymbol{p}_b\cdot\boldsymbol{R}](t-t_0)$ and $[\mu_\delta^b\boldsymbol{u}_b\cdot\boldsymbol{R} + \mu_r^b\boldsymbol{q}_b\cdot\boldsymbol{R}](t-t_0)$ are second-order terms and are linearly proportional to time. These terms are related to the coupling of the proper motion or radial velocity with the motion of the Earth and stellar reflex motion. Because they are linear functions of time, they only become important for the interpretation of observations taken over decades. For example, this term will contribute to 0.1 mas offset over a decade of observation of α Centauri.
5. $(\boldsymbol{p}_b\cdot\boldsymbol{R})(\boldsymbol{u}_b\cdot\boldsymbol{R})$ and $(\boldsymbol{q}_b\cdot\boldsymbol{R})(\boldsymbol{u}_b\cdot\boldsymbol{R})$ are terms related to the coupling of Earth's motion and stellar reflex motion in different directions. This term does not significantly increase with time because the orbits of the observer and the stellar reflex motion are periodic and the corresponding semimajor axis does not change much over time. Thus this term only contributes to a microarcsecond displacement even for nearby stars such as α Centauri.

Although Equation (9) only expands the offset to the second order, there are two third-order terms that become important for decades-long astrometry observations:

1. $\xi(t)^3/6 = \xi(t) - \sin\xi(t)$ and $\eta(t)^3/6 = \eta(t) - \sin\eta(t)$ are the third-order terms for a Taylor expansion of a sinusoidal function in the vicinity of zero. This term can introduce a submilliarcsecond offset for high proper motion stars. For example, this term is about 0.3 mas for α Centauri for a 100 yr observational baseline. It would be about 8.8 mas for a century of observations of Barnard's star.
2. $\mu_\alpha\mu_r^2(t-t_0)^3$ and $\mu_\delta\mu_r^2(t-t_0)^3$ are related to the coupling of proper motion and radial motion of the TSB. The sums of these two terms are respectively about 1 and 40 mas for 100 yr observations of α Centauri and Barnard's star.

Models that only account for the first-order terms are not reliable for the detection or characterization of planets that induce submilliarcsecond reflex motion. For example, the maximum reflex offset of a Sun-like star at 10 pc is 0.50 mas for a Jupiter-like planet, 0.27 mas for a Saturn-like planet, 0.08 mas for Uranus, and 0.16 mas for Neptune. Without including these higher order terms, it would be impossible to robustly detect them even if data from all the individual *Gaia* epochs were available.

Reference stars are typically difficult to obtain due to the large relative brightness of stars, such as α Centauri A and B. Thus, relative astrometry is more reliable than absolute astrometry in terms of constraining the orbit of α Centauri (Kervella et al. 2016; Pourbaix & Boffin 2016). By removing the third-order terms from Equation (9), we derive the relative offset of the secondary with respect to the primary:

$$\begin{aligned}\Delta\xi(t) &= \boldsymbol{p}_b\cdot\Delta\boldsymbol{R}(t) - [\mu_\alpha^b\boldsymbol{u}_b\cdot\Delta\boldsymbol{R}(t) \\ &\quad + \mu_r^b\boldsymbol{p}_b\cdot\Delta\boldsymbol{R}(t)](t-t_0), \\ \Delta\eta(t) &= \boldsymbol{q}_b\cdot\Delta\boldsymbol{R}(t) - [\mu_\alpha^b\boldsymbol{u}_b\cdot\Delta\boldsymbol{R}(t) \\ &\quad + \mu_r^b\boldsymbol{q}_b\cdot\Delta\boldsymbol{R}(t)](t-t_0),\end{aligned} \tag{10}$$

where $\Delta\boldsymbol{R}(t) \equiv \boldsymbol{R}_2(t) - \boldsymbol{R}_1(t) = \Delta\boldsymbol{r}(t)\widetilde{\omega}^b/A$, and $\Delta\boldsymbol{r} \equiv \boldsymbol{r}_{\rm BT2}(t) - \boldsymbol{r}_{\rm BT1}(t)$ denotes the Keplerian motion of the secondary with respect to the primary. It is notable that the relative astrometry depends not only on the reflex motion but also on the astrometry and radial velocity of the TSB when considering secondary effects. This linear-time secondary effect could contribute to submilliarcsecond offsets that are comparable with the signal caused by Jupiter-like planets around nearby stars.

2.2. Radial Velocity Model

The time derivative of $\boldsymbol{r}_{\rm OT}$ (Equation (1)) determines the observed velocity of a star:

$$\boldsymbol{v}_{\rm OT} = \boldsymbol{v}_{\rm OS} + \boldsymbol{v}_{\rm SB} + \boldsymbol{v}_{\rm BT}. \tag{11}$$

The observed radial velocity is the projection of $\boldsymbol{v}_{\rm OT}$ onto the observed direction of the star:

$$v_r(t) = \boldsymbol{v}_{\rm OT}(t)\cdot\boldsymbol{u}_{\rm OT}(t) \tag{12}$$

The terms $\boldsymbol{v}_{\rm OT}(t)$ and $\boldsymbol{u}_{\rm OT}$ can be respectively calculated from Equations (5) and (11) given the astrometry and radial velocity of a star and its reflex motion as well as the Jet Propulsion Laboratory (JPL) ephemeris such as DE430 (Folkner et al. 2014) and the rotation of the Earth. Thus, the above vectorized formula is the most robust nonrelativistic modeling of radial velocity. However, to compare with other radial velocity models, we need to approximate this model through Taylor

expansions. We expand $\boldsymbol{u}_{\rm OT}(t)$ to the first-order Taylor series

$$\boldsymbol{u}_{\rm OT}(t) = \boldsymbol{u}_b + \Delta\boldsymbol{u}_t(t) + \mathcal{O}(|\Delta\boldsymbol{u}_t(t)|^2), \quad (13)$$

where

$$\Delta\boldsymbol{u}_t(t) = (\boldsymbol{p}_b\mu_\alpha^b + \boldsymbol{q}_b\mu_\delta^b)(t - t_0) + \boldsymbol{R}_t(t) \quad (14)$$

is the tangential component of the change of $\boldsymbol{u}_{\rm OT}$, and $\boldsymbol{R}_t(t)$ is the tangential component of $\boldsymbol{R}(t)$. Then the radial velocity becomes

$$v_r(t) = \boldsymbol{v}_{\rm OT}(t)\cdot\boldsymbol{u}_b + \boldsymbol{v}_{\rm OT}(t)\cdot\Delta\boldsymbol{u}_t(t). \quad (15)$$

In the above equation, the first term is the classical radial velocity model, which does not account for the influence of the perspective variation on the radial velocity. This perspective change is approximated by the second term, which is related to the tangential reflex motion and the tangential motion of the observer perpendicular to $\boldsymbol{u}_b$. Because the radial velocities are typically measured with respect to a reference epoch t_0, we derive the variation of radial velocity, which is

$$\Delta v_r(t) = \boldsymbol{v}_{\rm OT}(t)\boldsymbol{u}_{\rm OT}(t) - \boldsymbol{v}_{\rm OT}(t_0)\boldsymbol{u}_{\rm OT}(t_0). \quad (16)$$

The above geometric model of radial velocity does not account for relativistic effects, which will be discussed in Section 3.4.

2.3. Stellar Reflex Motion

We calculate the stellar reflex motion in the coordinate system formed by the triad $[\boldsymbol{p}_b\ \boldsymbol{q}_b\ \boldsymbol{u}_b]$. Because this coordinate system is determined at the reference epoch, the orbital parameters are also calculated with respect to the reference epoch. This is different from the rotation reference frame , where the orbital elements may vary with time due to the adoption of a noninertial frame (Kopeikin 1996).

In the orbital-plane coordinate system shown in Figure 2, the position of the target star is denoted by $\boldsymbol{r}_{\rm orb} = (x, y, 0)^{\rm T}$. The orbital-plane coordinate system is transformed into the sky-plane coordinate system through a sequence of rotations such that the position of the target star with respect to the TSB is

$$\begin{bmatrix} x_{\rm BT} \\ y_{\rm BT} \\ z_{\rm BT} \end{bmatrix} = \begin{bmatrix} B' & G' & \cos\Omega\sin I \\ A' & F' & -\sin\Omega\sin I \\ C' & H' & -\cos I \end{bmatrix} \begin{bmatrix} x \\ y \\ 0 \end{bmatrix}, \quad (17)$$

where

$$\begin{aligned} A' &= \cos\Omega\cos\omega_{\rm T} - \sin\Omega\sin\omega_{\rm T}\cos I \\ B' &= \sin\Omega\cos\omega_{\rm T} + \cos\Omega\sin\omega_{\rm T}\cos I \\ F' &= -\cos\Omega\sin\omega_{\rm T} - \sin\Omega\cos\omega_{\rm T}\cos I \\ G' &= -\sin\Omega\sin\omega_{\rm T} + \cos\Omega\cos\omega_{\rm T}\cos I \\ C' &= \sin\omega_{\rm T}\sin I \\ H' &= \cos\omega_{\rm T}\sin I \end{aligned}$$

are the elements of the rotation matrix and a scaled version of the so-called "Thiele–Innes constants." In the above equations, Ω is the longitude of the ascending node, $\omega_{\rm T}$ is the argument of periastron for the orbit of the target star around the TSB, and I is the inclination. The argument of periastron for the barycentric motion of the companion is $\omega_C = \omega_{\rm T} + \pi$. Because this convention of binary motion is consistent with the triad used for the astrometry model, we call it the "astrometric convention," which is described in detail in Appendix A.4.

The Keplerian motion of the target star with respect to the TSB is

$$\begin{aligned} \boldsymbol{r}_{\rm BT}(t) &= [B'x(t) + G'y(t)]\boldsymbol{p}_b + [A'x(t) \\ &\quad + F'y(t)]\boldsymbol{q}_b + [C'x(t) + H'y(t)]\boldsymbol{u}_b, \\ \boldsymbol{v}_{\rm BT}(t) &= [B'\dot{x}(t) + G'\dot{y}(t)]\boldsymbol{p}_b + [A'\dot{x}(t) \\ &\quad + F'\dot{y}(t)]\boldsymbol{q}_b + [C'\dot{x}(t) + H'\dot{y}(t)]\boldsymbol{u}_b, \end{aligned} \quad (18)$$

and the Keplerian motion in the orbital plane (see Figure 2) is

$$\begin{aligned} x(t) &= a_{\rm T}[\cos E(t) - e] \\ y(t) &= a_{\rm T}[\sqrt{1-e^2}\sin E(t)] \\ \dot{x}(t) &= -a_{\rm T}\frac{n\sin E(t)}{1 - e\cos E(t)} \\ \dot{y}(t) &= a_{\rm T}\sqrt{1-e^2}\frac{n\cos E(t)}{1 - e\cos E(t)}, \end{aligned} \quad (19)$$

where $a_{\rm T} = \frac{m_C}{m_C + m_T}a$ is the semimajor axis of the target star with respect to the TSB; a is the semimajor axis of the target star with respect to its companion; $E(t)$ is the eccentric anomaly, which is determined by solving Kepler's equation $M(t) = E(t) - e\sin E(t)$ for a given time, t; e is the eccentricity; $n \equiv 2\pi/P$ is the mean orbital motion; and P is the orbital period. By transforming the Keplerian motion from the orbital-plane reference frame into the sky-plane reference frame using Equation (18), we derive $\boldsymbol{r}_{\rm BT}$ and $\boldsymbol{v}_{\rm BT}$ to model astrometry and radial velocity fully using Equations (5) and (12).

3. Relativistic and High-order Geometric Effects

Relativistic effects can be important for nearby or binary systems such as α Centauri. For example, assuming an orbital period of 80 yr, a semimajor axis of 17.6 au, and an inclination of 79° for α Centauri A and B, the arrival time of light from A or B is changed by 6.3 hr due to binary motion over 40 yr. Although this is small compared with the binary orbital period, it would introduce timing noise and thus bias the detection of potential exoplanets in this system.

For the convenience of calculation of relativistic terms, we define various times following E06. The proper emission time τ_e of a photon is derived from the proper observed arrival time τ_o by including various delays as follows:

$$\tau_e = \tau_o - \Delta_{\rm S} - \Delta_{\rm is} - \Delta_{\rm T}, \quad (20)$$

where $\Delta_{\rm S}$ is the time delay due to effects in the solar system, $\Delta_{\rm is}$ is related to the travel time of a photon in the interstellar medium, and $\Delta_{\rm T}$ is the delay related to the target system. We introduce the coordinate time of light arrival at the SSB, $t_a^{\rm SSB} = \tau_o - \Delta_{\rm S}$, and the coordinate time of light arrival at the TSB, $t_a^{\rm TSB} = t_a^{\rm SSB} - \Delta_{\rm is}$. The proper emission time and the arrival time at TSB are related by $\tau_e = t_a^{\rm TSB} - \Delta_{\rm T}$. We also define the coordinate reference time $t_{\rm pos}$ as the epoch when the position or astrometry of the target star is measured. At the reference epoch, $t_a^{\rm SSB} = t_a^{\rm TSB} = t_{\rm pos}$. We will introduce

post-Newtonian and GR models of binary motion in Section 3.1 and describe various relativistic terms in the models of timing (Section 3.2), astrometry (Section 3.3), and radial velocity (Section 3.4).

3.1. Post-Newtonian Stellar Reflex Motion

In Section 2.3, we derive the formula for the classical Keplerian motion in the reference frame formed by the triad $[\boldsymbol{p}_b\ \boldsymbol{q}_b\ \boldsymbol{u}_b]$. Here we model the post-Newtonian Keplerian (PPK) motion in terms of proper emission time τ_e according to previous works (Damour & Deruelle 1986; Taylor & Weisberg 1989, and E06):

$$\boldsymbol{r}_{\rm BT} = [\boldsymbol{p}_b\ \boldsymbol{q}_b\ \boldsymbol{u}_b]\begin{bmatrix}\sin\Omega & -\cos\Omega & 0\\ \cos\Omega & \sin\Omega & 0\\ 0 & 0 & 1\end{bmatrix}\begin{bmatrix}1 & 0 & 0\\ 0 & -\cos I & -\sin I\\ 0 & \sin I & -\cos I\end{bmatrix} \times \begin{bmatrix} r_{\rm reflex}\cos\theta \\ r_{\rm reflex}\sin\theta \\ 0\end{bmatrix}, \tag{21}$$

where

$$\begin{aligned} r_{\rm reflex} &= a_r(1 - e_r\cos U),\\ M &= n(\tau_e - \tau_p) = U - e_\theta\sin U,\\ \theta &= \omega + A_{e_\theta}(U),\\ A_{e_\theta}(U) &= 2\tan^{-1}\left[\left(\frac{1+e_\theta}{1-e_\theta}\right)^2\tan\frac{U}{2}\right],\\ e_r &= e(1+\delta_r),\\ e_\theta &= e(1+\delta_\theta),\\ n &= \frac{2\pi}{P_0} + \frac{\pi\dot{P}(\tau_e-\tau_p)}{P_0^2},\\ \omega &= \omega_0 + kA_e(U),\\ k &= \frac{\dot{\omega}}{n},\\ e &= e_0 + \dot{e}(\tau_e-\tau_p),\\ x_a &= x_{a0} + \dot{x}_a(\tau_e-\tau_p), \end{aligned} \tag{22}$$

where ω_0, e_0, P_0 are the Keplerian parameters at the reference epoch, τ_p is the proper time of periastron, U is the relativistic eccentric anomaly, a_r is the semimajor axis of the primary with respect to the barycenter of the target system, δ_r and δ_θ are PPK terms used to define eccentricities, and $x_a \equiv a\sin I/c$ is the light travel time across the projected semimajor axis. Because this model was first proposed by Damour & Deruelle (1986), we call it "DD," following Taylor & Weisberg (1989) and E06. Because the x axis of the orbital plane is in the direction of the ascending node rather than periastron as in the astrometric convention, we call this coordinate system framework the "precession-compatible convention," which is described in detail in Appendix A.4.

Considering GR, we define $m_{\rm tot} = m_C + m_{\rm T}$ and give the following relativistic terms after E06's Equations (71) and (80)–(88):

$$\begin{aligned} \dot{\omega}^{\rm GR} &= 3T_\odot^{2/3}n^{5/3}\frac{m_{\rm tot}^{2/3}}{1-e^2},\\ g^{\rm GR} &= T_\odot^{2/3}n^{-1/3}e\frac{m_C(m_T+2m_C)}{m_{\rm tot}^{4/3}},\\ r_s^{\rm GR} &= T_\odot m_C,\\ s_s^{\rm GR} &= \sin I = T_\odot^{-1/3}n^{2/3}x_a\frac{m_{\rm tot}^{2/3}}{m_C},\\ \delta_r^{\rm GR} &= T_\odot^{2/3}n^{2/3}\frac{3m_T^2 + 6m_Tm_C + 2m_C^2}{m_{\rm tot}^{4/3}},\\ \delta_\theta^{\rm GR} &= T_\odot^{2/3}n^{2/3}\frac{\frac{7}{2}m_T^2 + 6m_Tm_C + 2m_C^2}{m_{\rm tot}^{4/3}},\\ \dot{P}^{\rm GR} &= -\frac{192\pi}{5}T_\odot^{5/3}n^{5/3}\frac{m_Tm_C}{m_{\rm tot}^{1/3}}\frac{1 + 73e^2/24 + 37e^4/96}{(1-e^2)^{7/2}}, \end{aligned} \tag{23}$$

where GR denotes general relativity, c is the speed of light, $T_\odot = Gm_\odot/c^3$ is half the light travel time across the solar Schwarzschild radius, $m_\odot$ is the solar mass, G is the gravitational constant, g is the timing model parameter, and $r_s^{\rm GR}$ and $s_s^{\rm GR}$ are parameters for the Shapiro delay in the target system assuming GR. We call this model "DDGR" following the syntax of TEMPO2.

In a combined model of radial velocity and astrometry, the free classical orbital parameters are $\{P_0, e_0, \omega_0, I, \Omega, \tau_p\}$ as well as masses $\{m_C, m_{\rm T}\}$. For general post-Newtonian theories, the additional fittable parameters are $\{\dot{\omega}, g, \dot{P}, s_s, r_s, \dot{x}_a, \dot{e}\}$, where s_s and r_s are respectively the shape and range parameters of Shapiro delay. For a classical Keplerian orbit, $\dot{\omega}$, $\dot{P}$, $\dot{x}_a$, $\dot{e}$ are all zero.

3.2. Timing Model

We transform the proper light arrival time at the observatory τ_o to the barycentric coordinate time ($t_a^{\rm SSB}$) by calculating the "tropospheric delay" ($\Delta_{\rm tropo}$), "Roemer delay" ($\Delta_{\rm rS}$), "Shapiro delay" ($\Delta_{\rm sS}$), and "Einstein delay" ($\Delta_{\rm eS}$). Then we transform $t_a^{\rm SSB}$ to the light arrival coordinate time at the TSB ($t_a^{\rm TSB}$) by calculating the vacuum propagation time of the light traveling from SSB to TSB ($\Delta_{\rm vp}$) as well as the Einstein delay ($\Delta_{\rm ei}$) due to the relative motion between TSB and SSB. Finally, we derive the proper emission time τ_e from $t_a^{\rm TSB}$ by calculating the Roemer delay ($\Delta_{\rm rT}$), Shapiro delay ($\Delta_{\rm sT}$), and Einstein delay ($\Delta_{\rm eT}$) in the target system.

The purpose of modeling the light emission time is to calculate the mean anomaly of the stellar reflex orbit precisely given an observation proper time τ_o. The formulae in the following sections are similar to the formulae given in E06 for pulsar timing but are adapted and implemented to be more suitable for exoplanets.

3.2.1. Tropospheric Delay

The time delay in the solar system is

$$\Delta_{\rm S} \simeq \Delta_{\rm tropo} + \Delta_{\rm eS} + \Delta_{\rm rS} + \Delta_{\rm pS} + \Delta_{\rm sS}, \tag{24}$$

where $\Delta_{\rm pS}$ is a second-order Roemer delay, called "parallax delay" (E06).

An incident light ray is refracted by Earth's atmosphere and is delayed by (Nilsson et al. 2013)

$$\Delta_{\rm tropo} = c\int_{\mathcal{L}} [n(l) - 1]dl + (t_{\mathcal{L}} - t_{\mathcal{G}}), \quad (25)$$

where $\mathcal{L}$ is the light ray path in the atmosphere, n is the refractive index, and $t_{\mathcal{L}}$ and $t_{\mathcal{G}}$ are respectively the vacuum light propagation times for deflected and straight light rays. Because the atmosphere model typically consists of the hydrostatic and wet components, the tropospheric delay is typically split into two parts:

$$\Delta_{\rm tropo} = \frac{10^{-6}}{c}\int_{\mathcal{L}} N_{\rm hydro}(l)dl + \frac{10^{-6}}{c} \times \int_{\mathcal{L}} N_{\rm wet}(l)dl + (t_{\mathcal{L}} - t_{\mathcal{G}}) \quad (26)$$

$$= \Delta_{\rm hydro} + \Delta_{\rm wet} + (t_{\mathcal{L}} - t_{\mathcal{G}}), \quad (27)$$

where $N_{\rm hydro}$ and $N_{\rm wet}$ are respectively the hydrostatic and wet refractivity. The refractivity is related to the refractive index by $N = 10^{-6}(n - 1)$. Each of these two components is a product of a zenith delay and a mapping function. The geometric delay term $t_{\mathcal{L}} - t_{\mathcal{G}}$ is typically included in the mapping function of the hydrostatic component (Nilsson et al. 2013). Hence, the tropospheric delay becomes

$$\Delta_{\rm tropo} = \Delta_{\rm hydro} m_h(\Theta) + \Delta_{\rm wz} m_w(\Theta), \quad (28)$$

where Θ is the observed elevation angle of the source, and $\Delta_{\rm hydro}$ is[6]

$$\Delta_{\rm hydro} = \frac{0.02268\left(\frac{p_{\rm O}}{\rm kPa}\right)}{\left(\frac{c}{\rm m\ s^{-1}}\right)[1 - 0.00266\cos(2\phi_{\rm O}) - 2.8\times 10^{-7}\left(\frac{h_{\rm O}}{\rm m}\right)]}, \quad (29)$$

where $\phi_{\rm O}$ is the latitude of the observatory, $p_{\rm O}$ is the air pressure, and $h_{\rm O}$ is the telescope altitude. The zenith hydrostatic delay is typically a few nanoseconds. On the other hand, the wet zenith delay is not well modeled and is highly variable. However, it is about one order of magnitude smaller than the hydrostatic delay and thus is only important for high-precision applications. Following E06, we adopt the Niell mapping function (Niell 1996) to calculate m_h and m_w in Equation (28). Like E06, we only consider the wet component if the zenith wet delay is given by the observatory. Similar to the wet component, the refraction caused by the ionosphere is highly variable and cannot be separated from the dispersion in the interstellar and interplanetary medium. Thus, we consider them as time-correlated noise, which can be modeled using a red noise model such as the moving-average model (Feng et al. 2017).

3.2.2. Time Delay in the Solar System

The Einstein delay is caused by the gravitational effect on the time measurement in different reference systems. According to E06 and Irwin & Fukushima (1999), the Einstein delay is

$$\Delta_{\rm eS} = \frac{1}{c^2}\int_{t_0}^{t}\left(U_\oplus + \frac{v_\oplus^2}{2} + \Delta L_C^{\rm (PN)} + \Delta L_C^{\rm (A)}\right)dt + \frac{\boldsymbol{s}\cdot\dot{\boldsymbol{r}}_\oplus + W_0\tau_o}{c^2}, \quad (30)$$

where $U_\oplus$ is the gravitational potential of all solar system objects apart from the Earth, $v_\oplus$ is the barycentric velocity of the geocenter, W_0 is approximately the gravitational and spin potential of the Earth at the geoid, and $\Delta L_C^{\rm (PN)}$ and $\Delta L_C^{\rm (A)}$ respectively characterize the post-Newtonian effects and asteroidal effects. The integral is to transform the Geocentric Coordinate Time (TCG) into the barycentric time (TCB) at the geocenter. In the above equation, the last term corresponds to the time difference between the observer and the geocenter and transforms the terrestrial time (TT) to TCG. The rate of TT with respect to TCG at the geocenter is $L_G = W_0/c^2 = 6.969290134\times 10^{-10}$. The term $\Delta_{\rm rot} = \boldsymbol{s}\cdot\dot{\boldsymbol{r}}_\oplus/c^2$ induces a periodic delay with an amplitude of about 2 μs. We model the Earth's rotation using Equation (26) in E06.

Instead of calculating the integral in Equation (30) directly, we use the time ephemeris of the Earth in JPL DE430 to transform TT at the geocenter to Barycentric Dynamical Time (TDB) and use $L_B = 1.550519768\times 10^{-8}$ to transform TDB into TCB according to TCB = TDB/$(1 - L_B)$. Because the rotation-induced delay $\boldsymbol{s}\cdot\dot{\boldsymbol{r}}_\oplus/c^2$ is not accounted for in the transformation from TT to TDB by the JPL ephemeris, we add it in the transformation and determine TDB in an iterative way as follows:

1. Transform Coordinate Universal Time (UTC) to the International Atomic Time (TAI; *Temps Atomique* in French) using the SOFA[7] routine iauUtctai.
2. Transform TAI to TT(BIPMXY). BIPM denotes the International Bureau of Weights and Measures, and XY represents the year when the BIPM realization of TT is published. TT(BIPMXY) = TAI+32.184 s+δt, where δT is the difference between the BIPMXY and TAI realizations of TT (Petit 2004) and can be downloaded from https://www.bipm.org/jsp/en/TimeFtp.jsp?TypePub=ttbipm. In this work, we use the TT(BIPM17) realization by default. The BIPM file is automatically updated to the latest version by PEXO.
3. Determine TT-TDB as a function of TT at the geocenter using the latest JPL time ephemeris (e.g., DE430t).
4. For a ground-based observer, determine the observer's geocentric position and velocity using the Earth rotation model recommended by IAU2006 resolutions (Capitaine & Wallace 2006; Wallace & Capitaine 2006). For space telescopes, their ephemerides are determined using the JPL HORIZONS system. We have implemented an automated downloading of JPL ephemerides in PEXO.
5. Calculate $\Delta_{\rm rot}$ in the TDB coordinate system based on step 4 and add it onto TT-TDB. Note that $\Delta_{\rm rot}$ is calculated using TT and thus needs to be scaled with dTT/dTDB, although this scaling is a negligible secondary effect and only contributes at most 1 ps (1 ps = picosecond = 1×10^{-12} s).

[6] Note that the routine tropo.C in the TEMPO2 package contains an error. The cosine function in the denominator should be $\cos(2\phi_{\rm O})$ rather than $\cos\phi_{\rm O}$. However, this error may not significantly influence the TEMPO2 precision because $\cos(2\phi_{\rm O})$ is multiplied by 0.00266.

[7] http://www.iausofa.org/

6. Transform TDB to TCB using $\mathrm{TCB} = \mathrm{TDB}/(1 - L_B)$.

In summary, the transformation chain of various time standards is UTC → TAI → TT → TCG → TDB → TCB.

To derive the barycentric time, we need to account for the difference in the light travel time to the observer and to the SSB. This is the so-called Roemer delay, which is

$$\Delta_{\mathrm{rS}} = \frac{\boldsymbol{r}_{\mathrm{SO}} \cdot \boldsymbol{u}_{\mathrm{SB}}}{c}, \tag{31}$$

where $\boldsymbol{r}_{\mathrm{SO}} = \boldsymbol{r}_{\oplus} + \boldsymbol{s}$ is the sum of the BCRS position of the geocenter $\boldsymbol{r}_{\oplus}$ and the position of the observatory with respect to the geocenter $\boldsymbol{s}$. For space telescopes, $\boldsymbol{r}_{\mathrm{SO}}$ can be obtained from the ephemeris of the telescope from JPL HORIZONS. However, the Roemer delay assumes that the fiducial observer at the SSB receives plane waves from the light source. To account for the curvature of the wave, we include the second-order "Roemer delay":

$$\Delta_{pS} = \frac{|\boldsymbol{r}_{\mathrm{SO}} \times \boldsymbol{u}_{\mathrm{SB}}|^2}{2cr_{\mathrm{SB}}}. \tag{32}$$

This so-called "parallax delay" is included in the Roemer delay in some other studies (e.g., Lindegren & Dravins 2003 and Eastman et al. 2010). For example, the parallax delay for α Centauri is about 0.7 ms. Note that this parallax delay is equal to the one in Equation (8) of Eastman et al. (2010; hereafter E10), who use $\boldsymbol{u}_{\mathrm{OT}}$ rather than $\boldsymbol{u}_{\mathrm{SB}}$ as the reference unit vector, leading to an opposite sign of parallax delay. However, Equations (31) and (32) do not account for higher-order astrometric effects, as mentioned in Section 2.1. To improve the precision of PEXO for solar system objects, we calculate the total Roemer delay (including parallax delay) using

$$\Delta_{\mathrm{rS}} = \frac{r_{\mathrm{OT}} - r_{\mathrm{ST}}}{c}. \tag{33}$$

Because the third-order astrometric terms contribute submilliarcsecond position offsets over decades, we expect tens of nanoseconds bias to be introduced by using Equations (31) and (32). Such a bias is inversely proportional to the heliocentric distance and increases with time, as we will see in Section 4.1. Because this bias is cumulative, the estimation of <1 ns for third-order delays in E10 is not representative for long-term timing observations.

A photon is deflected by the gravitational field of the solar system, leading to the so-called "Shapiro delay" (Shapiro 1964), which is

$$\Delta_{\mathrm{sS}} = (1 + \gamma)\sum_i \frac{Gm_i}{c^3}\left\{\ln\left(\frac{2r_{\mathrm{ST}}}{A}\right) - \ln\left[\frac{r_{\mathrm{SO}}(1 - \cos\psi_i)}{A}\right]\right\}, \tag{34}$$

where $A = 1$ au, and ψ_i is the coordinate angle distance between the center of the body i and the target star from the perspective of the observer. The angle between the Sun and the target star dominates the Shapiro delay and is determined by $\cos\psi_i = \frac{\boldsymbol{r}_{\mathrm{OT}}\boldsymbol{r}_{\mathrm{OS}}}{r_{\mathrm{OT}}r_{\mathrm{OS}}}$. The Shapiro delay formulated in Equation (34) differs from Equation (5) of Eastman et al. (2010), who ignore the terms related to r_{ST} and r_{SO}. However, r_{SO} is not constant for an observer on an eccentric orbit. Although this change may not be important for current exoplanet research, it is crucial for high-precision pulsar timing and thus is included in the model of TEMPO2 by E06.

In summary, the barycentric Julian date (BJD) in the TCB standard ($\mathrm{BJD_{TCB}}$) is determined by the corresponding Julian date ($\mathrm{JD_{TCB}}$) through $\mathrm{BJD_{TCB}} = \mathrm{JD_{TCB}} - \Delta_{\mathrm{rS}} - \Delta_{\mathrm{pS}} - \Delta_{\mathrm{sS}}$, where $\mathrm{BJD_{TCB}}$ and $\mathrm{JD_{TCB}}$ are BJD and JD in the TCB time standards, respectively. BJD can only be determined precisely if the precise location of the observed target is known at a given epoch. However, this is impossible even with *Gaia* astrometry because the astrometric solution is based on the assumption of a single star. Thus, BJD is known a posteriori rather than a priori by simultaneously modeling the motions of the Earth, the barycenter of the target system, and the stellar reflex motion. We will discuss the influence of decoupling the solar and target systems on timing in Section 3.5. Although PEXO does not separate the solar system dynamics and the target system dynamics in its timing model, we provide $\mathrm{BJD_{TDB}}$ and $\mathrm{BJD_{TCB}}$ for users who do not require a timing precision of <0.02 s. The upper limit of this precision corresponds to the timing bias amplitude for α Centauri A due to the decoupling of α Centauri and the solar system over one decade (see Section 5.4). For users who need a high-precision timing model, PEXO provides a combined modeling of all motions and various times as optional outputs.

PEXO generates quantities compatible with both TDB and TCB time standards. TCB is used as the time standard for *Gaia* (*Gaia* Collaboration et al. 2018), while TDB is used by *TESS* (Ricker et al. 2014). Because TDB is a time standard compatible with JPL ephemeris and has a time-increasing rate very similar to that of TT and TAI, it is frequently used in the exoplanet community. TCB by definition is not a relativistic time standard and is not sensitive to relativistic effects in the solar system, although its realization may depend on the relativistic simulation of the solar system. Both TDB and TCB systems have particular advantages; we provide the ability to introduce data from both time standards, for example, for the combined analysis of the data from *Gaia* and *TESS*. The critical matter is a consistent transformation when using data sets with different time standards. PEXO is designed to provide for this. We refer the readers to Klioner et al. (2010) and Petit & Luzum (2010) for a detailed discussion of different time standards.

3.2.3. Interstellar Time Delay

Ignoring the interaction between a photon with the interstellar medium, the arrival time at the SSB is delayed with respect to the TSB by

$$\Delta_{\mathrm{is}} \simeq \Delta_{\mathrm{vp}} + \Delta_{\mathrm{ei}}, \tag{35}$$

where $\Delta_{\mathrm{vp}} = |\boldsymbol{v}_{\mathrm{SB}}(t_a^{\mathrm{SSB}} - t_{\mathrm{pos}}) + \boldsymbol{r}_{\mathrm{SB}}(t_{\mathrm{pos}})|/c$. Because the vacuum propagation of light at the reference time ($|\boldsymbol{r}_{\mathrm{SB}}(t_{\mathrm{pos}})|/c$) is a constant, we only model the relative vacuum propagation delay, $\Delta_{\mathrm{vp}} = |\boldsymbol{v}_{\mathrm{SB}}(t_a^{\mathrm{SSB}} - t_{\mathrm{pos}}) + \boldsymbol{r}_{\mathrm{SB}}(t_{\mathrm{pos}})|/c - |\boldsymbol{r}_{\mathrm{SB}}(t_{\mathrm{pos}})|/c$. The Einstein delay due to the relative motion between TSB and SSB is

$$\Delta_{\mathrm{ei}} = \frac{v_{\mathrm{SB}}^2}{2c^2}(t_a^{\mathrm{SSB}} - t_{\mathrm{pos}} - \Delta_{\mathrm{vp}}). \tag{36}$$

3.2.4. Time Delay in the Target System

Similar to the time delay in the solar system, the delay in the target system is

$$\Delta_{\rm T} \simeq \Delta_{\rm rT} + \Delta_{\rm pT} + \Delta_{\rm eT} + \Delta_{\rm sT}. \quad (37)$$

According to E06, the Roemer delay is

$$\Delta_{\rm rT} = \frac{\boldsymbol{r}_{\rm BT}\cdot\boldsymbol{u}_b}{c} + \frac{1}{cr_{\rm SB}} \times \left(\boldsymbol{\mu}\cdot\boldsymbol{r}_{\rm BT,\perp} - \boldsymbol{r}_{\rm SO,\perp}\cdot\boldsymbol{r}_{\rm BT,\perp} + \frac{|\boldsymbol{r}_{\rm BT,\perp}|^2}{2}\right), \quad (38)$$

where $\boldsymbol{r}_{\rm SO,\perp} = \boldsymbol{u}_b \times (\boldsymbol{r}_{\rm SO}\times\boldsymbol{u}_b)$ and $\boldsymbol{r}_{\rm BT,\perp} = \boldsymbol{u}_b \times (\boldsymbol{r}_{\rm BT}\times\boldsymbol{u}_b)$. In the above equation, the first term is related to the Roemer delay that is due to the motion of TSB, while the other terms are named "Kopeikin terms" related to the orbital variation of the target system that is due to the changing perspective caused by the proper motion of TSB (Kopeikin 1996). In a rotation reference frame perpendicular to the line of sight, these terms can "change" the orbital elements of the target system. However, such an apparent change disappears if the orbit is defined at the reference epoch in a fixed reference frame, as in Equation (3).

Instead of using the reference unit vector $\boldsymbol{u}_b$, we use the time-varying vector $\boldsymbol{u}_{\rm SB}$ to calculate the combined Roemer and parallax delay as

$$\Delta_{\rm rT} + \Delta_{\rm pT} = \frac{\boldsymbol{r}_{\rm BT}\cdot\boldsymbol{u}_{\rm SB}}{c} - \frac{|\boldsymbol{r}_{\rm BT}\times\boldsymbol{u}_{\rm SB}|^2}{2cr_{\rm SB}}. \quad (39)$$

This delay is similar to its counterpart in the solar system, as expressed in Equations (31) and (32).

According to Blandford & Teukolsky (1976) and Damour & Deruelle (1986), the Einstein delay in the target system is

$$\Delta_{\rm eT} = gU, \quad (40)$$

where g is the timing model parameter.

According to Damour & Deruelle (1986), the Shapiro delay for the target system is

$$\Delta_{\rm sT} = -2r_s \log\{1 - e\cos U - s_s[\sin\omega(\cos U - e) + (1-e^2)^{1/2}\cos\omega\sin U]\}, \quad (41)$$

where all of the variables are given in Section 3.1. Although higher-order Shapiro delay terms are available (Kopeikin & Schäfer 1999), they are insignificant because the first-order term is of the order of $(v_{\rm BT}/c)^3$.

3.3. Astrometry Model

The direction of a light ray observed by an observer is deflected by the gravitational field between the source and the frame transformation between the observer and the target. Thus we aim to find the observed direction of the target star by tracing the direction of a photon forward from the emission time to the arrival time at the observatory. To avoid confusion with the geometric modeling of the observed direction of the source derived in Section 2.1, we use $\boldsymbol{l}$ to denote the direction of a light ray at a given time.

3.3.1. Stellar Aberration

According to special relativity, the Lorentz transformation from a static reference frame to a moving reference frame would introduce a change in the direction of the target star. This effect is called "stellar aberration." After Equation (7) of Klioner (2003), the direction of the observed light ray is

$$\begin{aligned}\hat{\boldsymbol{u}}_o &= \langle -\boldsymbol{l}_o + c^{-1}\boldsymbol{l}_o\times(\boldsymbol{v}_{\rm SO}\times\boldsymbol{l}_o) + c^{-2}\Big[(\boldsymbol{l}_o\cdot\boldsymbol{v}_{\rm SO})\boldsymbol{l}_o \times(\boldsymbol{v}_{\rm SO}\times\boldsymbol{l}_o) + \frac{1}{2}\boldsymbol{v}_{\rm SO}\times(\boldsymbol{l}_o\times\boldsymbol{v}_{\rm SO})\Big] \\ &\quad + c^{-3}\Big\{[(\boldsymbol{l}_o\cdot\boldsymbol{v}_{\rm SO})^2 + (1+\gamma)w(r_{\rm SO})]\boldsymbol{l}_o\times(\boldsymbol{v}_{\rm SO}\times\boldsymbol{l}_o) \\ &\quad + \frac{1}{2}(\boldsymbol{l}_o\cdot\boldsymbol{v}_{\rm SO})\boldsymbol{v}_{\rm SO}\times(\boldsymbol{l}_o\times\boldsymbol{v}_{\rm SO})\Big\} + O(c^{-4})\rangle,\end{aligned} \quad (42)$$

where $\boldsymbol{l}_o$ is the light ray direction when it is observed, the absolute value of potential $w(r_{\rm SO})$ is approximated by a spherically symmetric Sun by

$$w(r_{\rm SO}) \approx Gm_\odot/r_{\rm SO}, \quad (43)$$

and γ is a dimensionless parameter in the parameterized post-Newtonian formalism (PPN; Nordtvedt & Will 1972). It is equal to 1 if GR is true. It could be fitted to astrometry data in the case of weak-field relativity tests, although a fully post-Newtonian formulization of the timing, astrometry, and radial velocity models is required to test GR consistently. For strong-field relativity tests, only the PPK parameters (see Equation (22)) are fitted. For the difference between PPN and PPK parameters, we recommend Taylor et al. (1992) for more details. Due to gravitational lensing, $\boldsymbol{l}_o \neq -\boldsymbol{u}_{\rm OT}$.

3.3.2. Atmospheric Refraction

As mentioned in Section 3.2.1, a light ray is refracted when it propagates in the Earth's atmosphere. This effect is one of the main factors that limits the precision of ground-based astrometry (Gubler & Tytler 1998; Mangum & Wallace 2015). We use the routine *slaRefro* in SLALIB[8] to calculate the refraction,

$$\mathcal{R} = \int_1^{n_{\rm O}} \frac{\tan Z}{n}\,dn, \quad (44)$$

where $n_{\rm O}$ is the refractive index at the telescope and Z is the refracted zenith angle. The observed zenith angle Z_o is the sum of the incident zenith angle above the atmosphere Z_i and the refraction:

$$Z_o = Z_i + \mathcal{R}. \quad (45)$$

As $\tan Z$ diverges when Z approaches 90° (see Equation (44)), Auer & Standish (2000) reformulate the integrant as a function of zenith angle, and the refraction becomes

$$\mathcal{R} = -\int_0^{Z_o} \frac{rdn/dr}{n + rdn/dr}dZ, \quad (46)$$

where r is the distance from the geocenter. Because refraction is wavelength dependent, the effective temperature or wavelength of a star should be known in order to calculate the

[8] http://star-www.rl.ac.uk/star/docs/sun67.htx/sun67.html

refraction. By adopting the atmospheric model developed by Rüeger (2002) and using the *slaRefro* routine adapted from the *AREF* routine given by Hohenkerk & Sinclair (1985), we can calculate refraction R to a precision of about 1 arcsec (Mangum & Wallace 2015) and the differential refraction ΔR to a precision of 10 μas (Gubler & Tytler 1998). However, in order to achieve such relative astrometric precision for a typical binary, those authors find that the effective temperature of stars should be measured to a precision of 100 K, absolute zenith angle to a precision of 36 arcsec, relative zenith angle to a precision of 30 mas, air temperature at the observatory to a precision of 0.6 K, air pressure to a precision of 160 Pa, and relative humidity to a precision of 10%. Because the refraction is calculated using the observed zenith in *slaRefro*, we set $Z_o = Z_i$ and repeat the calculation of R until it converges. Because the refraction occurs in the plane formed by the zenith and the incident light ray and is perpendicular to the incident light ray, the refraction vector is

$$\boldsymbol{R} = \frac{\boldsymbol{u}_Z - (\boldsymbol{u}_Z \cdot \boldsymbol{u}_{\rm OT})\boldsymbol{u}_{\rm OT}}{\sin Z} R, \tag{47}$$

where $\boldsymbol{u}_Z$ is the unit vector in the zenith direction. Then the light ray direction when it is observed is

$$\boldsymbol{l}_o = \boldsymbol{l}_i - \boldsymbol{\mathcal{R}}, \tag{48}$$

where $\boldsymbol{l}_i$ is approximately $-\boldsymbol{u}_{\rm OT}$. Such an assumption would at most induce third-order effects.

3.3.3. Gravitational Light Deflection

For a target system outside of the solar system (with heliocentric distance $>10^5$ au), the emitted light from the target star would be deflected by the gravitational fields of companions. This effect is also called gravitational lensing and will also contribute to the Shapiro delay, as discussed in Section 3.2. After Equation (70) of Klioner (2003), we convert the light ray direction at the emission time $\boldsymbol{l}_e$ into the direction after leaving the target system as

$$\boldsymbol{l}_l = \boldsymbol{l}_e - \sum_A \frac{(1+\gamma)Gm_A}{c^2} \times \frac{\boldsymbol{r}_{\rm OT} \times (\boldsymbol{r}_{\rm TA} \times \boldsymbol{r}_{\rm OA})}{|\boldsymbol{r}_{\rm OT}||\boldsymbol{r}_{\rm OA}|(|\boldsymbol{r}_{\rm TA}||\boldsymbol{r}_{\rm OA}| + \boldsymbol{r}_{\rm OA}\boldsymbol{r}_{\rm TA})}, \tag{49}$$

where A denotes the body in the target system parameter and $\gamma = 1$ if GR is assumed. We ignore the gravitational deflection of light that is due to the nonspherical gravitational potential of lenses because it only contributes 1 μas when the light source is very close to the lens (see Table 1 of Klioner 2003 for details).

Assuming vacuum propagation of the light ray between the target and the solar system, the direction of the incident light beyond the atmosphere is

$$\boldsymbol{l}_i = \boldsymbol{l}_l - \sum_{\rm L} \frac{(1+\gamma)Gm_{\rm L}\boldsymbol{d}_{\rm L}}{c^2 d_{\rm L}^2}(1 + \cos\psi_{\rm L}), \tag{50}$$

where $\cos\psi_{\rm L} = \boldsymbol{u}_{\rm OT} \cdot \boldsymbol{r}_{\rm OL}/r_{\rm OL}$ is the angular distance between the light ray and lens L, and $\boldsymbol{d}_{\rm L} = \boldsymbol{l}_e \times (\boldsymbol{r}_{\rm OL} \times \boldsymbol{l}_e)$. For an observer at the geocenter, the light ray does not bend if one assumes the gravitational field of the Earth is spherically symmetric. According to Klioner (2003), the main light deflection is caused by the Sun and the Earth, while the Moon and other planets are only important if the light ray passes them closely.

In summary, the emitted light ray direction is derived from the geometric observed direction using $\boldsymbol{l}_e = -\boldsymbol{u}_{\rm OT}$ with $\boldsymbol{u}_{\rm OT}$ derived from Equation (5). Here, $\boldsymbol{l}_i$ is calculated using Equations (49) and (50). The incident light is further refracted by the atmosphere by $\boldsymbol{\mathcal{R}}$. The direction of the light ray at the telescope is $\boldsymbol{l}_o = \boldsymbol{l}_i - \boldsymbol{\mathcal{R}}$. Then $\hat{\boldsymbol{u}}_o$ is calculated using Equation (42) to model the observed direction of star $\boldsymbol{u}_o$.

3.4. Radial Velocity Model

In this section, we model the observed radial velocity related to the kinematics, geometry, and relativistic effects of the target star and the observer.

3.4.1. Einstein Doppler Shift

In an inertial reference frame, the Schwarzschild solution to the Einstein field equations leads to the following exact ratio between the rate of proper time and the rate of coordinate time for a clock:

$$\frac{d\tau}{dt} = \sqrt{1 - \left(\frac{v^2}{c^2} + \frac{v_e^2}{c^2} + \frac{(v_{||}/c)^2(v_e/c)^2}{1-(v_e/c)^2}\right)}, \tag{51}$$

where $v_{||}$ is the radial velocity of the clock with respect to the inertial frame, and

$$v_e = \sqrt{\sum_i \frac{2Gm_i}{r_i}} \tag{52}$$

is the escape velocity determined by the sum of the gravitational potential of nearby bodies. Applying the above formula to the solar system and the target system and ignoring c^{-4} terms, we derive the increment ratio of the proper observation time τ_o and the proper emission time τ_e as

$$1 + z \equiv \frac{\lambda_o}{\lambda_e} = \frac{\nu_e}{\nu_o} = \frac{d\tau_o}{d\tau_e} = \frac{d\tau_o}{dt_o}\frac{dt_o}{dt_i}\frac{dt_i}{dt_e}\frac{dt_e}{d\tau_e} = \left(1 - \frac{\Phi_{\rm S}}{c^2} - \frac{v_{\rm SO}^2}{2c^2}\right)\left(1 - \frac{\Phi_{\rm T}}{c^2} - \frac{v_{\rm ST}^2}{2c^2}\right)^{-1}\frac{dt_o}{dt_i}\frac{dt_i}{dt_e}, \tag{53}$$

where λ_o and λ_e are respectively the observed and emission wavelength, λ_o and λ_e are respectively the observed and emitted light frequency, $\Phi_{\rm S} = \sum_i \frac{Gm_i}{r_i}$ is the absolute value of gravitational potential of the solar system at the observer's location while $\Phi_{\rm T} = \sum_j \frac{Gm_j}{r_j}$ is the absolute value of gravitational potential of the target system when it emits the light, dt_o/dt_i is determined by the atmospheric refraction, and dt_i/dt_e is determined by Shapiro delay and vacuum propagation. We define

$$z_{\rm grS} \equiv \Phi_{\rm S}/c^2 \tag{54}$$

and

$$z_{\rm grT} \equiv \Phi_{\rm T}/c^2 \tag{55}$$

as gravitational Doppler shifts in the solar and target systems, respectively. We also define

$$z_{\rm srS} \equiv \frac{v_{\rm SO}^2}{2c^2} \tag{56}$$

and

$$z_{\rm srT} \equiv \frac{v_{\rm ST}^2}{2c^2} \tag{57}$$

as the Doppler shifts due to special relativity effects in the solar and target systems, respectively. Because

$$\frac{d\tau_o}{dt_o} = \frac{d{\rm TT}}{d{\rm TCB}} = 1 - z_{\rm grS} + z_{\rm srS}, \tag{58}$$

the relativistic effects on the Doppler shift in the SS can be derived from $\Delta_{\rm eS}$ later in Section 3.2.

For photons emitted from different places on the surface of a star, they experience different gravitational Doppler shifts, especially if there is a massive companion close to the target star. For example, the velocity variation corresponding to the gravitational Doppler shift caused by a Sun-like star located about 1 au from the target star is $3\,{\rm m\,s^{-1}}$. Assuming that the radius of the target star is comparable with the solar radius, which is about $1/215$ au, the differential Doppler shift would lead to about $1\,{\rm cm\,s^{-1}}$ of radial velocity variation. Such a differential Doppler shift should be accounted for together with the rotation-induced differential Doppler shift in the case of exoplanet detection in close binary systems.

3.4.2. Kinematic, Lensing, and Tropospheric Doppler Shift

As discussed in Section 3.2, the emission coordinate time t_e is delayed from the coordinate arrival time of a nonrefracted light ray t_i by

$$t_i - t_e = \Delta_{\rm geo} + \Delta_{\rm sS} + \Delta_{\rm sT}, \tag{59}$$

where

$$\Delta_{\rm geo} = \frac{r_{\rm OT}}{c} \tag{60}$$

is the vacuum propagation time from the target to the observer. The differential of the above delay gives

$$\frac{dt_e}{dt_i} = \frac{1 + z_{\rm kS} - z_{\rm lS}}{1 + z_{\rm kT} - z_{\rm lT}}, \tag{61}$$

where $z_{\rm lS}$ and $z_{\rm lT}$ are respectively the lensing Doppler shift corresponding to the Shapiro delay in the solar system and in the target system. Thus the ratio of time rate is

$$z_{\rm kS} = \frac{\boldsymbol{u}_{\rm OT} \cdot \boldsymbol{v}_{\rm SO}}{c} \tag{62}$$

and

$$z_{\rm kT} = \frac{\boldsymbol{u}_{\rm OT} \cdot \boldsymbol{v}_{\rm ST}}{c}, \tag{63}$$

respectively the kinematic Doppler shift in the solar and target systems. We calculate the relativistic effects by adopting the direction from the observer to the target as in Kopeikin & Schäfer (1999) and Lindegren & Dravins (2003).

In Lindegren & Dravins (2003), the gravitational deflection and the Shapiro delay of the light are not thoroughly treated because of their negligible effects. For example, Lindegren & Dravins (2003) dropped the Shapiro delay term because it contributes at most $0.3\,{\rm m\,s^{-1}}$ radial velocity variation. Although this upper limit is determined from the extreme situation when the light ray grazes the solar limb, the lensing effect for stars with a large angular distance from the Sun can still be important for achieving $1\,{\rm cm\,s^{-1}}$ radial velocity precision, and we consider this further below. Based on a more rigorous treatment of the Shapiro effect in Equations (169), (173), and (238) of Kopeikin & Schäfer (1999), the lensing Doppler shift in the solar system is

$$z_{\rm lS} = \left(\frac{\delta\nu}{\nu_{\rm o}}\right)_S = \sum_{\rm L} \frac{1}{c} \times \left(\boldsymbol{v}_{\rm SL} - \frac{r_{\rm LT}}{r_{\rm OT}}\boldsymbol{v}_{\rm SO} - \frac{r_{\rm OL}}{r_{\rm OT}} \cdot \boldsymbol{v}_{\rm ST}\right) \cdot \boldsymbol{\alpha}(\boldsymbol{\lambda}_{\rm L}), \tag{64}$$

where $\boldsymbol{\lambda}_{\rm L}$ is the impact parameter of the unperturbed path of photons with respect to lens L, and

$$\boldsymbol{\alpha}(\boldsymbol{\lambda}_{\rm L}) = 2(1+\gamma)\frac{Gm_{\rm L}}{c^2\lambda_{\rm L}^2}\boldsymbol{\lambda}_{\rm L}, \tag{65}$$

where $m_{\rm L}$ is the mass of lens L. Ignoring the lensing effects of planets, assuming a static Sun with respect to the SSB, and considering $r_{\rm OA} \ll r_{\rm AT}$ and $r_{\rm OT} \simeq r_{\rm OA} + r_{\rm AT}$, we find that Equation (64) becomes

$$z_{\rm lS} = \left(\frac{\delta\nu}{\nu_{\rm o}}\right)_S = -\frac{\boldsymbol{v}_{\rm SO} \cdot \boldsymbol{\alpha}(\boldsymbol{\lambda}_S)}{c}, \tag{66}$$

where $\boldsymbol{\lambda}_S = \boldsymbol{u}_{\rm OT} \times (\boldsymbol{r}_{\rm OS} \times \boldsymbol{u}_{\rm OT})$. Because the lensing effect is proportional to c^{-3}, the above assumptions would at most have a fourth-order effect. Equation (66) is the lensing formula used in most literature. Similarly, the lensing Doppler shift in the target system is approximately

$$z_{\rm lT} = \left(\frac{\delta\nu}{\nu_{\rm o}}\right)_{\rm T} = -\frac{\boldsymbol{v}_{\rm CT} \cdot \boldsymbol{\alpha}(\boldsymbol{\lambda}_{\rm C})}{c}, \tag{67}$$

where $\boldsymbol{v}_{\rm SC}$ and $\boldsymbol{v}_{\rm ST}$ are respectively the velocity of the companion and target star with respect to the SSB and $\boldsymbol{\lambda}_{\rm C} = \boldsymbol{u}_{\rm OT} \times (\boldsymbol{r}_{\rm OC} \times \boldsymbol{u}_{\rm OT})$. The Sun is the main gravitational lens in the solar system, which induces a gravitational shift of about $\frac{1\,{\rm au}}{\lambda_S}\,{\rm mm\,s^{-1}}$ assuming the observer's tangential velocity of $30\,{\rm km\,s^{-1}}$. For an impact parameter comparable with the solar radius, the shift would be about $0.3\,{\rm m\,s^{-1}}$. The angle between the target source and the light ray from the perspective of the observer ψ should be less than 7° based on Equations (66) and (67) in order to induce $>1\,{\rm cm\,s^{-1}}$ line shift. If the target system is like the solar system, this effect leads to $>1\,{\rm cm\,s^{-1}}$ Doppler shift in edge-on systems. Although the lensing effect is typically ignored in current exoplanet packages such as EXOFAST (Eastman et al. 2013), it could become significant in the search for small planetary signals whose amplitude is comparable with the lensing effect.

Atmospheric refraction not only causes timing delay and deflects light rays but also leads to Doppler shift. The Doppler

shift induced by tropospheric refraction is

$$z_{\rm tropo} = \frac{dt_o}{dt_i} - 1 = \frac{d\Delta_{\rm tropo}}{dt_i} \approx (\Delta_{\rm hydro} m_h'(\Theta) + \Delta_{\rm wz} m_h'(\Theta)) \frac{d\Theta}{dt_i}, \quad (68)$$

where $m_h' = \frac{dm_h}{d\Theta}$ and $m_w' = \frac{dm_w}{d\Theta}$. The differential tropospheric delay is derived numerically using *slaRefro*. The rotation of the Earth leads to a continuous change of the elevation and thus changes the mapping functions m_h and m_w. This effect would induce diurnal radial velocity variation of a few mm s^{-1} for elevation angles lower than 30° if only hydrostatic delay was considered. For elevation angles less than 10°, the refraction could induce up to a few m s^{-1} radial velocity variation due to the exponential variation of refraction near the horizon (see P4 of Figure 15).

By combining all Doppler effects, the Doppler shift is

$$\frac{v_r^{\rm obs}}{c} \equiv z = \frac{1 - z_{\rm grS} - z_{\rm srS}}{1 - z_{\rm grT} - z_{\rm srS}} \times \frac{1 + z_{\rm kT} - z_{\rm lT}}{1 + z_{\rm kS} - z_{\rm lS} - z_{\rm tropo}} - 1. \quad (69)$$

Unlike Wright & Eastman (2014) and Butkevich & Lindegren (2014), we do not explicitly add a term related to the light travel effect. Rather, we calculate the quantities at the corresponding retarded time for a given light ray. We calculate the emitted frequency at the proper emission time according to the time transformation described in Section 3.2. In Equation (69), the special and general relativistic Doppler shifts ($z_{\rm srS}$, $z_{\rm grS}$, $z_{\rm srT}$, and $z_{\rm grT}$) are proportional to c^{-2}, and lensing effects ($z_{\rm lS}$ and $z_{\rm lT}$) lead to $\mathcal{O}(c^{-3})$ Doppler shift. The kinematic Doppler shifts ($z_{\rm kS}$ and $z_{\rm kT}$) are proportional to c^{-1} and are thus significant radial velocity variations. In the case of detection of small planets like the Earth, $z_{\rm kT}$ corresponds to <1 m s^{-1} radial velocity variation, as large as the radial velocity effects caused by some relativistic effects. Thus, a comprehensive modeling of these effects is essential for reliable detection of Earth-like planets.

3.5. Caveats in the Decoupling of the Solar and Target Systems

The so-called "barycentric correction" is typically used to transform the measured radial velocity into the BCRS radial velocity. However, it is only possible if we can separate the local effects and the remote effects caused by the target system. Specifically, the total Doppler shift is split into local and remote Doppler shifts:

$$z = (1 + z_{\rm T})(1 + z_{\rm S}) - 1, \quad (70)$$

$$1 + z_{\rm S} = \frac{1 - z_{\rm grS} - z_{\rm srS}}{1 + z_{\rm kS} - z_{\rm lS} - z_{\rm tropo}}, \quad (71)$$

$$1 + z_{\rm T} = \frac{1 + z_{\rm kT} - z_{\rm lT}}{1 - z_{\rm grT} - z_{\rm srT}}. \quad (72)$$

Although most terms in $z_{\rm S}$ can be precisely determined, $\boldsymbol{u}_{\rm OT}$ is typically not known a priori. For single stars, the error in proper motion may bias the barycentric correction for decades-long radial velocity data. For example, a 10 mas yr^{-1} uncertainty in proper motion would lead to 1.5 cm s^{-1} uncertainty in barycentric correction over one year.

For stars with massive planet companions, the catalog astrometry of the barycenter is biased by the typical assumption of a single star in the data reduction. Because the stellar reflex motion is coupled with Earth's motion (see Equation (5)), a barycentric correction for binaries would not only lead to a spurious trend but also introduce false periodic signals in the corrected radial velocity data. For α Centauri, these false signals lead to sub-m s^{-1} radial velocity variation, hindering the detection of Earth-like planets in this system. Thus, precise barycentric correction is only possible if the stellar reflex orbit is accurately determined a priori. However, this is rarely the case even in the *Gaia* era because the five-parameter astrometry solution assumes no companions around a target star. Even if companions are considered in astrometry modeling, potential uncertainty and bias are expected because of a lack of precise modeling of instrumental bias, stellar activity, and other noise terms.

Two types of biases are caused by barycentric correction:

1. A trend bias is caused by using the barycentric velocity of the target system as the velocity of the target star without considering the stellar reflex motion. This assumption would bias the astrometric solution and thus induce a long-term trend in the radial velocity data. Thus this bias is related to the velocity of the stellar reflex motion and is important for long-term observations.
2. A periodic bias is caused by ignoring the position offset of the target star with respect to the barycenter of the target system. Because the stellar reflex motion is periodic, this assumption would cause periodic variation of the visual direction of the target star, leading to periodic variation of radial velocity. It is important for observations with baselines longer than the period of stellar reflex motion.

Because the Earth's motion is coupled with the barycentric and binary motions, the annual and diurnal Earth motions are manifested in both biases. To estimate the trend bias, we calculate the average reflex motion of the target star as

$$\bar{v}_{\rm reflex} = \frac{m_C}{m_C + m_T}\sqrt{\frac{G(m_C + m_T)}{a}}. \quad (73)$$

The corresponding proper motion bias caused by ignoring this reflex motion is

$$\delta\mu = \bar{v}_{\rm reflex}\frac{\widetilde{\omega}^b}{A}. \quad (74)$$

This proper motion offset leads to a positional bias of

$$\delta u = \delta\mu\delta t \quad (75)$$

over a time span of δt. Assuming that the characteristic radial velocity caused by the motions of the target star and the Earth is $v_{\rm tot} = 50$ km s^{-1}, we estimate the radial velocity bias related to δu as

$$\delta v_r^{\rm trend} = v_{\rm tot}\delta u = 1.52\left(\frac{m_C}{M_\odot}\right)\left(\frac{m_C + m_T}{M_\odot}\right)^{-1/2} \times \left(\frac{a}{\rm au}\right)^{-1/2}\left(\frac{\widetilde{\omega}^b}{\rm mas}\right)\left(\frac{\delta t}{\rm yr}\right) {\rm mm\ s^{-1}}. \quad (76)$$

The corresponding acceleration of the trend bias is

$$\delta \dot{v}_r^{\rm trend} = \frac{\delta v_r^{\rm trend}}{\delta t} = 1.52\left(\frac{m_C}{M_\odot}\right)\left(\frac{m_C + m_T}{M_\odot}\right)^{-1/2} \times \left(\frac{a}{\rm au}\right)^{-1/2}\left(\frac{\varpi^b}{\rm mas}\right) {\rm mm\ s^{-1}\ yr^{-1}}. \quad (77)$$

The periodic bias is determined by the semimajor axis of the stellar reflex motion and is

$$\delta v_r^{\rm period} = v_{\rm tot} a \frac{m_C}{m_C + m_T}\frac{\varpi^b}{A} = 0.24\left(\frac{a}{\rm au}\right)\left(\frac{\varpi^b}{\rm mas}\right) {\rm mm\ s^{-1}}. \quad (78)$$

Considering that the barycentric correction is also frequently used in astrometry and timing, we calculate the time delay biases corresponding to the trend and periodic radial velocity biases, which are

$$\delta\Delta^{\rm trend} = \frac{\delta v_r^{\rm period}}{v_{\rm tot}}\frac{A}{c} = 15.17\left(\frac{m_C}{M_\odot}\right)\left(\frac{m_C + m_T}{M_\odot}\right)^{-1/2} \times \left(\frac{a}{\rm au}\right)^{-1/2}\left(\frac{\varpi^b}{\rm mas}\right)\left(\frac{\delta t}{\rm yr}\right) \mu{\rm s} \quad (79)$$

and

$$\delta\Delta^{\rm periodic} = \frac{\delta v_r^{\rm period}}{v_{\rm tot}}\frac{A}{c} = 2.40\left(\frac{a}{\rm au}\right)\left(\frac{\varpi^b}{\rm mas}\right) \mu{\rm s}. \quad (80)$$

In the above equations, we consider the light travel time from the Earth to the Sun (about 1 au) as the characteristic Roemer delay.

Similarly, the astrometric biases corresponding to the trend and periodic radial velocity biases are

$$\delta u^{\rm trend} = \frac{\delta v_r^{\rm trend}}{v_{\rm tot}} = 6.27\left(\frac{m_C}{M_\odot}\right)\left(\frac{m_C + m_T}{M_\odot}\right)^{-1/2} \times \left(\frac{a}{\rm au}\right)^{-1/2}\left(\frac{\varpi^b}{\rm mas}\right)\left(\frac{\delta t}{\rm yr}\right) {\rm mas} \quad (81)$$

and

$$\delta u^{\rm periodic} = \frac{\delta v_r^{\rm period}}{v_{\rm tot}} = 0.99\left(\frac{a}{\rm au}\right)\left(\frac{\varpi^b}{1\ {\rm mas}}\right) {\rm mas}. \quad (82)$$

Therefore, a radial velocity bias of 1 mm s^{-1} corresponds to a timing bias of 10 μs and an astrometric bias of about 4 mas.

To investigate the influence of the barycentric correction or more generally the decoupling of local and remote effects on the detection of exoplanets, we calculate the boundary of companion mass and orbital period corresponding to a trend bias with an acceleration of 1 mm s^{-1} yr^{-1} and a periodic bias of 1 cm s^{-1} for stars with a heliocentric distance of 1, 10, and 100 pc. We show these boundaries together with the currently known planets in Figure 3. In this figure, we add circles around plotted points to denote planets that are subject to trend bias with an acceleration larger than 1 mm s^{-1} yr^{-1} or periodic bias larger than 1 cm s^{-1}. An acceleration of 1 mm s^{-1} yr^{-1} corresponds to a 1 cm s^{-1}trend bias for observations over one decade. There are only six planets strongly influenced by trend bias. Five of them are transit planets, while one of them is detected through astrometry. They are all massive planets with relatively short orbital periods. The boundaries for trend biases also suggest that short-period, massive planets such as hot Jupiters would induce large stellar reflex motions and thus bias the initial proper motions, leading to a spurious radial velocity trend. On the other hand, the periodic bias is manifested in stars with long-period and massive companions, most of which are detected through direct imaging.

Nevertheless, our estimation of the bias for a given system is only a lower limit because the bias is determined by the largest companion in a system, which might not be detected. Therefore, the boundaries shown in Figure 3 are a better guide for the estimation of decoupling bias because it is calculated for the most massive companion in a system.

Because the transit timing is not sensitive to <0.02 s bias (corresponding to decoupling bias for α Centauri A), a decoupling in timing modeling is efficient and reliable for most transit systems. However, the transit system is sensitive to remote effects such as the transit timing variation (TTV) caused by binary motions. Relative astrometry is sensitive to the astrometry and radial velocity of the TSB (see Equation (10)), which could be biased through decoupling. Absolute astrometry is sensitive to decoupling, and this is why the high-precision astrometry software GREM (Klioner 2003) is used to model all motions simultaneously for *Gaia* astrometry, although its timing model is biased by decoupling effects.

For the radial velocity method, decoupling is unlikely to achieve 1 cm s^{-1} radial velocity precision because even distant close binaries ($d > 1$ kpc) show 1 cm s^{-1} trend bias for decade-long observations. On the other hand, wide binaries (with orbital periods longer than one decade) show strong periodic bias, which can be approximated as a trend for observations with a baseline far shorter than the orbital period. Because nearly half of the solar-type stars are binaries (e.g., Sana & Evans 2011; Moe et al. 2019), a combined modeling of the target and local systems is essential to achieve 1 cm s^{-1} precision over decade-long observations. As illustrated in Figure 3, for nearby stellar systems, planets with hot and cold Jupiter companions are sensitive to trend and periodic biases, respectively. Because most *TESS* targets are close to the Sun, the radial velocity follow-up for hot Jupiters detected by *TESS* may need to consider the trend bias. Specifically, decoupling could introduce ~0.1 m s^{-1} bias in 10 years of radial velocity measurements of a nearby star (<10 pc) with hot or cold Jupiters. It could introduce ~1 m s^{-1} bias over one year for a nearby star hosting stellar-mass companions.

Considering the above difficulties, a separation of local and remote radial velocity effects through decoupling is unlikely to achieve 1 cm s^{-1} precision for decades-long radial velocity data, especially for nearby stars with massive companions (e.g., with a mass >1 $M_{\rm Jup}$). Because astrometry data is essential for a reliable decoupling, a combined modeling of radial velocity and astrometry is the proper way to avoid bias induced by decoupling. Another more efficient approach is to use astrometry offsets or jitter terms to model potential bias and fit these offsets together with the radial velocity model parameters to the radial velocity data "corrected" for barycentric effects.

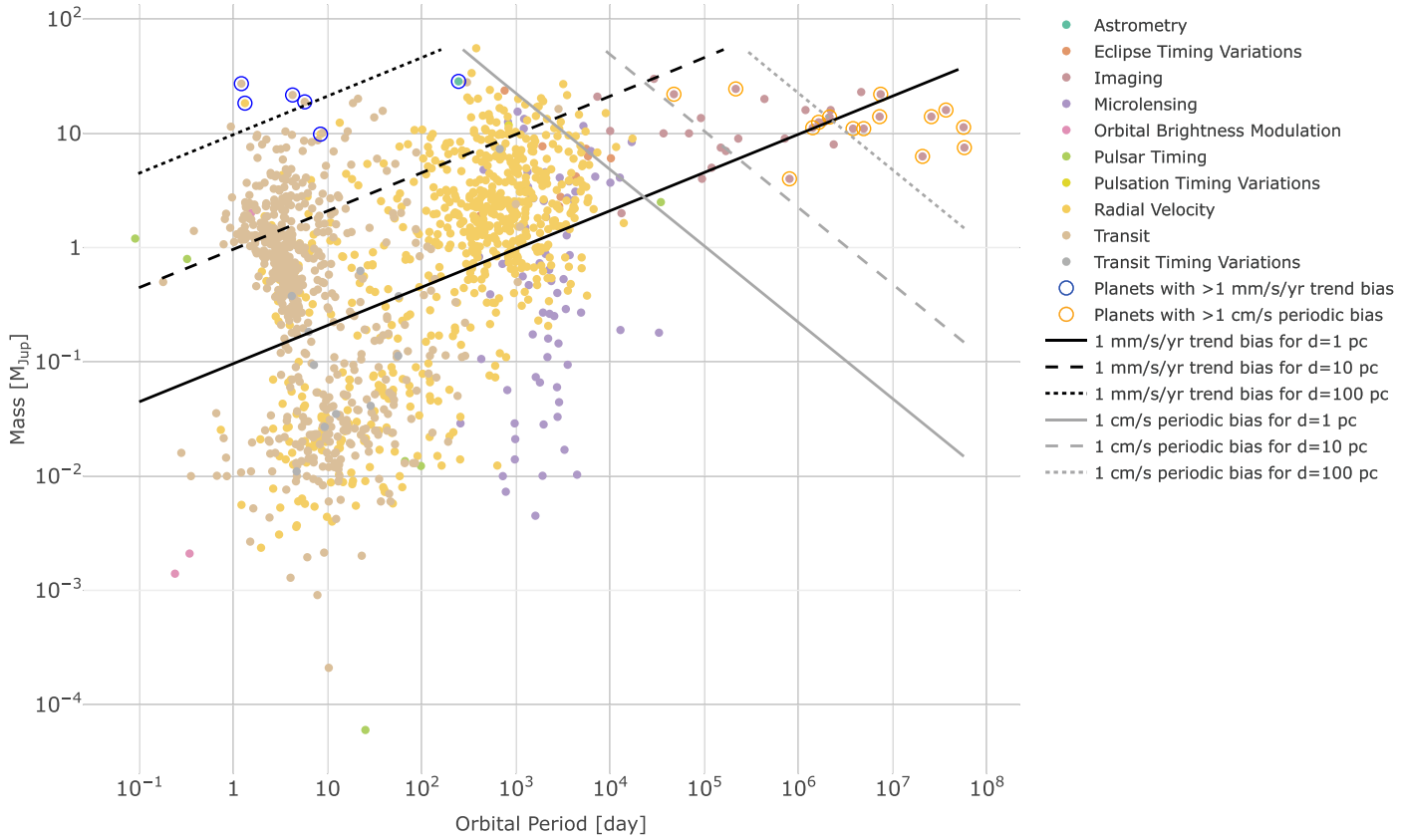

Figure 3. The plot shows exoplanets downloaded from the NASA Exoplanet Archive and color coded for different detection methods as a function of orbital period and planetary mass. The lines on the plot indicate potential radial velocity biases caused by barycentric corrections or more generally by decoupling local and remote effects with the assumption that plotted exoplanets are hosted by single stars. The black lines show the boundaries for the 1 mm s^{-1} yr^{-1} trend bias, while the gray lines show the boundaries for the 1 cm s^{-1} periodic bias. The top left part of the phase space is particularly susceptible to large trend bias, while the top right part of the phase space is particularly susceptible to large periodic bias. The solid, dashed, and dotted lines show the biases for stars with distances $d = 1$, 10, and 100 pc, respectively. The planets denoted by open circles are influenced by at least 1 mm s^{-1} yr^{-1} trend bias or 1 cm s^{-1} periodic bias because of decoupling. The orbital periods for directly imaged planets are derived from their semimajor axes by assuming a face-on circular orbit.

3.6. Significance of Relativistic Effects in Extrasolar Systems

In this section, we investigate the sensitivity of currently confirmed exoplanets to relativistic effects. The main relativistic effect in extrasolar systems is the precession of the longitude of periastron. According to Misner et al. (1973) and Jordán & Bakos (2008), it is

$$\dot{\omega}_{\rm GR} = \frac{3Gm_T}{ac^2(1-e^2)}n = \frac{7.78}{1-e^2}\left(\frac{m_T}{1\,M_\odot}\right) \times \left(\frac{a}{0.05\ \text{au}}\right)^{-1}\left(\frac{P}{1\ \text{day}}\right)^{-1}\text{degree/century}, \quad (83)$$

where $n \equiv [G(m_{\rm T} + m_C)/a^3]^{1/2}$ is the Keplerian mean motion and P is the orbital period. Assuming $m_C \ll m_{\rm T}$, we derive the period–mass boundaries for $e = 0$, 0.5, and 0.9 for $\dot{\omega}_{\rm GR} = 10^\circ$ per century or 1° per decade and show them in the period–mass distribution of currently known planets in Figure 4. There are about 144 transit planets with strong relativistic precession, although the planetary perturbation and tidal deformations may also contribute at a level comparable to the relativistic precession (Jordán & Bakos 2008). However, these nonrelativistic effects only become important when the planet is very close to the star. According to Jordán & Bakos (2008), planetary orbits with semimajor axis larger than 0.05 au are suitable for relativity tests. The precession is detectable in the variation of primary transit duration (Miralda-Escudé 2002) and in the changes of longitude of periastron in radial velocity data (Jordán & Bakos 2008). Although such effects will probably be detected in the near future, the current radial velocity and transit timing data are not likely to be precise enough to put strong constraints on various post-Newtonian theories and to test GR in particular.

Unlike star–planet systems, binaries have relatively stronger gravitational fields and thus are more suitable for relativity testing. Considering that timing data is limited to one-dimensional information, we investigate the feasibility of using astrometry and radial velocity data to test relativity. The former has been studied previously (e.g., Kopeikin & Ozernoy 1999; Klioner 2003; Kopeikin & Makarov 2007). We will focus on the latter by assessing the significance of the Doppler shift induced by special ($z_{\rm srT}$) and general ($z_{\rm grT}$) relativity. Because these two Doppler shifts are proportional to c^{-2}, they dominate the relativistic Doppler shifts in the target system, compared with the lensing Doppler shifts, which are proportional to c^{-3}. Because the constant relativistic Doppler shift is not detectable in radial velocity data, we only estimate the variation of relativistic Doppler shifts. According to Equations (19) and

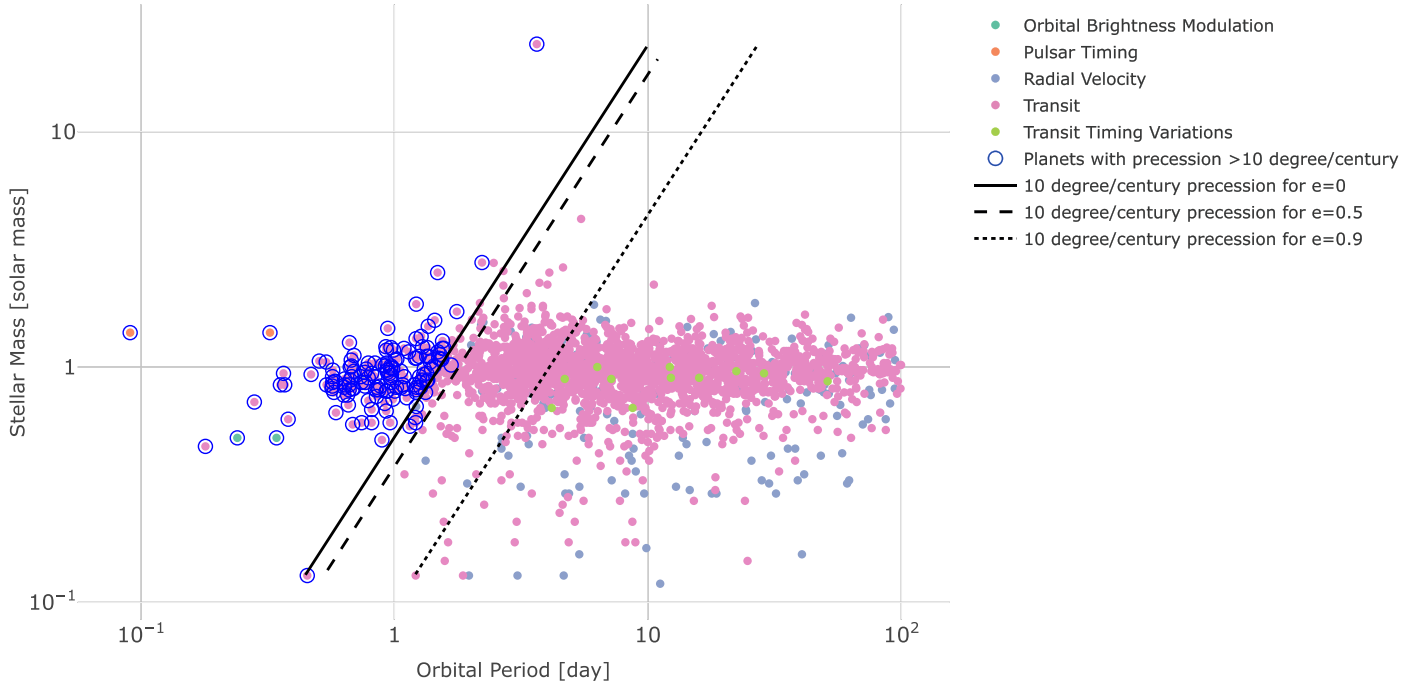

Figure 4. In order to illustrate the detectability of relativistic effects in currently known planetary systems, we select exoplanets with stellar mass larger than 0.1 $M_\odot$ and orbital period less than 100 days from the known exoplanets selected for Figure 3. All of the exoplanets to the left of the solid, dashed, and dotted lines (for $e = 0$, 0.5, and 0.9) are the exoplanets with a precession larger than 10° per century and are highlighted with open circles.

(57), the amplitude of the variation of $z_{\rm srT}$ is

$$\delta z_{\rm srT} = \frac{\delta v_{\rm ST}^2}{2c^2} = \frac{\boldsymbol{v}_{\rm ST,max}^2 - \boldsymbol{v}_{\rm ST,min}^2}{2c^2}, \quad (84)$$

where $\boldsymbol{v}_{\rm ST,max}$ and $\boldsymbol{v}_{\rm ST,min}$ are respectively the maximum and minimum $\boldsymbol{v}_{\rm ST}$. The variation of $(\boldsymbol{v}_{\rm SB} + \boldsymbol{v}_{\rm BT})^2 = v_{\rm SB}^2 + v_{\rm BT}^2 + 2\boldsymbol{v}_{\rm SB} \cdot \boldsymbol{v}_{\rm BT}$ depends on the angle between $\boldsymbol{v}_{\rm SB}$ and $\boldsymbol{v}_{\rm BT}$ and thus depends on the inclination and angular parameters of the binary orbit. To simplify the problem, we explore the range of $\delta z_{\rm srT}$ for a given eccentricity e and barycentric velocity $v_{\rm SB}$. The minimum $\delta z_{\rm srT}$ is

$$\delta z_{\rm srT,min} = \frac{\delta \boldsymbol{v}_{\rm BT}^2}{2c^2} = \frac{v_{\rm BT,max}^2 - v_{\rm BT,min}^2}{2c^2} = \frac{2e}{c^2(1-e^2)}\left[\frac{2\pi G}{P}\right]^{2/3}(m_T + m_C)^{-4/3} m_C^2. \quad (85)$$

Then the minimum amplitude of radial velocity variation induced by special relativity is

$$\delta v_{\rm srT,min} = c\delta z_{\rm srT} = 5.92 \frac{e}{1-e^2}\left(\frac{P}{\rm year}\right)^{-2/3} \times \left(\frac{m_T + m_C}{M_\odot}\right)^{-4/3}\left(\frac{m_C}{M_\odot}\right)^2 {\rm m\ s^{-1}}. \quad (86)$$

The maximum $\delta z_{\rm srT}$ is

$$\delta z_{\rm srT,max} = \frac{(v_{\rm SB} + v_{\rm BT,max})^2 - (v_{\rm SB} - v_{\rm BT,min})^2}{2c^2} = \frac{v_{\rm SB}(v_{\rm BT,max} - v_{\rm BT,min})}{c^2} + \delta z_{\rm srT,min} = v_{\rm SB}\frac{2e}{c^2\sqrt{1-e^2}}\left[\frac{2\pi G}{P}\right]^{1/3} \times (m_T + m_C)^{-2/3} m_C + \delta z_{\rm srT,min}. \quad (87)$$

The maximum amplitude of radial velocity variation induced by special relativity is

$$\delta v_{\rm srT,max} = c\delta z_{\rm srT,max} = \delta v_{\rm srT,min} + \delta v_{\rm srT,couple}, \quad (88)$$

where

$$\delta v_{\rm srT,couple} = 9.94 \frac{e}{\sqrt{1-e^2}}\left(\frac{P}{\rm yr}\right)^{-1/3}\left(\frac{m_T + m_C}{M_\odot}\right)^{-2/3} \times \left(\frac{m_C}{M_\odot}\right)\left(\frac{v_{\rm SB}}{50\ {\rm km\ s^{-1}}}\right) {\rm m\ s^{-1}} \quad (89)$$

is the relativistic radial velocity related to the coupling of the heliocentric motion of the TSB and the binary motion. For α Centauri A, $\delta v_{\rm srT,min} \approx 0.08\ {\rm m\ s^{-1}}$ and $\delta v_{\rm srT,max} \approx 0.61\ {\rm m\ s^{-1}}$ over half of the binary orbital period.

According to Equations (55) and (19), the amplitude of the variation of gravitational Doppler shift for a binary is

$$\delta z_{\rm grT} = \Phi_T/c^2 = \frac{Gm_C}{r_{\rm CT,min}} - \frac{Gm_C}{r_{\rm CT,max}} = \frac{2m_C}{c^2}\frac{e}{1-e^2}\left[\frac{4\pi^2 G^2}{(m_C + m_T)P^2}\right]^{1/3}. \quad (90)$$

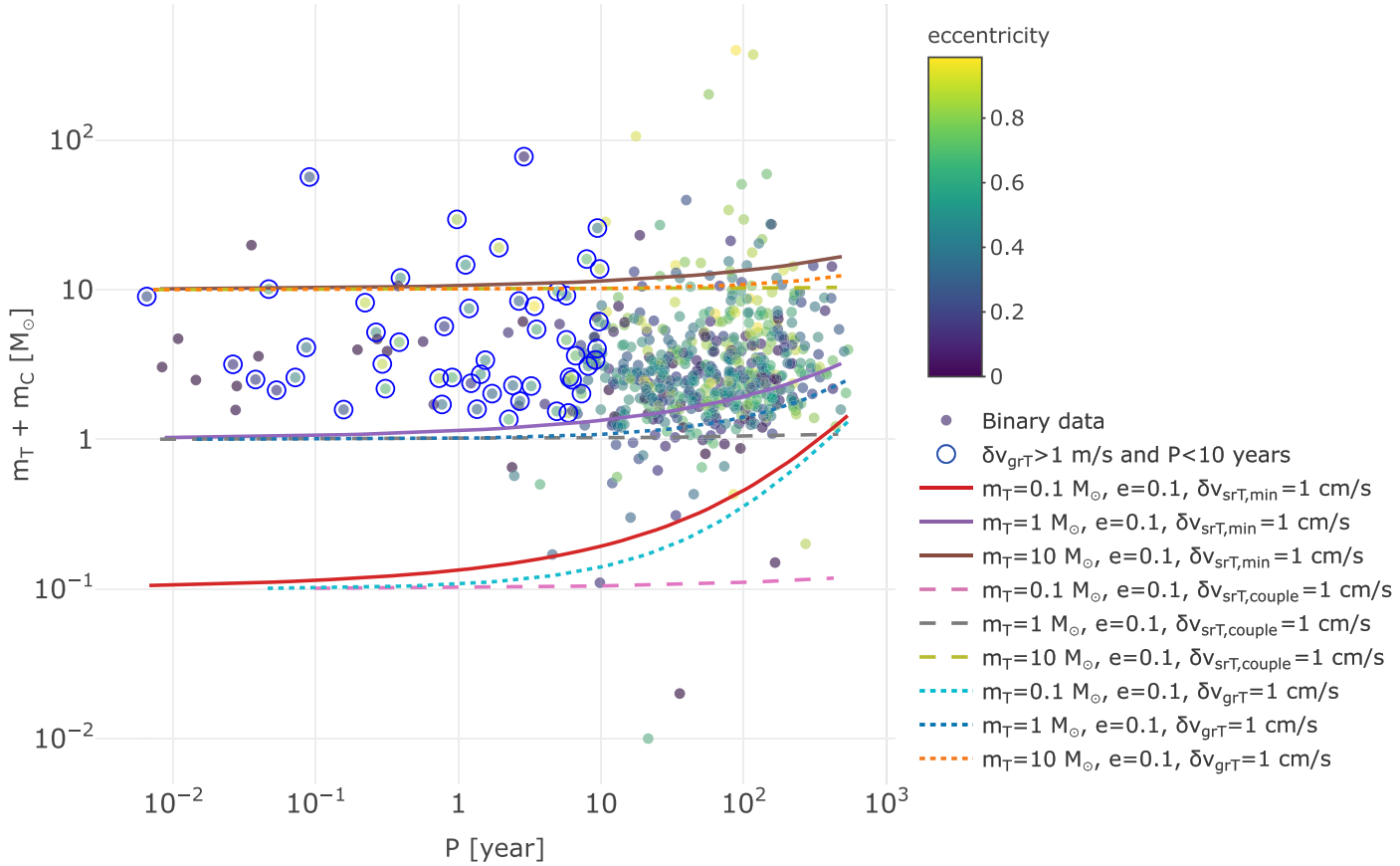

Figure 5. We show the observed binary masses and orbital periods from Malkov et al. (2012) along with period sensitivity for the relativistic radial velocity variation. The three groups of lines are for different values of the mass of target star m_T (0.1, 1, and 10 $M_\odot$). The upper solid lines are for the minimum amplitude of radial velocity induced by special relativity (Equation (86)). The dashed lines are for the relativistic radial velocity related to the coupling of the heliocentric motion of the TSB and the binary motion (Equation (90)). The dotted lines are the amplitude of radial velocity variation due to the gravitational Doppler shift of a binary (Equation (92)). On the basis that primaries and secondaries have the same mass, the 52 binaries with gravitational radial velocity $\delta v_{\rm grT} > 1\,{\rm m\,s^{-1}}$ and orbital period $P < 10$ yr are denoted by blue circles. We note that in all our predictions we assume general relativity to be true and use $e = 0.1$, although a wide range of eccentricity values are observed, as denoted by the colored eccentricity legend.

Hence, the corresponding amplitude of radial velocity variation is

$$\delta v_{\rm grT} = 5.92 \frac{e}{1-e^2}\left(\frac{P}{\rm yr}\right)^{-2/3} \times \left(\frac{m_T + m_C}{M_\odot}\right)^{-1/3}\left(\frac{m_C}{M_\odot}\right) {\rm m\,s^{-1}}. \quad (92)$$

For α Centauri A, $\delta v_{\rm grT} \approx 0.16\,{\rm m\,s^{-1}}$ over half of the binary orbital period.

To investigate the sensitivity of binary orbits to relativistic effects, we show the relativistic radial velocity variation as a function of binary mass and orbital period. We show a sample of 652 binaries with dynamical masses derived by Malkov et al. (2012) in Figure 5. According to Equations (86), (89), (90), and (92), the relativistic radial velocity variation is not sensitive to eccentricity if the binary orbit is not circular (e.g., $e > 0.1$). Because only 8% of binaries in the binary sample have $e < 0.1$, we adopt $e = 0.1$ to more easily calculate the relativistic radial velocity variation. Figure 5 illustrates that the relativistic radial velocity is relatively sensitive to the mass of the secondary m_C for a low-mass primary compared with a high-mass primary. Thus the optimal targets for detecting relativistic effects are the low-mass companions of massive primaries. While many binaries show a relativistic radial velocity variation of a few $\rm cm\,s^{-1}$ over one orbital period, the detection of such a variation is at most marginal and thus is not suitable for relativity tests. To select the optimal targets for relativity tests, we note that there are 52 binaries with $v_{\rm grT} > 1\,{\rm m\,s^{-1}}$ and orbital period $P < 10\,{\rm yr}$. Based on a PPN formulation of the gravitational redshift (e.g., Misner et al. 1973; Kopeikin & Ozernoy 1999; Gravity Collaboration et al. 2018), these binaries can be used to constrain the strong principle of equivalence to a relative precision of 1% if a few $\rm cm\,s^{-1}$ radial velocity precision can be achieved by high-precision spectrographs. Because the gravitational redshift caused by a binary companion has a period that differs from the orbital periods of potential planets around the target star, the gravitational redshift variation can be detected without considering planetary perturbations, although a combined modeling may reduce the residual and improve the significance of detection.

In summary, the gravitational redshift variation in binary systems can provide a new method to test GR. To demonstrate the uniqueness of this method, we show the mass and dimensionless gravitational potential for various relativity tests in Figure 6. Although current efforts are focused on strong-field tests of GR, few tests have been done in the weak-field regime. It is in the extreme weak-field regime where dark matter needs to be invoked to explain phenomena such as galactic rotation and gravitational lensing. However, in the extremely weak

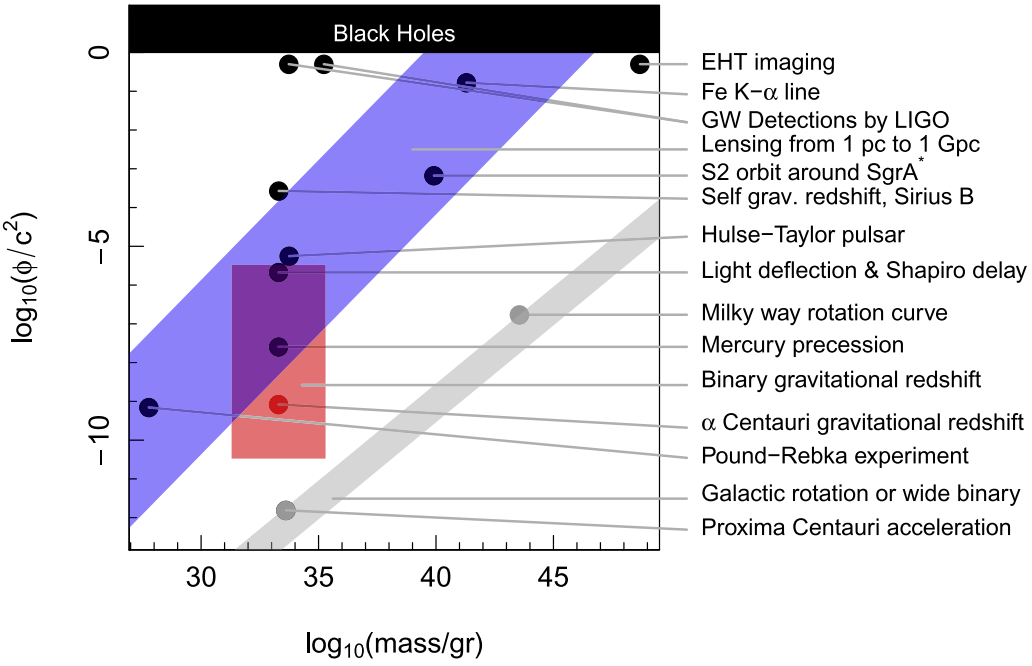

Figure 6. Relativity tests as a function of logarithmic mass and dimensionless gravitational potential, inspired by Psaltis (2004) and Gravity Collaboration et al. (2018). The blue region represents the gravitational lensing effect at the Einstein radius for a reduced distance $d = \frac{d_L d_S}{d_{LS}}$ from 1 pc to 1 Gpc, where d_L and d_S are respectively the distances to the lens and to the source, and d_{LS} is the distance from the lens to the source. The red region represents the binary test with mass from 0.1 to 150 $M_\odot$ and gravitational radial velocity variation from 1 cm s^{-1} to 1 km s^{-1}. The gray region represents the galactic rotation where the width of the gray region is determined by an acceleration ranging from 10^{-12} to 10^{-10} m s^{-2} (Lelli et al. 2017). The black dots show well-established tests (from top to bottom): the imaging of the M87 black hole horizon by Event Horizon Telescope Collaboration et al. (2019), the relativistic broadening of Fe Kα lines (Tanaka et al. 1995; Fabian et al. 2000), the LIGO/Virgo detection of gravitational waves (Abbott et al. 2016, 2017), the S2 orbit around the Galactic-center massive black hole (Gravity Collaboration et al. 2018), the self-gravitational redshift of Sirius B (Greenstein et al. 1971; Barstow et al. 2005), the Hulse–Taylor pulsar (Taylor & Weisberg 1982), the light deflection and Shapiro delay in the solar system (e.g., Shapiro 1964), the precession of Mercury (Einstein 1916), and the Pound & Rebka (1959) experiment. The red dot denotes the gravitational redshift in the α Centauri AB binary system. The gray dots represent tests of dark matter and MOND theories and thus also provide tests of general relativity in a nonrelativistic regime. They are galactic rotation curves represented by the Milky Way and the wide binary acceleration represented by α and Proxima Centauri (Banik & Zhao 2018).

gravitational field, relativistic effects become weak as well, and thus it is not clear whether the weak-field anomaly is due to the breakdown of the classical or relativistic predictions of GR if the null detection of dark matter over the past two decades (Cosine-100 Collaboration et al. 2018) indicates alternative gravity theories. To this end, the binary test of relativity provides a unique way to probe the weak-field and stellar-mass regime in order to test GR and alternative theories such as the modified Newtonian dynamics (MOND; Milgrom 1983).

4. Comparison between PEXO and TEMPO2

To estimate the precision of PEXO, we compare PEXO with TEMPO2, which is able to model timing to a precision of ∼1 ns. Because radial velocity is simply the time derivative of various delay terms, we also use TEMPO2 to estimate the radial velocity model precision of PEXO. However, TEMPO2 does not model astrometry precisely. Because our astrometry model is similar to the model used by GREM (Klioner 2003), which is able to achieve microarcsecond precision, we expect a similar precision for PEXO. Considering that our radial velocity and astrometry models are consistent with each other, we also expect 1 μas precision for the astrometry model if the radial velocity modeling precision is 1 cm s^{-1} for most stars over decades.[9]

4.1. Timing

We use τ Ceti as an example to compare the timing model of PEXO with the one in TEMPO2 and the one introduced by Eastman et al. (2010). The position of τ Ceti is characterized by $\alpha = -15^\circ.93955572$ (ICRF),$\delta = 26^\circ.02136459$ (ICRF), $\varpi = 273.96$ mas, $\mu_\alpha = -1721.05$ mas yr^{-1}, $\mu_\delta = 854.16$ mas yr^{-1}, and radial velocity $v_r = -16.68$ km s^{-1} (*Gaia* Collaboration et al. 2018). We use the online applet developed by E10 to calculate the BJD$_{TDB}$ from JD$_{UTC}$. Because this online applet does not propagate the orbit of the target star, we set μ_α, μ_δ, and v_r to be zero in order to compare with PEXO as well as TEMPO2. We use the GPS position of CTIO determined by Mamajek (2012) as an example observatory geocentric coordinate. We calculate BJD$_{TDB}$ for JD$_{UTC}$ over a 10,000 day time span in a step of 10 days and use the ephemeris of JPL DE405 (Standish 1998) to determine the motions of the Earth and observatory.[10] We use the 2001 version (hereafter FB01) of the analytical method developed by Fairhead & Bretagnon (1990) and recommended by McCarthy & Petit (2004) to calculate TDB-TT for PEXO. The 1990 version (hereafter FB90) is used for TEMPO2 because it is the only available version in TEMPO2. We also use the 2000B model of Earth rotation (Capitaine et al. 2003; McCarthy & Luzum 2003) for TEMPO2 and PEXO.

[9] The velocity precision is $\delta v = 1$ cm s^{-1} =2.109 × 10^{-6} au yr^{-1}. The corresponding astrometry precision $\delta u = v\delta t/d = 2.109 \times 10^{-6}$ au yr^{-1} × 10 yr/10 pc = 2.109 μas, where $d = 10$ pc is the distance of the target star and $\delta t = 10$ yr is the time span.

[10] Because E10 uses DE405 by default, we use DE405 in PEXO for comparison, though DE430 is used in other cases.

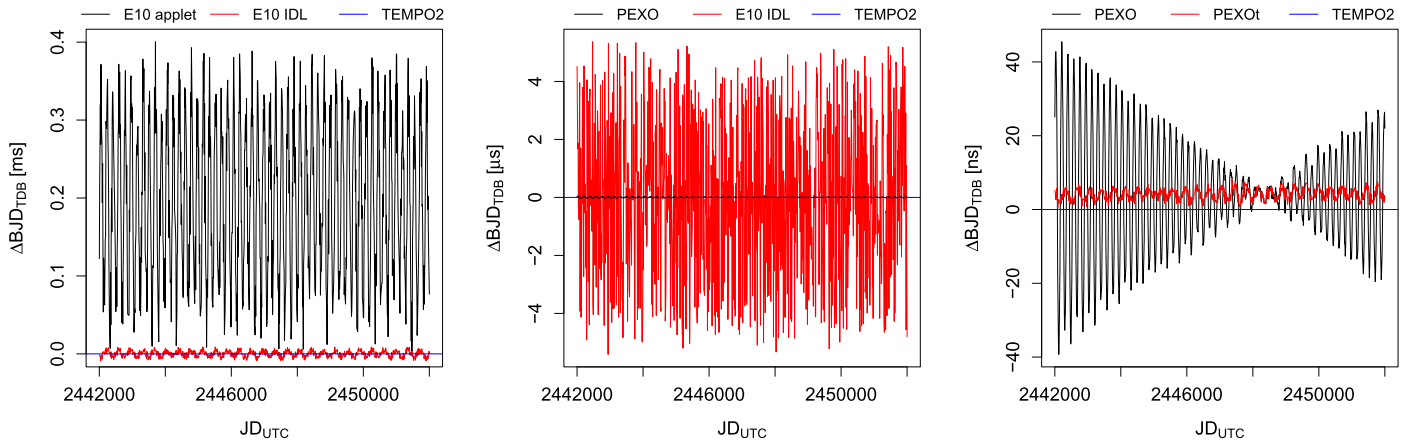

Figure 7. Comparison of $\mathrm{BJD_{TDB}}$ calculated by E10, PEXO, and TEMPO2. Left panel: $\mathrm{BJD_{TDB}}$ modeled by the online applet (black) and IDL version (blue) of E10 after subtraction by the TEMPO2 values. Considering that the applet does not propagate the coordinates of targets, zero proper motion of τ Ceti is assumed. Middle panel: $\mathrm{BJD_{TDB}}$ modeled by E10 and PEXO with respect to the TEMPO2 values. In this comparison, proper motion effects are considered. Right panel: $\mathrm{BJD_{TDB}}$ modeled by PEXO with and without third-and higher-order Roemer delay terms. Because the latter is the approach adopted by TEMPO2, we call it "PEXOt." Proper motion effects are considered in this comparison.

We show the difference in $\mathrm{BJD_{TDB}}$ between the online applet and IDL versions of E10 and TEMPO2 in the left panel of Figure 7. The IDL version gives a few microsecond timing precision, while the applet gives submicrosecond precision due to its use of double precision to store the unreduced JD. However, the original IDL version of E10 has an error in the calculation of "parallax delay" (Equation (32)). In the E10 paper, they correctly add a positive sign in the parallax delay shown in Equation (8) by using $\boldsymbol{u}_{\mathrm{OT}}$ as the reference direction. In the E10 IDL code utc2bjd.pro, the input R.A. and decl. are barycentric, and thus the reference unit vector is $\boldsymbol{u}_{\mathrm{SB}}$. However, E10 calculates the total Roemer delay by adding the parallax delay onto rather than subtracting it from the first-order Roemer delay. The latter is used to calculate the correct Roemer delay shown in the left and middle panels of Figure 7.

To compare PEXO, E10, and TEMPO2 on the same footing, we include all astrometric parameters for τ Ceti and use u_{OT} calculated by PEXO in the IDL version of E10. We compare the three packages in the middle and right panels of Figure 7. We see that the E10 timing precision is about 4 μs, while the PEXO difference from TEMPO2 is less than 50 ns. In the right panel, we compare PEXO with its degraded version ("PEXOt"), which does not include Roemer delay terms higher than two orders (see Section 2.1). The degraded version differs from TEMPO2 by less than 8 ns. There is an offset of $\sim$4 ns due to the different computation methods of TDB-TT. Instead of using the FB90 method to derive TDB-TT like TEMPO2, we use the FB01 method, which is updated and more accurate (Petit & Luzum 2010). We also use DE430t to derive TDB-TT and find a similar offset, suggesting a bias of a few nanoseconds in the FB90 method. The annual variation in $\Delta\mathrm{BJD_{TDB}}$ suggests that the bias caused by FB90 depends on the barycentric distance of the geocenter. The minimum difference between PEXO and TEMPO2 occurs at the reference *Hipparcos* epoch. Therefore, third-order geometric terms shown in Section 2.1 are necessary for a timing model with a precision of $\sim$1 ns. The failure to consider this in TEMPO2 might bias its modeling of decade-long pulsar timing data.

In the Figure 7 comparison of the degraded PEXO (i.e., PEXOt) and TEMPO2, we only account for the Shapiro delay due to the Sun because we find a related bug in TEMPO2. The term $1-\cos(\psi)$ in Equation (34) is implemented as $1+\cos(\psi)$ in the TEMPO2 routine shapiro_delay.C. This will lead to considerable bias in Shapiro delay caused by the solar system planets. We show the Shapiro delays induced by the Sun, Jupiter, Saturn, and Uranus in Figure 8. The Sun is the dominant source of Shapiro delay. Jupiter contributes about 30 ns to the total Shapiro delay and thus is the second important source. Saturn and Uranus contribute about 10 and 1.5 ns, respectively. The other solar system planets only induce less than 1 ns Shapiro delay. Therefore, the Shapiro delays due to the Sun, Jupiter, Saturn, and Uranus are essential components in the model for $\sim$1 ns timing. The Shapiro delay and lensing effects due to Jupiter and Saturn have been detected using very-long-baseline interferometry (Fomalont & Kopeikin 2003; Fomalont et al. 2009). In the timing, astrometry, and radial velocity models of PEXO, Shapiro or lensing effects of the Sun, Mercury, Venus, Earth, Moon, Mars, Jupiter, Saturn, Uranus, and Neptune are considered as standard.

In the comparison shown in Figure 7, we modify PEXO to use a relatively outdated ephemeris, DE405. To assess the significance of ephemeris difference, in Figure 9 we compare the JPL ephemerides DE405 (Standish 1998), DE414 (Standish 2006), DE421 (Folkner et al. 2008), DE435 (Folkner et al. 2016), DE436, and DE438 with DE430 (Folkner et al. 2014). From left to right, the plots in Figure 9 indicate that DE405 and DE414 typically differ from DE 430 and other recent ephemerides by more than 1000 ns in $\mathrm{BJD_{TDB}}$ ($\Delta\mathrm{BJD_{TDB}}$), more than 1 km in barycentric position of the geocenter (r_{SG}), and more than 0.05 mm s^{-1} in barycentric velocity of the geocenter (v_{SG}). DE436 and DE438 differ from DE430 by $\Delta\mathrm{BJD_{TDB}} \sim 400$ ns, $r_{\mathrm{SG}} \sim 200$ m, and $v_{\mathrm{SG}} \sim 0.02$ mm s^{-1}. In contrast, DE435 and DE436 differ from each other by $\Delta\mathrm{BJD_{TDB}} \sim 35$ ns, $r_{\mathrm{SG}} \sim 20$ m, and $v_{\mathrm{SG}} \sim 0.0005$ mm s^{-1}. These stated differences are only a guideline as they are based on average differences and constitute an annual variation superposed on the trend due to perspective change.

The significant difference between DE405 and other ephemerides has been studied frequently (e.g., Viswanathan et al. 2017; Wang et al. 2017). The precision of an ephemeris is determined by the quality of the solar system model, as well as the amount of data available when the ephemeris was computed and fit. Thus we encourage use of the most recent

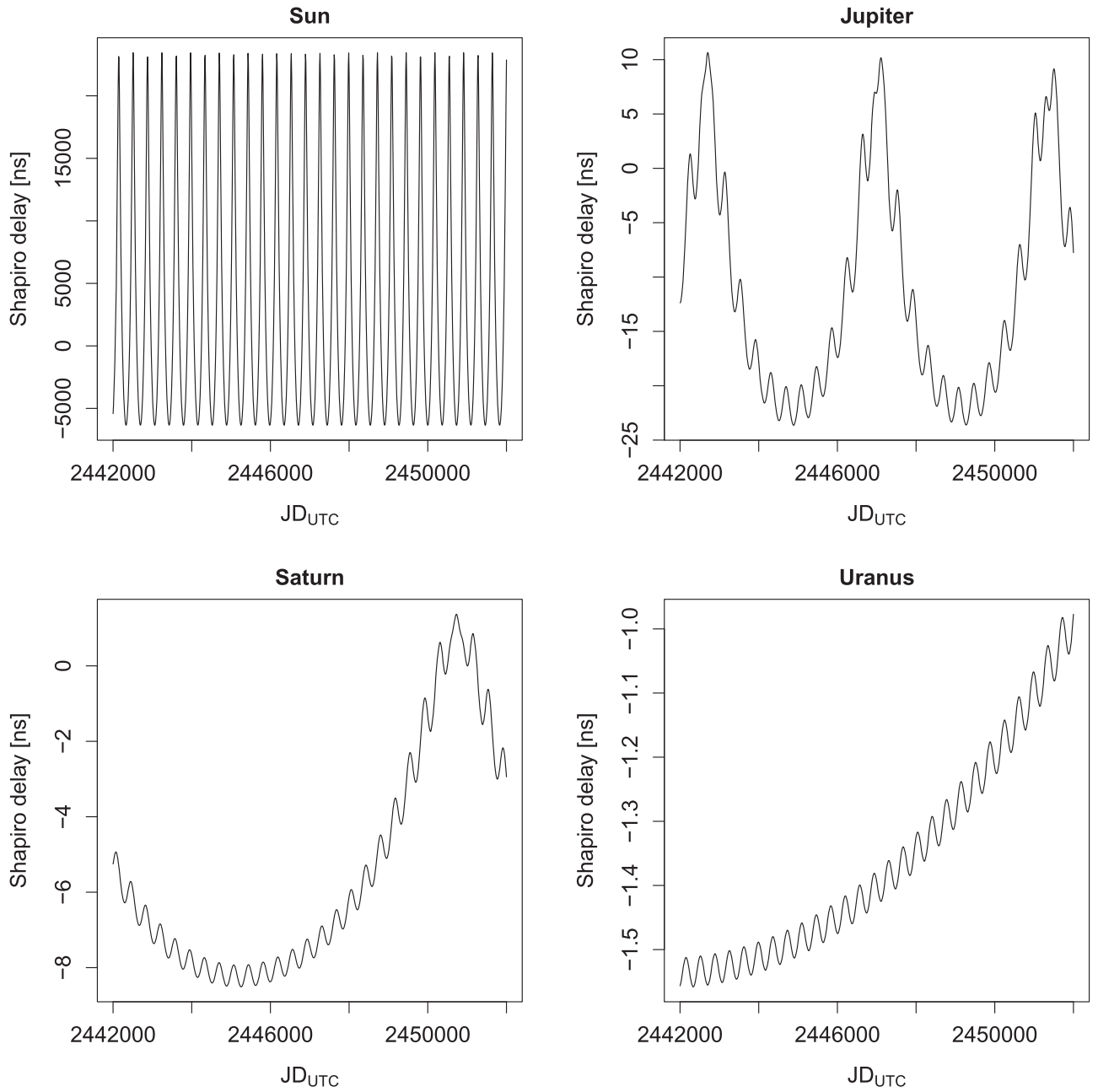

Figure 8. Shapiro delay induced by the Sun, Jupiter, Saturn, and Uranus.

ephemeris if high-precision timing data are analyzed. For the ephemeris DE430 and more recent ones, we expect a timing precision of about 100 ns, a positional precision of about 100 m for the geocenter, and a velocity precision of about 0.01 mm s^{-1}. Thus the timing precision of both PEXO and TEMPO2 is mainly limited by the solar system ephemeris. Potential signals in precise timing data should be analyzed with various ephemerides to confirm, as done by the team of the North American Nanohertz Observatory for Gravitational Waves (NANOGrav; Arzoumanian et al. 2018) to constrain the gravitational-wave background.

To explore precision limits of E10 and TEMPO2 relative to PEXO, we apply them to the nearby star τ Ceti in Figure 10. Considering the lack of third-order Roemer delays and coding errors in TEMPO2, we consider PEXO as the package with the highest precision and compare E10 and TEMPO2 to it in order to explore the precision limit of these well-known packages. We use the Earth rotation model recommended by IAU2006 resolutions (Capitaine & Wallace 2006; Wallace & Capitaine 2006) and the DE430 ephemeris of JPL as well as DE430t to derive TT-TDB. First, we compare the original utc2bjd.pro routine without correcting the error of "parallax delay" with PEXO. We show the results in the left panel of Figure 10. As seen from the left panel, the coding error in E10 leads to about 0.1 ms bias. The ignorance of proper motion leads to about 0.06 s timing bias for τ Ceti over the 30 yr time span (see middle panel of Figure 10). This timing bias will lead to about 2 mm s^{-1} radial velocity bias. This bias could be significant for the analysis of data with high timing resolution, such as fast radio bursts with millisecond resolution (e.g., CHIME/FRB Collaboration et al. 2019). Moreover, proper-motion-induced timing bias is comparable with relativistic precession for some

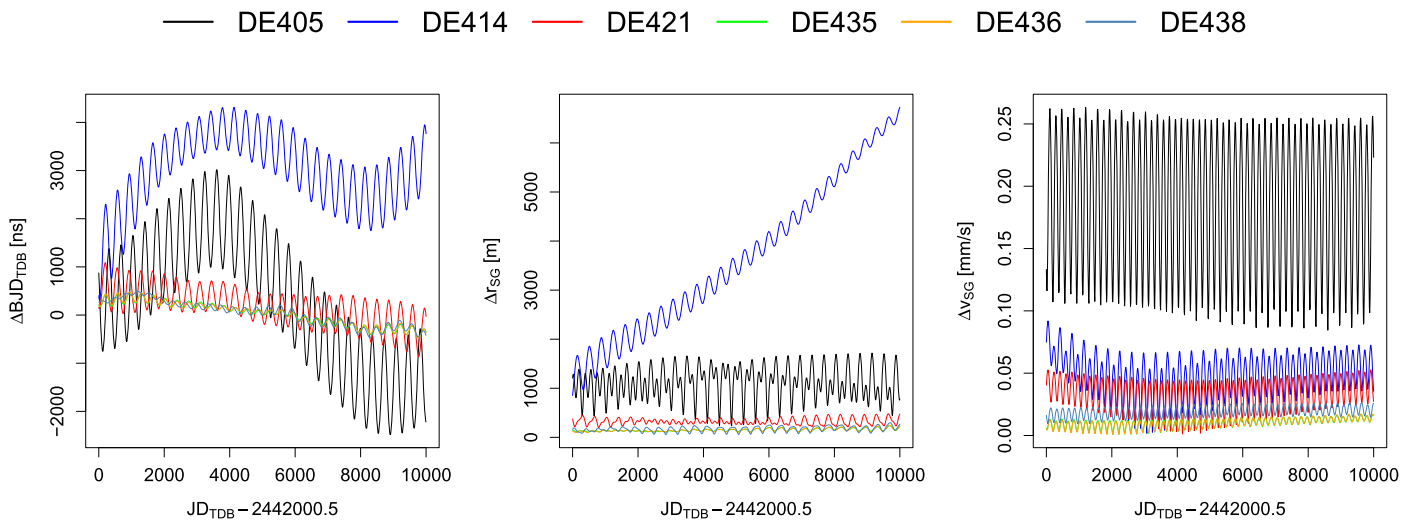

Figure 9. Difference in $\mathrm{BJD_{TDB}}$ (left), barycentric position (middle), and velocity (right) of the geocenter.

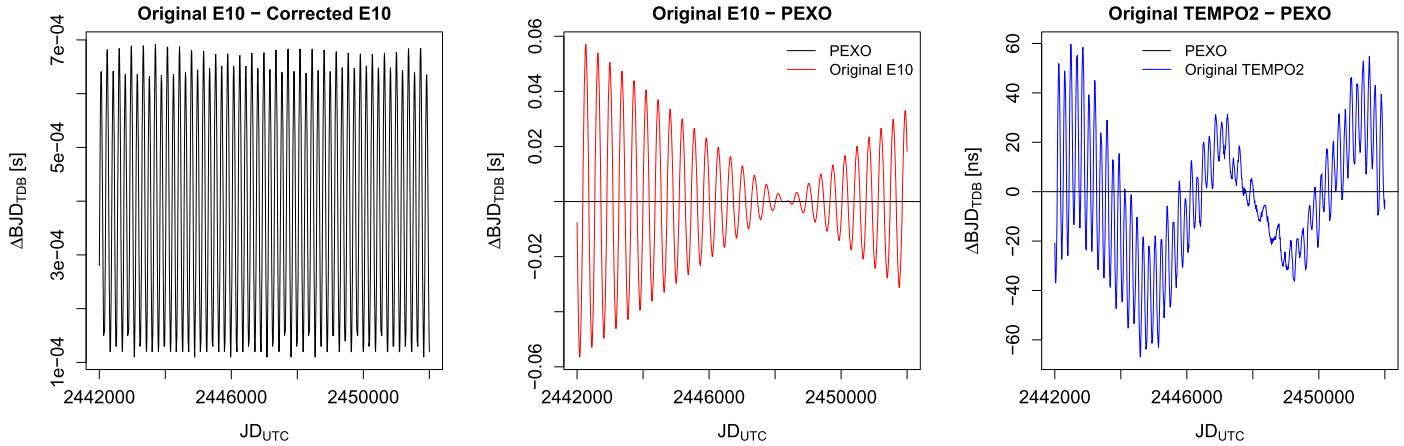

Figure 10. Comparison of the timing precision of E10 and TEMPO2 with PEXO for τ Ceti.

systems and thus needs to be modeled in order to detect relativistic effects in timing data. As seen in the right panel of Figure 10, TEMPO2 and PEXO with the same Earth rotation model and with the DE430 ephemeris are similar at the level of tens of nanoseconds. The original TEMPO2 (with coding error for planetary Shapiro delays) deviates from PEXO due to combined effects of third-order Roemer delays (see the right panel of Figure 7) and planet Shapiro delays (see Figure 8). For distant pulsars, the third-order Roemer delays are not significant, although the coding error in the calculation of planet Shapiro delays still biases TEMPO2 timing by tens of nanoseconds. Therefore, the original TEMPO2 has a timing precision of a few tens of nanoseconds for decade-long observations, and the original E10 has a timing precision of subseconds.

4.2. Radial Velocity

We compare the precision of radial velocity modeling by PEXO and TEMPO2 by calculating the so-called barycentric correction term z_{S} (see Equation (72)). Unlike Wright & Eastman (2014), we do not compare the Doppler shift of pulse frequency with z_{T} because pulse frequency is influenced by aberration delay (E06). We instead calculate Doppler shift numerically using

$$1 + z_{\mathrm{S}} = \frac{\delta \tau_a^{\mathrm{SSB}}}{\delta \tau_o}, \tag{93}$$

where τ_a^{SSB} is $\mathrm{BJD_{TDB}}$ and τ_o is $\mathrm{JD_{UTC}}$. Because the analytical value of the local Doppler shift z_{S} is not given in TEMPO2, we calculate it numerically by using $z_{\mathrm{bary}} = (\mathrm{BJD_{TDB2}} - \mathrm{BJD_{TDB1}})/(\mathrm{JD_{UTC2}} - \mathrm{JD_{UTC1}}) - 1$, where UTC2 and UTC1 are separated by 0.02 day and TDB2 and TDB1 are corresponding TDB times. This UTC time step is chosen such that the rounding error for both PEXO and TEMPO2 can be as small as possible. However, such a numerical treatment is only used for comparison. We use the analytical radial velocity model in Equation (69) for the application of PEXO.

We take τ Ceti as a test case and calculate the local Doppler shift z_{S} numerically for PEXO and TEMPO2. We show the difference in the corresponding radial velocities over 5 yr in Figure 11. We see that the PEXO radial velocities deviate from the TEMPO2 values with a peak-to-peak difference of $2\ \mu\mathrm{m\ s^{-1}}$, indicating a radial velocity precision comparable to TEMPO2.

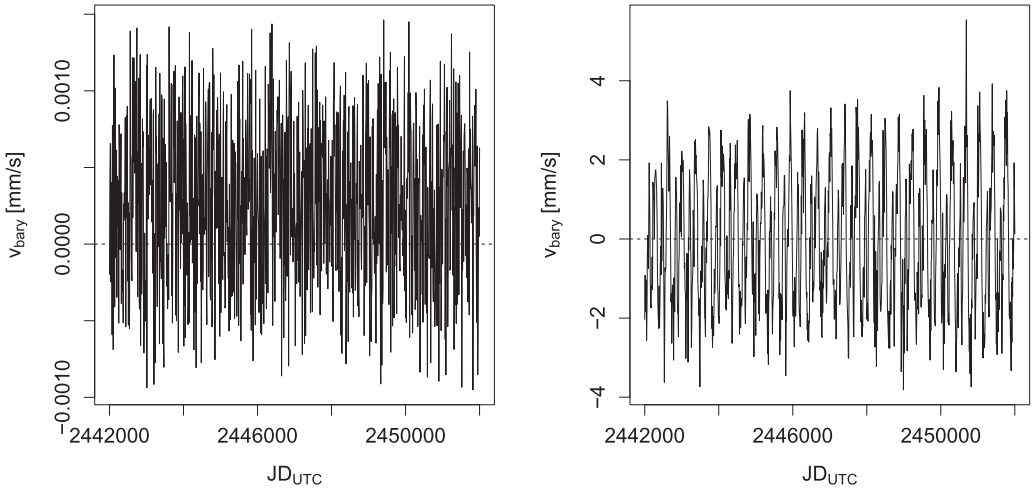

Figure 11. Difference of barycentric correction radial velocity term calculated by PEXO and TEMPO2. The left panel shows the numerical comparison, while the right one shows the analytical comparison.

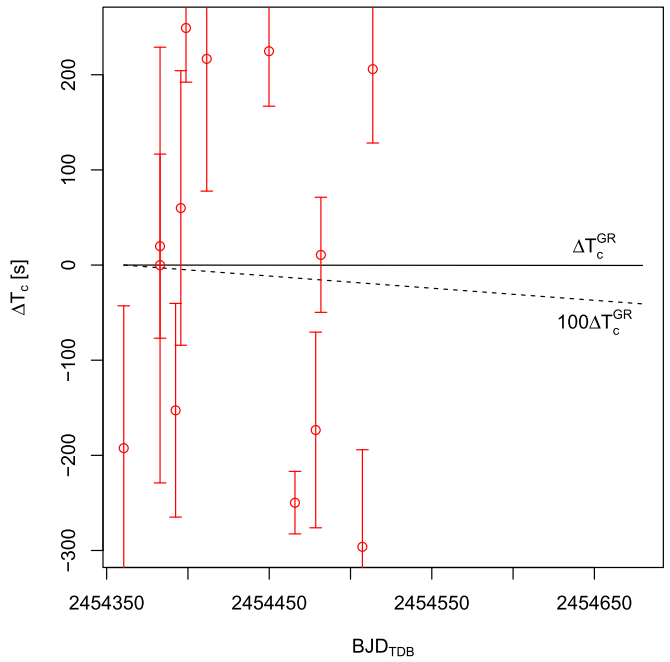

Figure 12. Comparison of the relativistic TTV ($\Delta T_c^{\rm GR}$; black solid line) and observed TTV (red circles with error bars). To visualize the small relativistic TTV signal, we show the amplified relativistic TTV prediction for $100\Delta T_c^{\rm GR}$.

We also compare the analytical PEXO and TEMPO2 models of barycentric radial velocity defined in Equation (28) of Wright & Eastman (2014) and show the results in the right panel of Figure 11. The main error seems to arise from the annual motion of the Earth, which is projected onto the source direction to derive kinematic Doppler shift. Because we use DE430 both for TEMPO2 and for PEXO, the annual variation might be caused by uncertainty in the Earth's rotation model and in the numerical calculation of TDB-TT. Readers are referred to Kopeikin & Ozernoy (1999) for a rigorous treatment of higher-order relativistic Doppler effects.

Therefore, PEXO's radial velocity precision is comfortably beyond the specification of the current best radial velocity instruments such as ESPRESSO (about a few cm s^{-1}). However, a precision at the mm s^{-1} level is only achievable with an ideal treatment of the atmospheric chromatic aberration (Wright & Eastman 2014). The ESPRESSO instrument's exposure meter provides three spectral channels, so in time the identification of possible chromatic effects on exposure time midpoints for radial velocity measurements can be evaluated. A precision of 1 mm s^{-1} is also challenged by the acceleration of the barycenters of the target system and the solar system. The acceleration of the SSB is about 1 mm s^{-1} yr^{-1}, leading to 1 cm s^{-1} bias in the radial velocity model prediction over one decade. This could provide an opportunity to use radial velocity data to estimate the acceleration of stars and thus provide measurements relevant to the Galactic potential analogous to ongoing efforts to quantify cosmological variations in the fine-structure constant (e.g., Whitmore & Murphy 2014).

5. PEXO Simulation of Relativistic Effects in Extrasolar Systems

In this section, we assess various relativistic effects in transit timing, astrometry, and radial velocity models through comparison of PEXO simulations and real data for example systems. These tests are aimed at roughly assessing the precision of PEXO more than detecting relativistic effects in real data.

5.1. Transit Timing

TTV (Miralda-Escudé 2002; Holman & Murray 2005) is an efficient method of constraining the mass and orbital parameters of transiting planets such as the TRAPPIST-1 system (Gillon et al. 2016; Grimm et al. 2018). However, relativistic effects are typically ignored to simplify the TTV modeling because of their small effects, such as in EXOFAST (Eastman et al. 2013), although these effects could be detectable with decade-long observations of some systems (Miralda-Escudé 2002; Jordán & Bakos 2008). To assess the importance of relativistic effects on transit timing, we use XO-3 b (Johns-Krull et al. 2008), a transiting hot Jupiter, as an example because it is a hot Jupiter on an eccentric orbit and is also recommended by Jordán & Bakos (2008) for searching for relativistic precession.

XO-3 b has a mass of 11.79 $M_{\rm Jup}$ and an orbital period of 3.1915239 ± 0.00023 days (Johns-Krull et al. 2008; Winn et al. 2008). We simulate the system over 100 orbital periods using PEXO, calculate the transit epoch for each orbit, and

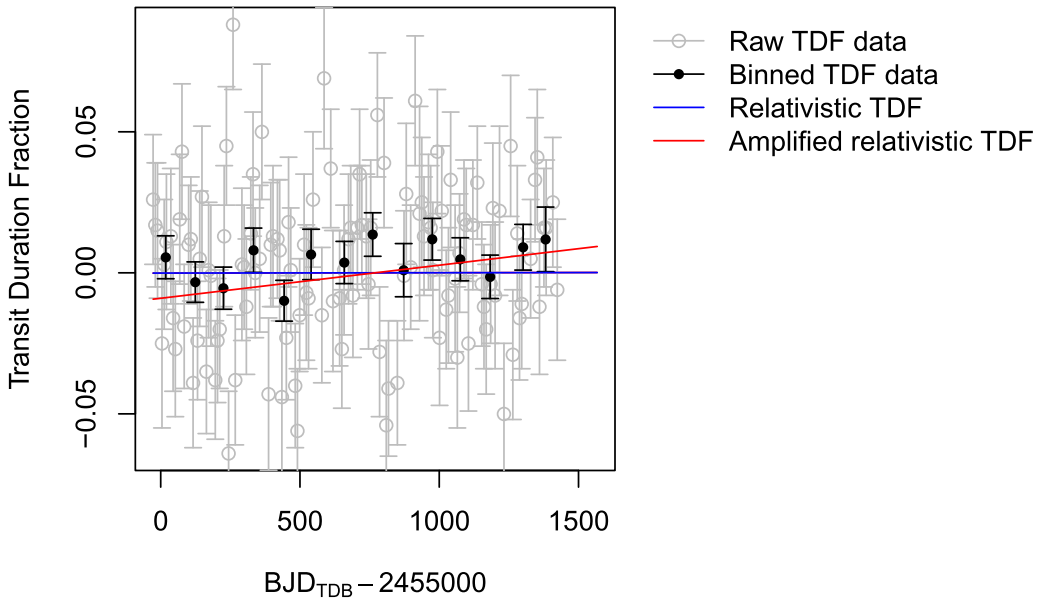

Figure 13. TDF for Kepler-210 over 200 orbits or 1500 days. The blue line denotes the relativistic TDF, while the red line represents the relativistic TDF multiplied by 100. The gray error bars show the raw TDF data, while the black ones are the binned data with a bin width of 100 days.

compare the simulated relativistic TTV with the observed transit timing data (Winn et al. 2008) in Figure 12. The period of primary transits is changed by about 0.4 s over 100 orbits (or about 319 days) due to relativistic precession. This corresponds to a time derivative of transit period of 7.98×10^{-5}, consistent with the prediction using Equation (21) of Miralda-Escudé (2002). Such a signal might be detectable in transit timing measurements with a precision of about one minute for each over one decade. Although such a detection of relativistic TTV is not impossible with current instruments, it is not as efficient as other methods such as Transit Duration Variation (TDV) and the variation of time between primary and secondary transit (PSV). This is because TTV is proportional to $\dot{\omega}_{\rm GR}^2$ while TDV and PSV are proportional to $\dot{\omega}_{\rm GR}$ (Miralda-Escudé 2002).

Because the duration for each transit of XO-3 b is not provided in previous studies, we select Kepler-210 c (Ioannidis et al. 2014) to assess the TDV effect. This planet has an orbital period of 7.9725 days and an eccentricity of 0.5 and thus has significant relativistic precession. We use the transit duration epoch data provided by Holczer et al. (2016) to compare to PEXO predictions. Treating the planet as the target and the star as the companion, we simulate the system over 200 orbits and calculate the velocity $v_{\rm TC}$. We derive the transit duration $\mathrm{TD} = 2\sqrt{(R_{\rm star}+R_{\rm pl})^2-(bR_{\rm star})^2}\big/v_{\rm TC}$, where b is the impact parameter, and $R_{\rm star}$ and $R_{\rm pl}$ are respectively the radii of Kepler-210 and Kepler-210 c. Because Holczer et al. (2016) only provide the epoch data for Transit Duration Fraction ($\mathrm{TDF} = (\mathrm{TD} - \overline{\mathrm{TD}})/\overline{\mathrm{TD}}$), we derive TDF from $v_{\rm TC}$ using $\mathrm{TDF} = (\bar{v}_{\rm TC} - v_{\rm TC})/v_{\rm TC}$ assuming the impact parameter does not change over time. We show the TDF data and the PEXO prediction in Figure 13. To visualize the relativistic TDF properly, we also show an amplified TDF in the figure. The relativistic TDF changes by 1.8×10^{-4} over 1500 days, equivalent to 1.93 s variation in transit duration. This is consistent with the prediction using Equation (23) of Miralda-Escudé (2002) or Equation (15) of Jordán & Bakos (2008). Considering that the mean uncertainty of transit durations is about 4 min and the relativistic precession is about $\dot{\omega}_{\rm GR} = 0.^{\circ}61/\mathrm{century}$, the relativistic TDF is not detectable with the current *Kepler* data for this system. However, such an effect becomes detectable if high-precession systems are observed with high cadence (<10 s) by space- or ground-based telescopes (e.g., Ivanov et al. 2011).

In summary, the relativistic precession is unlikely to be detectable in current transit timing data due to the large timing uncertainty caused by low-cadence observations. For transit systems such as XO-3, the relativistic precession is larger than 1° per century and is thus detectable with high-cadence observations with exposure time as small as a few seconds.

5.2. Astrometry

PEXO is similar to the GREM package (Klioner 2003; Lindegren et al. 2018) used by *Gaia* to model single stars. For binaries or stars hosting massive companions, PEXO also accounts for the gravitational lensing caused by companions in the target system. Additionally, PEXO models the atmospheric refraction in order to account for the differential refraction effects in ground-based direct imaging. For decade-long astrometry data, the parameter uncertainty in an astrometry catalog would lead to significant deviation of model prediction from the real position. For example, a proper motion error of 1 mas yr^{-1} would result in 100 mas position error over one century. Hence, the astrometry parameters should be determined a posteriori in combination with the orbital parameters of companions through Markov chain Monte Carlo (MCMC) posterior sampling. This is also an approach adopted by pulsar timing and is more suitable for precision exoplanet research than the traditional approach, which separates the barycentric correction from the motions in the target system.

To compare the various effects on the measured astrometry, we consider the nearest binary system α Centauri as an example. We use the CTIO observatory as an example observatory site. The orbital and astrometry parameters of α Centauri A and B are determined by Kervella et al. (2016) through a combined radial velocity and astrometry analysis. Based on a simulation of the position of α Centauri A over one orbital period with a time step of 10 days, we compare various

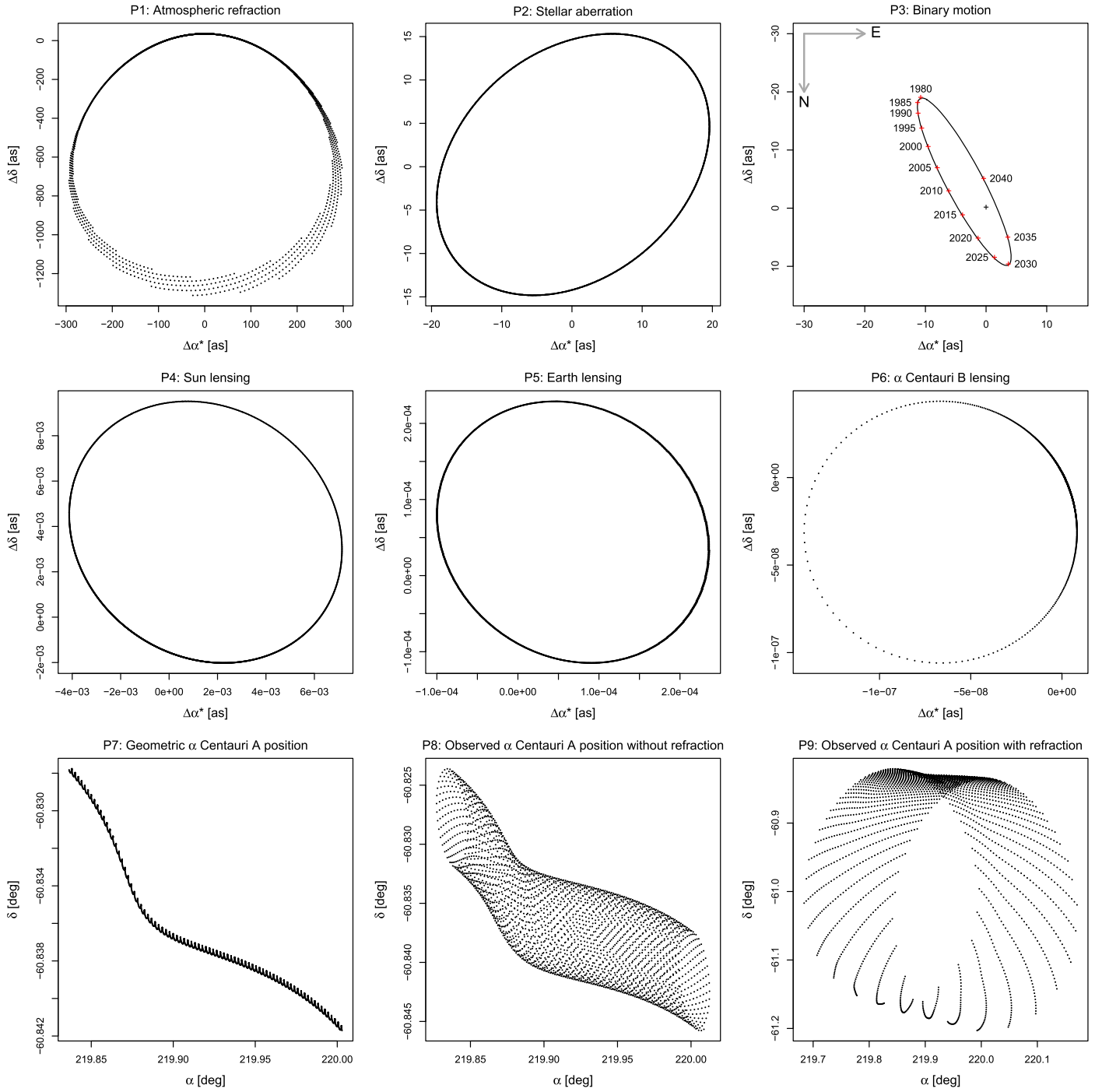

Figure 14. Various effects on the observed position of α Centauri A over an orbital period. The linear proper motion effect is easy to comprehend and thus is not shown here. The panels are denoted by "Pn" where n is the panel number. The names of effects are denoted by the panel titles. For P1 to P6, the panels are ordered in the order of decreasing significance. The plots P7 to P9 in the bottom row show the absolute position of α Centauri A without relativistic and atmospheric refraction effects, without refraction effect, and with all effects, respectively. The binary orbit in P3 shows the motion of α Centauri B with respect to A. It is scaled to be comparable with Figure 1 in Pourbaix et al. (1999). The north (N) and east directions are shown by arrows, and epochs are denoted by red crosses. The black cross represents α Centauri A.

astrometric effects in Figure 14. One of the main position changes is caused by the heliocentric motion of the barycenter of α Centauri. Because it is linear and easy to comprehend, we do not show this effect in the figure. For ground-based observations, the atmospheric refraction (P1 in Figure 14) induces a few arcminute position offset. Because this effect can only be modeled to a precision of about 1 arcsec (Mangum & Wallace 2015), the ground-based astrometry is not able to achieve 1 arcsec absolute precision. The segments of curves in P1 are due to the annual variation of the elevation angle. We use the *slaRefro* routine to calculate the refraction with an effective wavelength of about 500 nm, temperature of 278 K, and relative humidity of 0.1.

The stellar aberration due to the Earth's location (P2) is another main factor alternating the observed direction of α Centauri A. This effect is linearly proportional to the

barycentric velocity of the observatory for ground-based astrometry. Hence, a precise knowledge of Earth's ephemeris and rotation is required to properly model this effect. The third most significant effect is caused by the binary motion (P3). Instead of showing the barycentric motion of A in P3 of Figure 14, we show the orbit of α Centauri B with respect to A and scale the axes such that the binary orbit is comparable with the one shown in Figure 1 of Pourbaix et al. (1999). The good match between P3 and the one in Pourbaix et al. (1999) demonstrates the consistency of our convention (see Appendix A.4 for details) with the ones used in previous studies of visual binaries. Although the binary motion of visual binaries such as α Centauri A and B is significant, it was typically ignored in previous radial velocity modeling due to a decoupling of the solar and target systems. A more rigorous treatment of the stellar motion around the Galactic center is also needed to account for the secular aberration (Kopeikin & Makarov 2006).

The other less significant effects are the gravitational lensing in the solar and target systems. The gravitational lensing effects caused by the Sun (P4) and Earth (P5) are detectable in astrometric data with milliarcsecond and submilliarcsecond precision. As see in the bottom left panel of Figure 14, the annual motion of the Earth is superposed on the binary motion of α Centauri in the solar lensing effect. On the other hand, the lensing effect in the target system only changes the apparent position of the target star by less than 1 μas. According to Kopeikin & Schäfer (1999), the lensing effect due to a companion in the target system is only significant for nearly edge-on systems that host massive companions.

In panels P7 to P9, we show the position of α Centauri A with various combinations of effects. In the geometric position of α Centauri A (P7), we only combine the proper motion, parallax, and binary motion. We see that the orbit is dominated by a linear trend caused by proper motion and a periodic component due to the binary motion. The annual parallax is superposed on this long-term trend. If we add stellar aberration and lensing effects (P8), we find that the aberration adds another dimension to the trend and forms a "tube." The diameter of the tube is determined by the magnitude of stellar aberration. If we combine all effects (P9), the position offset is dominated by the refraction effect. If the elevation angle is large enough, the refraction can be smaller than 1 arcmin, which is still much more significant than other effects.

To see the influence of various effects on relative astrometry, we show the position of B with respect to A in Figure 15. The offset coordinates are defined as

$$\Delta\alpha^* = (\alpha_2 - \alpha_1)\cos\frac{\delta_1 + \delta_2}{2}, \tag{94}$$

$$\Delta\delta = \delta_2 - \delta_1, \tag{95}$$

where (α_1, δ_1) and (α_2, δ_2) are the equatorial coordinates of two points on the celestial sphere that are close to each other. We explain the various effects shown in Figure 15 as follows:

1. P1: Differential refraction. Because we only consider a single wavelength in the calculation of refraction, this refraction effect is achromatic. Chromatic refraction can be calculated simply by applying the *slaRefro* routine to different wavelengths. Despite much scatter and complexity in the pattern observed in the offsets, the differential refraction is less than 0.05 arcsec for most time steps when the elevation angle is higher than 30°. Without properly modeling this differential effect to a submilliarcsecond precision, relative astrometry based on direct imaging would be significantly biased in characterizing exoplanets.
2. P2: Differential refraction. Because we adopt a uniform time step of 10 days, the modulation of elevation and refraction over time is due to the Earth's motion with respect to the SSB.
3. P3: Differential refraction. This panel shows the differential refraction as a function of elevation angle. The upper limit of the differential refraction is determined by the elevation angle, while the binary motion modulates the differential refraction at a given elevation angle.
4. P4: Atmospheric refraction. This panel shows the refraction as a function of elevation. For the atmospheric parameter adopted in this simulation, the absolute refraction is less than 1 arcmin, and the relative refraction is less than 0.05 arcsec if the elevation angle is larger than 30° (see Section 3.4.2). In principle, the current atmospheric model allows a differential refraction model precision of 10 μas (Gubler & Tytler 1998). Parameters such as temperature of the star, local pressure and temperature, and relative humidity may not be well known. As already routinely practiced by some ground-based astrometric programs, it is necessary to observe target systems close to the zenith if submilliarcsecond relative astrometry is required.
5. P5 and P6: Differential aberration. The aberration is determined by the component of $\boldsymbol{r}_{\rm SO}$ that is perpendicular to the target direction. Hence, the aberration is modulated by the Earth's rotation and barycentric motion. Although this effect contributes a few milliarcsecond positional offset (comparable with the astrometric signal induced by a Jupiter analog) and shows strong variation in time, it is rarely considered in analyses of relative astrometry data.
6. P7: Differential solar lensing. This effect is at most a few microarcseconds and thus is only important for future space-based astrometry missions such as the SIM PlanetQuest (Catanzarite et al. 2006; Unwin et al. 2008).
7. P8: Geometric orbit. This is the binary motion projected onto the plane of the sky and is frequently used by the community to model relative astrometry.
8. P9: Observed orbit. This is a combination of geometric and other effects. The atmospheric refraction biases the binary orbit by at most 2 arcsec, producing about 10% of the total offsets. If the system is observed with an elevation angle larger than 30°, we expect <0.05 arcsec refraction bias, equivalent to a 0.2% uncertainty in the binary orbital solution. Without properly removing this bias through modeling, it is unlikely to detect astrometric signals of exoplanets reliably.

Based on the above analyses of the α Centauri orbit, the atmospheric and aberration effects are only marginally important for constraints on its binary orbit based on relative astrometry. However, these effects are far more significant than potential planetary signals. For example, an Earth-like planet around α Centauri B would induce $\sim$1 μas stellar reflex motion, and a Jupiter-like planet would induce $\sim$1 mas reflex motion. Hence, the atmospheric and aberration effects should

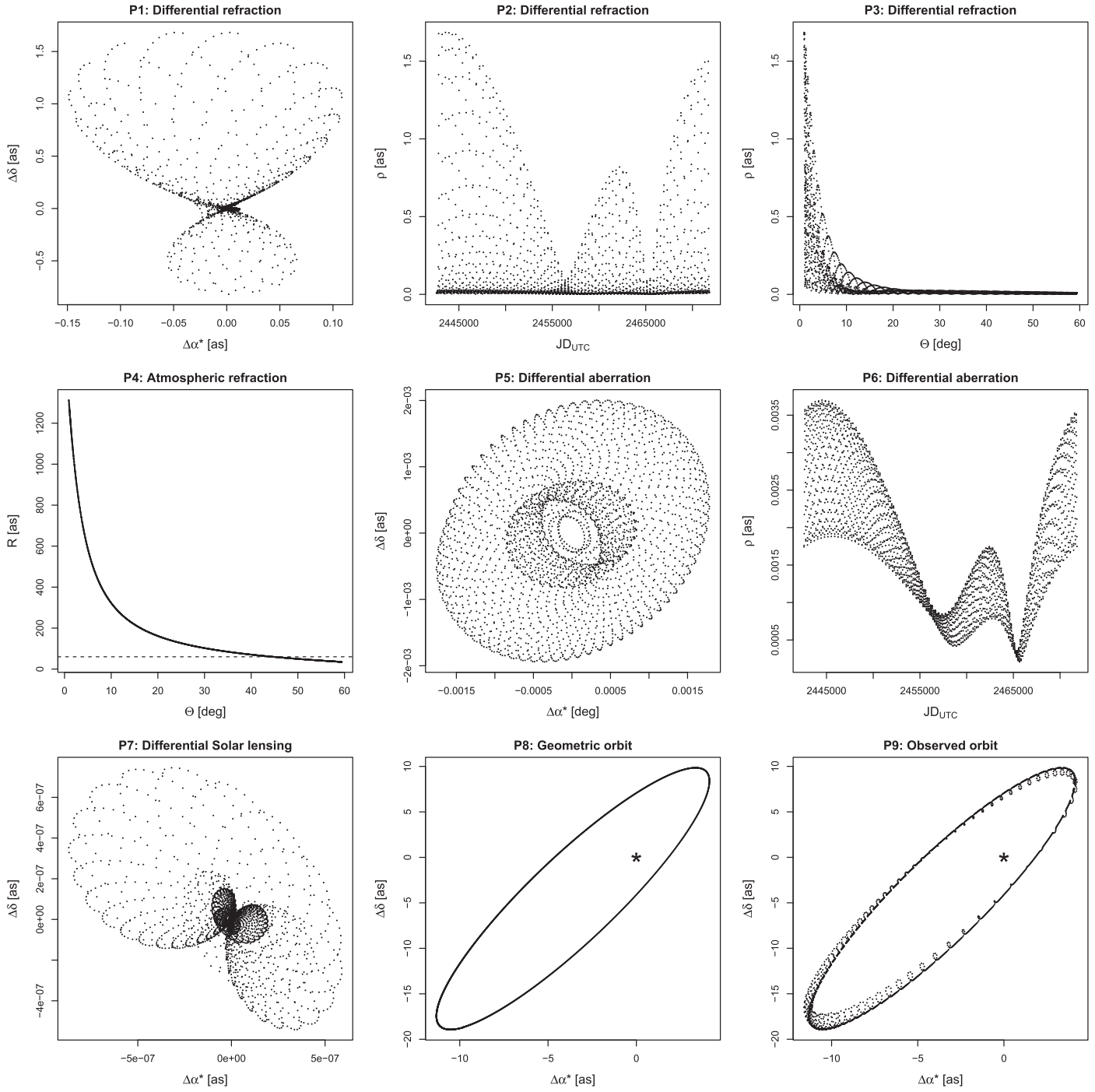

Figure 15. Various effects on the relative position of α Centauri B with respect to A. The differential refraction is shown in the offset coordinates (P1), as a function of time (P2), and as a function of elevation angle (P3). The refraction as a function of elevation angle is shown in P4. The horizontal dashed line indicates a refraction of 1 arcmin. The differential aberrations in the offset coordinates and as a function of time are shown in P5 and P6, respectively. P7 shows the differential solar lensing in offset coordinates. The geometric orbit of B around A without lensing, aberration, and refraction effects is shown in P8. The observed orbit with all effects is shown in P9.

be modeled to a high precision level if solar system analogs are to be detected through the astrometry method.

To roughly test the precision of PEXO prediction, we compare the geometric binary orbit (P8 in Figure 15) with the astrometry data from Kervella et al. (2016). The model and data for the angular separation and the position angle are shown in Figure 16. The small residual suggests that PEXO is able to recover previous results. The observational details for each astrometry data point are beyond this work, so we have not considered the aberration and atmospheric effects that could introduce differential positional offsets.

5.3. Radial Velocity

Adopting the same observatory coordinates and orbital parameters as in Section 5.2, we now consider the relativistic and classical effects on the radial velocities of α Centauri below and show the results in Figure 17:

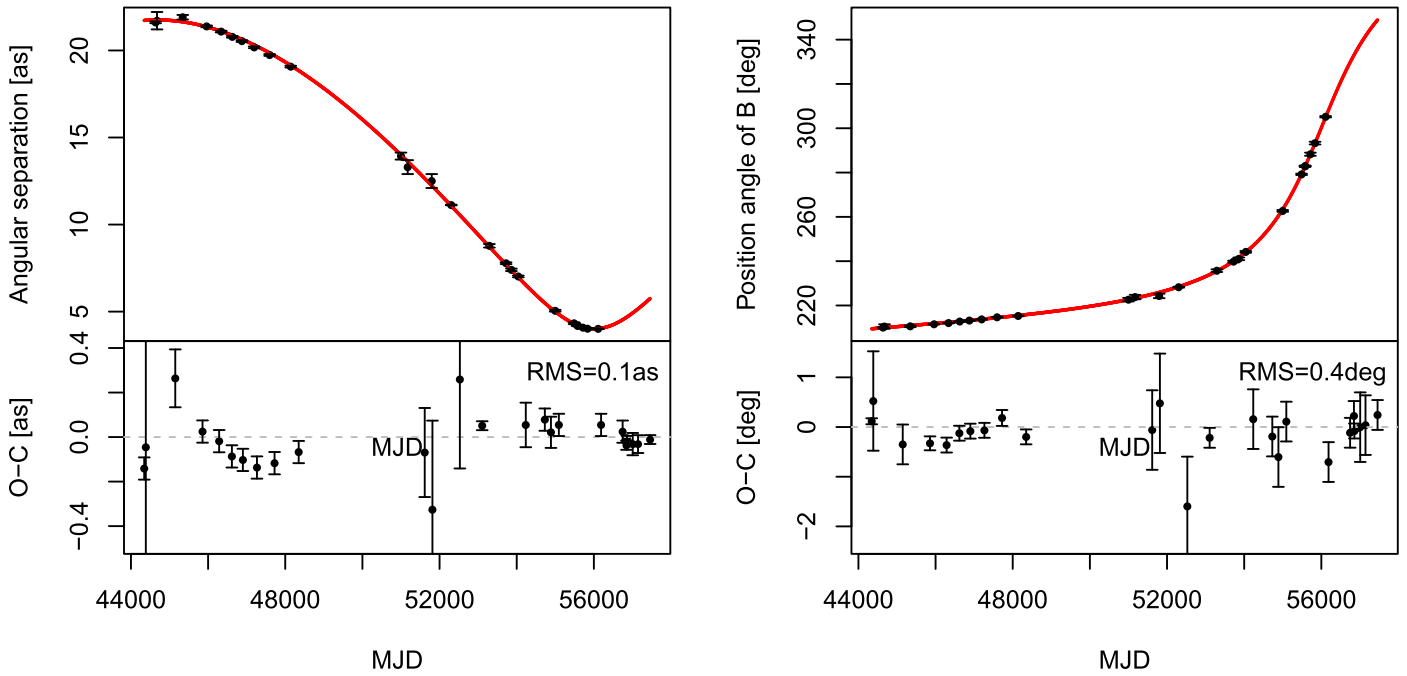

Figure 16. Predicted and observed angular separation (left) and position angle (right) of α Centauri B with respect to A. The red lines denote the best-fit orbital solution given by Kervella et al. (2016). The black error bars denote the astrometry data that the solution is based on and can be visualized in the lower observed–calculated plot.

1. P1: General relativity in the target system. This GR effect is caused by the gravitational field of α Centauri B, which makes the light ray from α Centauri A Doppler shifted. This leads to a radial velocity variation of $0.17\,\mathrm{m\,s^{-1}}$, which is larger than the maximum radial velocity variation of $0.1\,\mathrm{m\,s^{-1}}$ that would be caused by the presence of any Earth-like planets around α Centauri A. To the best of our knowledge, this effect is not considered in current radial velocity analysis packages.
2. P2: Special relativity in the target system.This is a special relativity effect that is due to the motion of α Centauri A around the barycenter of the binary. This effect contributes to a radial velocity variation of $0.53\,\mathrm{m\,s^{-1}}$ over one orbital period and again does not appear to be included in existing radial velocity packages.
3. P3: Motion of the target with respect to the TSB. This radial velocity variation is due to the motion of α Centauri A around the binary barycenter. This motion is typically ignored for the barycentric correction, although it can be determined a priori if the Keplerian parameters of the binary motion are known to a high precision.
4. P4: Motion of the TSB with respect to the SSB. This is a kinematic effect due to the relative motion of the TSB with respect to the SSB. This motion would change the viewing perspective and lead to the so-called "perspective acceleration" in radial velocity. This perspective acceleration is coupled with the binary motion and the observer's motion in the solar system. This is evident in the corresponding radial velocity acceleration shown in Figure 18. The mean acceleration is the perspective acceleration, the short periodic variation is due to the Earth's annual motion around the Sun, and the long periodic variation is caused by the binary motion of α Centauri A and B. This time-varying acceleration casts doubt on the reliability of subtracting a linear trend with a constant perspective acceleration from the radial velocity data (e.g., Zechmeister et al. 2013).
5. P5: Lensing in the target system. This effect corresponds to the gravitational lensing of the companion, which is α Centauri B in this case. This effect contributes at most a $0.1\,\mathrm{mm\,s^{-1}}$ radial velocity variation. Considering that this effect is proportional to the inclination and the semimajor axis, it might be detectable with radial velocity instruments such as ESPRESSO in a nearly edge-on binary system, in short-period binaries, and in transiting systems hosting massive, short-period planets.
6. P6: Lensing in the solar system. This effect is due to the gravitational lensing of the Sun and the Earth, contributing to a $0.1\,\mathrm{mm\,s^{-1}}$ radial velocity variation. This effect is proportional to $\cot\psi/2$ (Klioner 2003), where ψ is the angular distance between the Sun and the target star. Considering that the minimum ψ is 40° for the α Centauri example, the lensing effect would contribute to $1\,\mathrm{cm\,s^{-1}}$ if the target star is less than 1° from the Sun.
7. P7: Relativistic effects in the solar system. These effects are due to the gravitational field in the solar system and the barycentric motion of the observer. These effects also cause the Einstein delay, which transforms TT to TCB. The ratio of the increments of TT and TCB is simply the relativistic Doppler shift. Because the motion of the observatory in the solar system is derived from the JPL ephemeris, we can subtract this type of radial velocity variation directly from the measured radial velocity to remove these local effects. However, in the cases that the observatory site or the ephemeris is not well determined, the Earth's motion as well as the motions of the target star should be determined a posteriori.
8. P8: Motion of geocenter with respect to the solar system barycenter. This effect is due to the barycentric motion of the geocenter and contributes about a $20\,\mathrm{km\,s^{-1}}$ radial

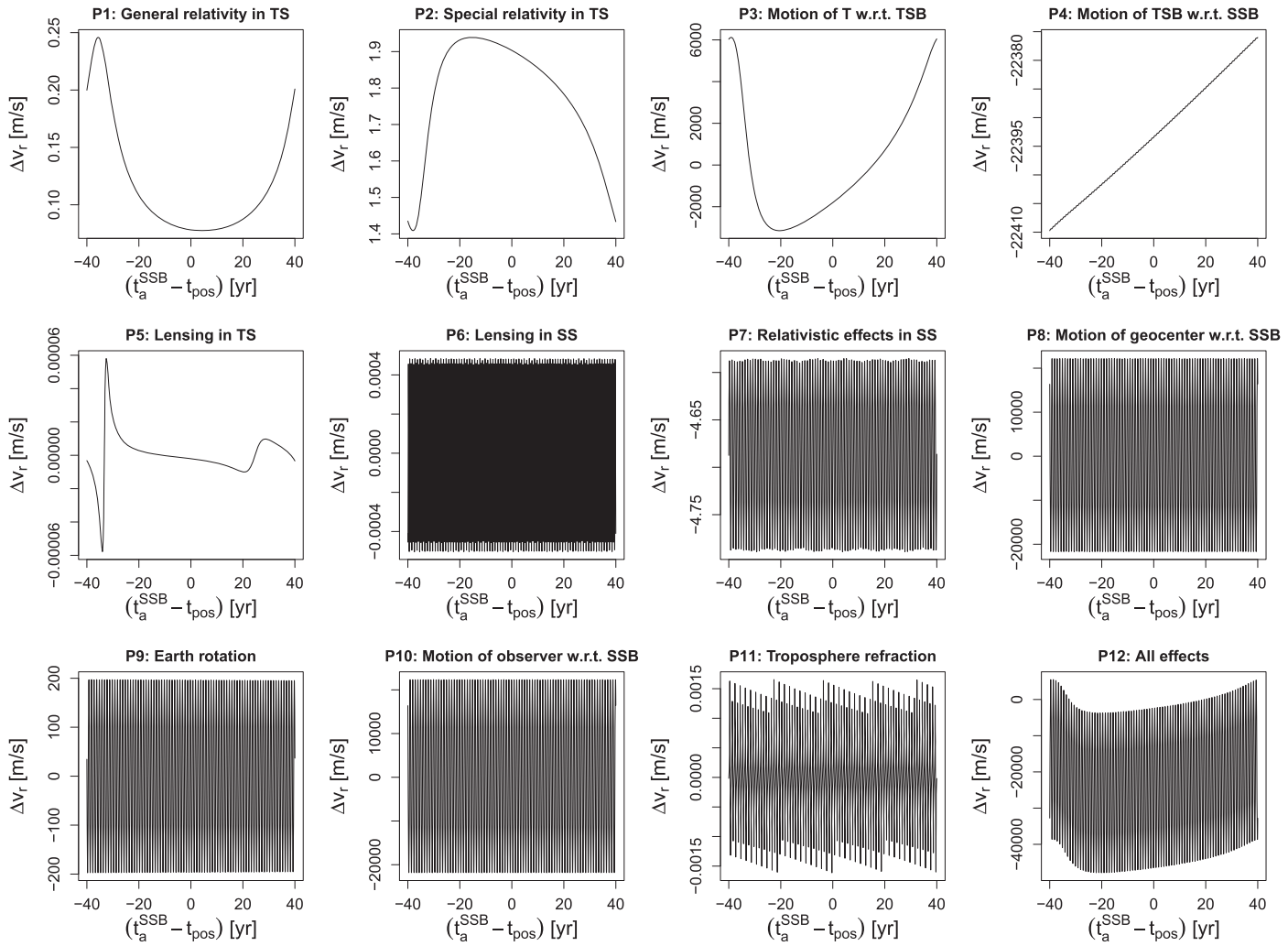

Figure 17. Relativistic and classical effects on the measured radial velocity of α Centauri A over an orbital period.

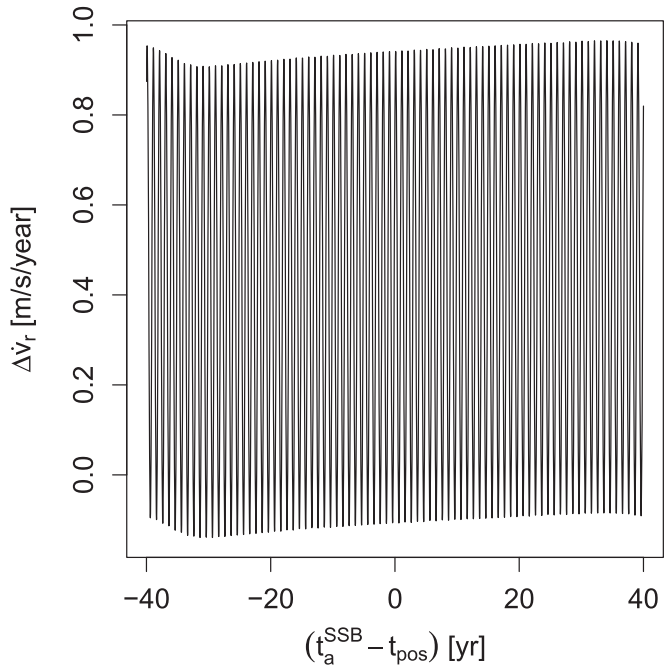

Figure 18. Radial velocity acceleration induced by the motion of the barycenter of α Centauri relative to the SSB.

velocity variation. Such significant kinematic effects are not completely local because the corresponding radial velocity variation depends on the direction of the target, which changes over time due to the motion of the target star.

9. P9: Earth rotation. This effect is due to the Earth's rotation and contributes to a 200 m s^{-1} variation. Hence, the radial velocity data precision highly depends on the Earth rotation model. Specifically, a radial velocity precision of 1 cm s^{-1} requires 1 cm s^{-1} modeling precision of the Earth rotation. Alternatively, the Earth's rotation can be determined a posterori through a fit of the combined model to the data.
10. P10: Motion of observer with respect to the SSB. It is a combination of the P9 and P10 effects.
11. P11: Troposphere refraction. In this panel, we show refraction-induced radial velocity variation for elevation angles larger than 10° to be representative of most ground-based observations. This indicates at most a few mm s^{-1} variation in radial velocity, and thus refraction-induced effects are negligible for the current radial velocity observations.
12. P12: All effects. This is the observed radial velocity, which is a combination of all effects.

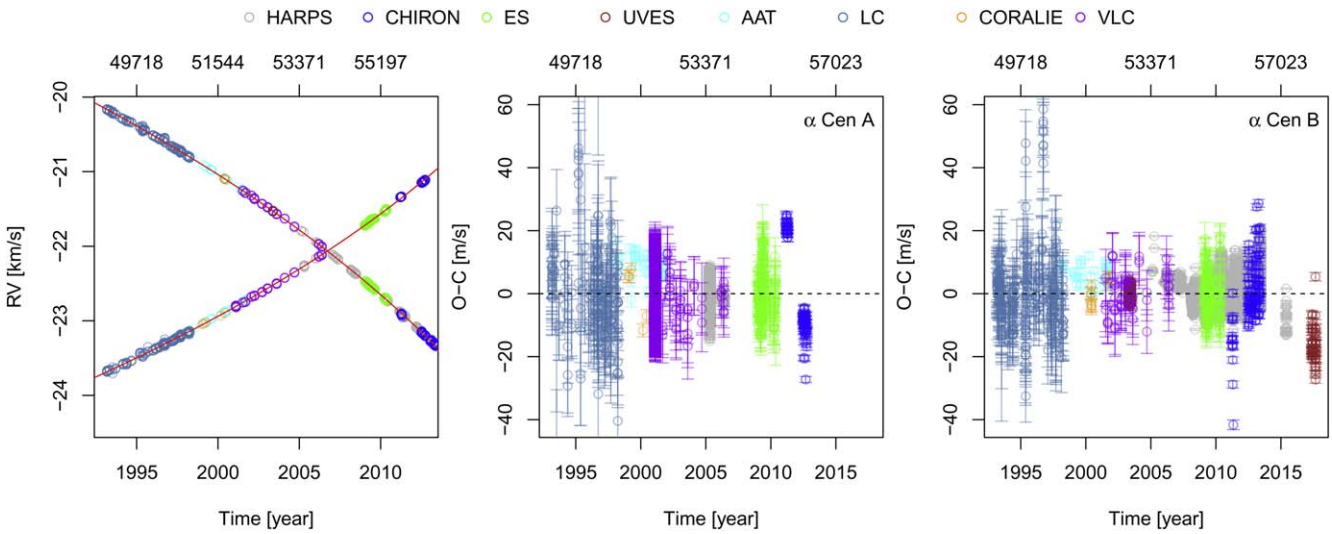

Figure 19. Comparison of the radial velocity model prediction and the radial velocity data sets from various sources. The red line shows the model prediction based on the solution given by Kervella et al. (2016). Left panel: model prediction and observed radial velocities of α Centauri A and B; middle panel: radial velocity residual for α Centauri A; right panel: radial velocity residual for α Centauri B. In each panel, the top axis shows the modified Julian date (MJD = JD-2,400,000.5). The HARPS data is from Lisogorskyi et al. (2019), the CHIRON and ES data sets are from Zhao et al. (2018), the UVES data is obtained by Kjeldsen et al. (2005), the AAT and CORALIE data are from Pourbaix et al. (2002), and the LC and VLC data are from Endl et al. (2001).

We further assess the performance of PEXO by comparing the PEXO model prediction of radial velocity with the radial velocity data in the literature in Figure 19. For data sets with relative radial velocities, we add an offset so that the mean predicted and observed radial velocities are equal. It is obvious that the PEXO prediction well fits the combined data, leading to 4.7 and 4.2 m s^{-1} standard deviations of residual radial velocities for α Centauri A and B, respectively. Nevertheless, we still see significant variations in the CHIRON and HARPS data sets, indicating potential bias in the Kervella et al. (2016) solution and in the barycentric correction. To mitigate such biases, a comprehensive modeling of the α Centauri system is needed and is beyond the scope of this work.

5.4. Comparison of Relativistic Effects on Timing, Astrometry, and Radial Velocities between Different Packages

We apply PEXO to simulate the timing, astrometry, and radial velocity of τ Ceti, α Centauri A, and XO-3 over one decade to assess the significance of various effects. In the XO-3 system, we treat XO-3 b as the primary and XO-3 as the secondary so that the timing model can be used to predict transit timing, the astrometry model is applicable to the relative astrometry of directly imaged planets, and the radial velocity model can be used in studies of systems such as the S2-Sgr A* system (Gravity Collaboration et al. 2018). Additionally, we compare the functions in PEXO with those in TEMPO2, EXOFAST+,[11] and GREM[12] and show the results in Table 1.

Although TEMPO2 is able to model radial velocity by differentiating the timing function over time, such a numerical treatment is likely to result in significant rounding errors due to the huge scale difference between various quantities. The pulse frequency in TEMPO2 is not the same as the light frequency; for example, the light from a star can be gravitationally redshifted while the rotation frequency of a pulsar cannot. Thus, TEMPO2 is not optimal for radial velocity modeling, especially in the case of exoplanet detections.

As seen in Table 1, TEMPO2 provides a precise timing model by including many high-order effects, EXOFAST+ includes some relativistic effects in timing and radial velocity, and GREM is able to model astrometry to a high precision. In comparison with these packages, PEXO aims to include most high-order effects while also providing a combined modeling of timing, astrometry, and radial velocity. As shown in the table, the significant time delay not included in EXOFAST+ and GREM is the Einstein delay in the target system, which is about 0.01 s for α Centauri A and XO-3 b. The Einstein delay in α Centauri over one binary orbit is as large as 0.1 s. This delay variation actually measures the difference between periastron and apastron for a given Keplerian orbit. Thus it is significant for an eccentric orbit and can be measured by the timing difference between the primary and secondary transits for a long-period transit planet.

Without considering proper motion effects, EXOFAST+ introduces subsecond timing bias for τ Ceti and α Centauri A. This bias increases with the time difference between the reference epoch of the astrometry catalog and the mean epoch of the data. On the other hand, the decoupling approach adopted by EXOFAST+ and GREM would introduce 0.02 s bias in their timing model for α Centauri. Because TEMPO2 does not consider the third-order Roemer delay, there would be timing biases of 200 and 900 ns for τ Ceti and α Centauri for one decade, respectively. Because the third-order Roemer delay is determined by the time difference between simulated epochs and the reference epoch, the corresponding 200 ns timing bias for the simulated epochs starting from the *Gaia* reference epoch for τ Ceti (shown in Table 1) is much higher than that for earlier epochs shown in the right panel of Figure 7.

The atmospheric effects contribute a few arcminute position offset and are not modeled by GREM, which is aimed at space-based astrometry. The second-most significant astrometric

[11] EXOFAST+ represents a combination of the timing routines such as utc2bjd.pro developed by E10, EXOFAST developed by Eastman et al. (2013), and zbarycorr.pro developed by Wright & Eastman (2014). The Roemer delay in TS applies to EXOFAST, the radial velocity functionalities apply to zbarycorr.pro, and the other timing functionalities apply to utc2bjd.pro.

[12] Because we do not have access to the software, information about the functions implemented comes from Klioner & Kopeikin (1992) and Klioner (2003).

Table 1
Comparison of Various Packages and Amplitudes of High-order Classical and Relativistic Effects in Timing, Astrometry, and Radial Velocity

Model	Function	Equations	Unit	τ Ceti	α Centauri A	XO-3 b	PEXO	TEMPO2[a]	EXOFAST+	GREM
Timing	Second-order Roemer delay in SS	(32)	s	3×10^{-4}	5×10^{-4}	4×10^{-6}	✓	✓	××	✓
Timing	Third-order Roemer delay in SS	(8)	s	6×10^{-5}	9×10^{-7}	3×10^{-12}	✓	×	×	×
Timing	Einstein delay in SS	(30)	s	20	20	20	✓	✓	✓	✓
Timing	Shapiro delay due to the Sun	(34)	s	3×10^{-5}	2×10^{-5}	2×10^{-5}	✓	✓	✓	✓
Timing	Shapiro delay due to SS planets	(34)	s	4×10^{-8}	2×10^{-8}	3×10^{-8}	✓	××	×	×
Timing	Proper motion of TS	(32)	s	0.2	0.6	1×10^{-4}	✓	✓	×	✓
Timing	Roemer delay in TS	(39)	s	0	3×10^{3}	40	✓	✓	✓	✓
Timing	Einstein delay in TS	(40)	s	0	0.01	0.01	✓	✓	×	×
Timing	Shapiro delay in TS	(41)	s	0	4×10^{-6}	2×10^{-7}	✓	✓	×	×
Timing	Atmospheric effects	(27)	s	8×10^{-8}	3×10^{-8}	3×10^{-8}	✓	✓	×	×
Timing	Trend decoupling effects	(79)	s	0	0.02	4×10^{-3}	✓	✓	×	×
Timing	Period decoupling effects	(80)	s	0	0.02	5×10^{-7}	✓	✓	×	×
Astrometry	Second-order stellar aberration	(42)	as	6×10^{-4}	7×10^{-4}	7×10^{-6}	✓	×	×	✓
Astrometry	Third-order stellar aberration	(42)	as	2×10^{-7}	1×10^{-7}	1×10^{-7}	✓	×	×	✓
Astrometry	Lensing by the Sun	(50)	as	0.02	0.009	0.01	✓	×	×	✓
Astrometry	Lensing by SS planets	(50)	as	6×10^{-4}	2×10^{-4}	9×10^{-4}	✓	×	×	✓
Astrometry	Gravitational lensing in TS	(49)	as	0	3×10^{-9}	1×10^{-9}	✓	×	×	×
Astrometry	Second-order geometric effects	(8)	as	0.2	4	2×10^{-3}	✓	×	×	✓
Astrometry	Third-order geometric effects	(8)	as	2×10^{-6}	3×10^{-5}	2×10^{-14}	✓	×	×	×
Astrometry	Atmospheric effects	(47)	as	4×10^{3}	1×10^{3}	3×10^{3}	✓	×	×	×
Astrometry	Trend decoupling effects	(81)	as	0	9	2	✓	×	×	✓
Astrometry	Period decoupling effects	(82)	as	0	0.7	5×10^{-3}	✓	×	×	✓
Radial velocity	Relativistic effects in the SS	(58)	$m\,s^{-1}$	0.2	0.2	0.2	✓	⋯	✓	×
Radial velocity	Lensing by the Sun	(64)	$m\,s^{-1}$	2×10^{-3}	1×10^{-3}	1×10^{-3}	✓	⋯	✓	×
Radial velocity	Lensing by SS planets	(64)	$m\,s^{-1}$	5×10^{-6}	2×10^{-6}	2×10^{-6}	✓	⋯	✓	×
Radial velocity	Special relativity in TS	(57)	$m\,s^{-1}$	0	0.2	40	✓	⋯	×	×
Radial velocity	General relativity in TS	(55)	$m\,s^{-1}$	0	0.04	50	✓	⋯	×	×
Radial velocity	Lensing Doppler shift in TS	(66)	$m\,s^{-1}$	0	2×10^{-5}	2	✓	⋯	×	×
Radial velocity	Second-order geometric effects	(8)	$m\,s^{-1}$	0.07	0.9	8×10^{-3}	✓	⋯	✓	×
Radial velocity	Third-order geometric effects	(8)	$m\,s^{-1}$	6×10^{-7}	1×10^{-5}	2×10^{-14}	✓	⋯	×	×
Radial velocity	Atmospheric effects	(68)	$m\,s^{-1}$	8×10^{-3}	3×10^{-3}	4×10^{-3}	✓	⋯	×	×
Radial velocity	Trend decoupling effects	(76)	$m\,s^{-1}$	0	2	0.4	✓	⋯	×	×
Radial velocity	Period decoupling effects	(78)	$m\,s^{-1}$	0	2	5×10^{-5}	✓	⋯	×	×

Notes. The amplitudes are determined based on simulations over 10 years starting from the *Gaia* DR2 epoch. The solar system is denoted by SS while the target system is denoted by TS. We do not show constant effects such as the frame transformation between TSB and SSB. Because TEMPO2 is not optimal and is not aimed at radial velocity modeling, but in principle might offer the feature, we assign a dash mark to each radial velocity effect for TEMPO2. Because the wet component of tropospheric delay is not well modeled, we follow TEMPO2 to only model the hydrostatic component. The delay values are for elevation angle larger than 10° and thus are representative for most astronomical observations. Like TEMPO2, PEXO only models the well-understood components such as hydrostatic delay in the troposphere in these effects and models the other components as fittable parameters. The trend decoupling bias is calculated for a 10 year time span, while the period decoupling bias is for an orbital period of a given target system. The decoupling effects are recorded as a function of a package if all motions are modeled simultaneously to avoid decoupling bias, and the decoupling effects can be separated as a data product (or "barycentric correction"). If a function is included in a package, a tick is assigned. Otherwise, a cross is assigned. If there is a coding error for a function, we use two crosses to mark it.

[a] TEMPO2 is not designed primarily for radial velocity modeling, although the pulse frequency variation can be converted into Doppler shift.

effect is the stellar aberration. Because the first-order aberration is considered in most packages, we only show the second- and third-order aberration values in Table 1. The second-order aberration contributes at most 1 mas position offset and is not sensitive to stellar distance. Thus it is important for milliarcsecond-precision astrometry for all stars. Another significant effect is gravitational lensing by the Sun, which could contribute more than 10 mas position offset. The Earth

lensing dominates the planetary lensing effects and contributes a submilliarcsecond position offset. The third-order geometric effect contributes to a 30 μas astrometric bias for α Centauri A and is not included in GREM. Such an effect could be significant for some nearby binary systems and needs to be properly modeled if microarcsecond precision is required. The decoupling effect contributes a few arcsecond offset.

For the comparison of radial velocity models, the total decoupling bias is about 4 m s^{-1} for α Centauri over one decade and thus significantly higher than potential signals in the radial velocity data (Zhao et al. 2018). The time-varying special relativity effect in the α Centauri system is as much as 0.3 m s^{-1} and is not included in current radial velocity packages. The relativistic effects are even more significant in nearly edge-on systems such as XO-3. In such cases, even the lensing Doppler effect in the target system contributes up to 2 m s^{-1} and is measurable with current radial velocity instruments.

It is evident in Table 1 that no current packages are able to precisely model different types of data consistently. In contrast, PEXO stands out as a package for modeling multiple types of data in a precise and consistent fashion. This makes it a suitable package for synthesizing data from high-precision ground-based or space-based facilities.

6. Conclusion

In this work, we introduce relativistic models of timing, astrometry, and radial velocity in the PEXO package, which is mainly aimed at data analysis for exoplanets as well as tests of GR. PEXO includes the general and special relativistic effects both in the solar system and in the target system. These relativistic effects lead to Einstein delays in timing, stellar aberration in astrometry, and gravitational Doppler shift in radial velocity. PEXO also models the gravitational lensing and high-order geometric effects in both systems. The lensing effects lead to the Shapiro delay in timing, light deflection in astrometry, and Doppler shift in radial velocity. Based on our comparison of PEXO with TEMPO2, PEXO is able to achieve a timing precision of $\sim$1 ns, an astrometry precision of $\sim$1 μas, and a radial velocity precision of $\sim$1 μm s^{-1}.

These figures are comfortably better than what were expected to be achieved by current facilities. To test the precision of PEXO, we compare it with TEMPO2 and the package developed by E10. The timing precision of PEXO is at least comparable with TEMPO2 at the level of a few nanoseconds. It is better than TEMPO2 for decade-long timing data for nearby targets due to its consideration of the third-order terms of Roemer delay. We find an error in the routine shapiro_delay.C of TEMPO2 that could induce tens of nanoseconds timing bias in the calculation of Shapiro delay. Considering the popularity of TEMPO2 and the potential for coding errors in complex packages, we strongly recommend the application of independent packages for important discoveries in pulsar timing and exoplanetology as well as in other astrophysical applications. We also compare the IDL routine utc2bjd.pro developed by E10 and its corresponding applet with TEMPO2. We find that the applet is able to provide a timing precision of a few milliseconds if ignoring the proper motion effects. However, we notice an error in the calculation of parallax delay in utc2bjd.pro, leading to a timing error of about 0.3 ms for τ Ceti. Although such a bug is not significant for current exoplanet science, it could become significant for high-precision applications. The corrected IDL version of E10 is able to model timing to a precision of a few microseconds if the propagation of TSB is provided externally. The errors in high-precision packages such as TEMPO2 and utc2bjd.pro demonstrate the utility of new packages in minimizing coding errors and their potential spread in other applications.

The numerical implementations of barycentric correction of radial velocity for PEXO and TEMPO2 differ a few μm s^{-1}. Considering the timing error in radial velocity data, PEXO is able to provide a practical radial velocity precision of 1 cm s^{-1}. The main limitation of radial velocity precision comes from the bias in the determination of the appropriate midpoint of an exposure caused by effects such as the atmospheric chromatic aberration. We do not compare PEXO with the known high-precision astrometry package GREM because it is not publicly available. Considering the consistency between astrometry and radial velocity modeling, we expect the astrometry precision to be microarcseconds.

We test various effects in transit timing by applying PEXO to XO-3 b and Kepler-210 c. The relativistic effects are not significant enough to be detectable in these two cases. High-cadence and long-term observations are needed to reliably detect relativistic precession in short-period and eccentric-transit systems where planet-induced precession is minimized. Follow-up work on how transit timing is sensitive to various relativistic effects is needed for the potential application of transit timing in the test of GR, as done in pulsar timing. The Einstein delay in the target system contributes to a 0.2 s timing variation for α Centauri over one decade but is not included in many previous packages such as EXOFAST and GREM. The Einstein delay in some high-eccentricity transit systems might be detectable in the timing difference between the primary and secondary transits. We further investigate the feasibility of using PEXO for relativity tests in binaries. The gravitational redshift variation caused by the companion of the target star is as large as a few m s^{-1} for 52 binaries with orbital periods less than 10 yr. Such tests are able to examine GR and MOND theories in a new regime of stellar mass and weak gravitational field.

Using α Centauri as an example, we assess relativistic effects in the modeling of astrometry. We find that the lensing effect in the solar system contributes to 9 mas position variation, while the lensing effect in α Centauri only contributes to 0.003 μas position variation over one decade. The barycentric motion of the binary, the stellar aberration due to the Earth's motion, and atmospheric refraction are the major effects changing the observed direction of photons. For ground-based astrometric observations, the atmospheric modeling uncertainty limits the absolute positional precision to 1 arcsec and the relative positional precision to tens of microarcseconds. For space-based observations, an astrometry precision of microarcseconds requires a telescope ephemeris with 1 cm s^{-1} velocity precision. An alternative approach is to determine the Earth's motion a posteriori through a combined fit to the data. The third-order geometric effect contributes to a few microarcsecond position bias and is not included in the GREM package, which is used by *Gaia* for relativistic astrometric solutions (Lindegren et al. 2018).

We assess various effects in the radial velocity model using the example of α Centauri A. The general and special relativistic effects in the α Centauri system affect the radial velocity of α Centauri A by 0.04 and 0.2 m s^{-1} over one

decade, respectively. Although these effects are essential for sub-m s^{-1} radial velocity modeling of binary systems, they are not accounted for in radial velocity packages. The special relativity effect due to α Centauri B changes the radial velocity by nearly 1 m s^{-1} over one orbital period. The binary motion of the target star would change the viewing perspective, leading to a change in the projection of various motions onto the radial velocity direction. Furthermore, errors in astrometry data would lead to considerable radial velocity variation for nearby stars. We find that decoupling could introduce $\sim$0.1 m s^{-1} bias in one decade of radial velocity observations of a nearby star ($<$10 pc) with hot or cold Jupiters and could introduce $\sim$1 m s^{-1} bias over one year for nearby stars with stellar-mass companions. Therefore, a barycentric correction of the measured radial velocity is not appropriate to achieve 1 cm s^{-1}. We suggest a combined modeling of stellar reflex motion, stellar proper motion, and the Earth's motion for high-precision radial velocity modeling.

The $\sim$1 ns timing precision of PEXO and TEMPO2 can be achieved if the uncertainty in the ephemeris of solar system bodies is less than 1 m and the effect of interstellar scattering is well understood (E06). On the other hand, the radial velocity precision of 1 μm is the software precision that is achievable only if we could model the observational effects to a high precision. For example, to achieve a precision of 1 mm s^{-1} in radial velocity modeling, we need to determine the midpoint of exposures in spectroscopic observations to a precision of a few milliseconds by properly modeling the atmospheric chromatic aberration of incoming photons. For future space-based spectrographs such as EarthFinder (Plavchan et al. 2018), the exposure time might be better determined and telluric effects would disappear, enabling $<$1 cm s^{-1} radial velocity precision if combined with PEXO's precise modeling of astrophysical effects. PEXO's precision can be further improved by the appropriate modeling of the Galactic acceleration of stars and the dispersion of photons in the interplanetary and interstellar medium. The extra packages envisaged for PEXO are (1) the Galactic acceleration of stars and the corresponding secular aberration as well as cosmological effects (e.g., Klioner 2003 and Lindegren & Dravins 2003) and (2) the inclusion of gravitational wave effects to provide an independent package for the detection of gravitational waves using pulsar timing arrays such as NANOGrav (e.g., Arzoumanian et al. 2018).

Based on our investigation of various relativistic effects and comparison of various packages, we summarize the main results of this paper and give relevant recommendations as follows:

1. By accounting for relativistic and high-order geometric effects, PEXO is able to model timing to a precision of 1 ns, astrometry to 1 μas, and radial velocity to 1 μm s^{-1}. PEXO is able to model multiple types of data precisely and consistently.
2. Decoupling of the target system and the solar system introduces considerable bias in the modeling of timing, astrometry, and radial velocity. For stars with stellar-mass companions and for nearby stars with Jupiter-mass companions, we recommend a combined modeling of binary motion, binary barycentric motion, and telescope ephemeris. An alternative, efficient approach is to model the decoupling trend bias using astrometric offsets and fit all motions to the data corrected for barycentric effects.
3. A detectable relativistic effect in extrasolar systems is the gravitational redshift of the light from a target star caused by its companion star. This test is feasible for a few binaries with long-term and high-precision radial velocity data ($\sim$1 m s^{-1} uncertainty), such as α Centauri A and B.
4. Atmospheric effects limit absolute astrometry to a precision of 1 arcsec and relative astrometry to a precision of tens of microarcseconds. Such precisions are only achievable if various atmospheric parameters are well measured at the observation site and the refraction effects are correctly modeled through reliable packages. To avoid high model uncertainty, we recommend an elevation angle of at least 30° for direct imaging of planets (see Section 5.2).
5. Second-order stellar aberration is needed to model space-based astrometric observations correctly. The third-order geometric effects become significant for decade-long observations of nearby stars. Because GREM is the core package used for *Gaia*'s astrometry solution (Lindegren et al. 2018), we recommend a more comprehensive analysis of astrometric epoch data for nearby stars to reveal potential planetary signals.
6. The consideration of relativistic effects in the target system is the missing piece in previous exoplanet packages. The Einstein delay and gravitational Doppler shift are significant in some binary systems and are detectable with current technology.
7. The coding error in the calculation of planetary Shapiro delay would bias TEMPO2 timing modeling by at least tens of nanoseconds over one decade. The bug in the calculation of parallax delay in utc2bjd.pro would bias its timing precision by $\sim$1 ms for nearby stars.
8. PEXO is tested by comparison with TEMPO2 and by recovering previous fitting results for the astrometric and radial velocity data for α Centauri.

In summary, PEXO provides a high-precision combined model for timing, radial velocity, and astrometry data. PEXO is versatile enough to take binary motions into account and precise enough to consider high-order classical and relativistic effects. By applying PEXO to the analysis of high-precision data provided by the state-of-the-art facilities such as *TESS*, ESPRESSO, and *Gaia*, we expect to have the ability to make a reliable detection of an Earth twin as well as a test of GR in extrasolar systems in the near future.

We are indebted to the anonymous referee of this paper for their inspiring and insightful comments that led to very substantial improvements in the content and clarity of this manuscript and PEXO. M.L. is supported by a University of Hertfordshire PhD studentship. F.F. and H.J. acknowledge support from the UK Science and Technology Facilities Council [ST/M001008/1]. This work has made use of data from the European Space Agency (ESA) mission *Gaia* (https://www.cosmos.esa.int/gaia), processed by the *Gaia* Data Processing and Analysis Consortium (DPAC, https://www.cosmos.esa.int/web/gaia/dpac/consortium). Funding for the DPAC has been provided by national institutions, in particular the institutions participating in the *Gaia* Multilateral Agreement. We adapt various SOFA routines (http://www.iausofa.org/) to R functions in PEXO.

Appendix A
Conventions in Binary Studies

The angular parameters for a binary orbit depend on the coordinate system where it is defined. We introduce three coordinate systems and corresponding orbital parameters in order to clarify the previous conventions and to assist the community in using data consistently.

Before defining the coordinate system, we need to be clear what we mean by rotation matrix, which is essential to transforming between different coordinate systems. We define a rotation matrix R as an operation to rotate vector $\boldsymbol{r}_a$ to $\boldsymbol{r}_b$. For example, in a 2D Cartesian system, we use the following matrix to rotate $\boldsymbol{r}_a$ counterclockwise by θ to get $\boldsymbol{r}_b$:

$$\boldsymbol{r_b} \equiv \begin{bmatrix} x_b \\ y_b \end{bmatrix} = \begin{bmatrix} \cos\theta & -\sin\theta \\ \sin\theta & \cos\theta \end{bmatrix} \begin{bmatrix} x_a \\ y_a \end{bmatrix}. \tag{96}$$

For a 3D rotation matrix in a Cartesian coordinate system, we define a counterclockwise rotation around the x axis by θ as

$$R_x(\theta) = \begin{bmatrix} 1 & 0 & 0 \\ 0 & \cos\theta & -\sin\theta \\ 0 & \sin\theta & \cos\theta \end{bmatrix}, \tag{97}$$

a counterclockwise rotation around the y axis by θ as

$$R_y(\theta) = \begin{bmatrix} \cos\theta & 0 & \sin\theta \\ 0 & 1 & 0 \\ -\sin\theta & 0 & \cos\theta \end{bmatrix}, \tag{98}$$

and a counterclockwise rotation around the z axis by θ as

$$R_z(\theta) = \begin{bmatrix} \cos\theta & -\sin\theta & 0 \\ \sin\theta & \cos\theta & 0 \\ 0 & 0 & 1 \end{bmatrix}. \tag{99}$$

For example, if the rotation sequence is to rotate vector $\boldsymbol{r}_a$ around the x axis by θ_1, y axis by θ_2, and z axis by θ_3, the new vector $\boldsymbol{r}_b$ should be

$$\boldsymbol{r_b} = R_x(\theta_1)R_y(\theta_2)R_z(\theta_3)\boldsymbol{r_a}. \tag{100}$$

If $\boldsymbol{r}_a$ is one of the axes of a coordinate system, the above operation would lead to a new coordinate system defined by $\boldsymbol{r}_b$. In other words, two coordinate systems are related to each other by

$$\begin{bmatrix} x' & y' & z' \end{bmatrix} \begin{bmatrix} \boldsymbol{e}'_x \\ \boldsymbol{e}'_y \\ \boldsymbol{e}'_z \end{bmatrix} = \begin{bmatrix} x & y & z \end{bmatrix} \begin{bmatrix} \boldsymbol{e}_x \\ \boldsymbol{e}_y \\ \boldsymbol{e}_z \end{bmatrix}, \tag{101}$$

where $\boldsymbol{e}'_x$, $\boldsymbol{e}'_y$, and $\boldsymbol{e}'_z$ are axes of the new coordinate system, $\boldsymbol{e}_x$, $\boldsymbol{e}_y$, and $\boldsymbol{e}_z$ are axes of the old coordinate system, and $[x', y', z']$ and $[x, y, z]$ are respectively the new and old coordinates of a vector. If the new coordinate system is transformed from the old one by rotation matrix R, which is orthogonal, the new coordinates would be

$$\begin{bmatrix} x' \\ y' \\ z' \end{bmatrix} = R^{\mathrm{T}} \begin{bmatrix} x \\ y \\ z \end{bmatrix}. \tag{102}$$

For the rotation operations in Equation (100), the coordinate transformation would be

$$\begin{bmatrix} x' \\ y' \\ z' \end{bmatrix} = R_z(-\theta_3)R_y(-\theta_2)R_x(-\theta_1) \begin{bmatrix} x \\ y \\ z \end{bmatrix}. \tag{103}$$

We will apply the definition and conclusion in the above analysis to the following subsections. We will introduce three conventions and label the corresponding coordinates by subscripts 1, 2, and 3. In the following conventions, we model the motion of the target object with respect to the binary barycenter. It is also known as stellar reflex motion if the star is the target.

A.1. Definition of Orbital Elements

Before introducing coordinate systems, we define the orbital elements independent of the chosen coordinate system. By doing this, we emphasize that conventions for orbital elements and coordinate systems are independent. To distinguish these two conventions, we use "definition" to name the former and "convention" to name the latter. The orbit of the target is in the "orbit plane," while the plane perpendicular to $\boldsymbol{r}_{\mathrm{SB}}$ is called the "sky plane." To focus on the study of stellar reflex motion, we assume that the observer is located at the SSB and the proper motion of TSB is zero. According to Equation (8), the offsets are $\xi \equiv \Delta\alpha^* \approx \boldsymbol{p}_b \cdot \boldsymbol{r}_{\mathrm{BT}}(t)\tilde{\omega}^b/A$ and $\eta \equiv \Delta\delta \approx \boldsymbol{q}_b \cdot \boldsymbol{r}_{\mathrm{BT}}(t)\tilde{\omega}^b/A$. This assumption is only used for a convenient definition of orbital elements and is not used in PEXO modeling. Because the semimajor axis and eccentricity do not depend on the viewing geometry, we focus on the definition of angular orbital elements.

The inclination I is defined as the angle between the target-to-observer direction (i.e., $-\boldsymbol{u}_b$) and the angular momentum. Thus, for an orbit with $0^\circ < I < 90^\circ$, the motion of the target with respect to the binary barycenter is counterclockwise if viewed by the observer. The line of nodes is at the intersection between the orbit plane and the sky plane. The ascending node is the node at which the target crosses the sky plane and moves away from the observer. The longitude of ascending node Ω is the counterclockwise angle in the sky plane from the north to the ascending node viewed from the observer. For the motion of the target with respect to the system barycenter or to the companion, we use the argument of periastron ω_{T}, which is the angle in the orbit plane from the ascending node to the periastron along the motion of the target. For the orbit of a companion with respect to the barycenter or to the target, the argument of periastron is $\omega_{\mathrm{C}} = \omega_{\mathrm{T}} + \pi$. We will use the barycentric motion of the target as an example for the following introduction and discussions.

It is important to note that astrometry data alone cannot distinguish between the ascending and descending nodes because we do not know whether the star is moving away from or toward the observer. Thus we recommend restricting the range of ω and Ω to be $[0, \pi]$ for astrometry-only analyses. This restriction should not be used for combined analyses of astrometry and radial velocity data. We also recommend reporting $\omega + \pi$ and $\Omega + \pi$ as an alternative solution. These are practical suggestions for fitting that do not change the definitions of the ascending node. If only one set of ω and Ω values is reported based on an astrometry-only analysis, $\omega + \pi$ and $\Omega + \pi$ should be considered as an alternative solution

during a combined analysis of astrometry and radial velocity data.

The orbital elements are illustrated in Figure 2. In principle, coordinate systems are not needed because the orbital elements are defined independently of the coordinate system. We can transform the target motion from the orbit-plane frame to the sky-plane frame, which is formed by the north (increase of decl.), the east (increase of R.A.), and the direction from the target to the observer. However, for the convenience of formulization, we can randomly assign these three axes or their opposite directions as X, Y, and Z axes to form a left-handed or right-handed coordinate system for the sky-plane frame. We will introduce three of them as follows.

A.2. Convention I: Right-handed Coordinate System

We use a right-handed convention where the $+X$ direction is along the north (or increasing decl.), the $+Y$ direction is along the east (or increasing R.A.), and the $+Z$ axis is from the target to the observer (or decreasing distance). In the orbit plane, the $+x$ axis is the direction of periastron, the $+z$ axis is along the direction of orbital angular momentum of a binary, and the $+y$ axis is in the orbit plane and is chosen such that x, y, and z axes form a right-handed Cartesian coordinate system. The rotation matrix transforming the orbital-plane frame to the sky-plane frame is $R_z(-\omega)R_x(I)R_z(-\Omega)$. Thus the coordinate transformation matrix[13] would be its inverse or transpose, which is $R_z(\Omega)R_x(-I)R_z(\omega)$.

The orbital-plane coordinates are transformed into the sky-plane coordinates following

$$\begin{bmatrix} X_1 \\ Y_1 \\ Z_1 \end{bmatrix} = R_z(\Omega)R_x(-I)R_z(\omega)\begin{bmatrix} x \\ y \\ 0 \end{bmatrix}. \tag{104}$$

The expansion of the above rotation matrices leads to

$$\begin{bmatrix} X_1 \\ Y_1 \\ Z_1 \end{bmatrix} = \begin{bmatrix} \cos\Omega\cos\omega_T - \sin\Omega\sin\omega_T\cos I & -\cos\Omega\sin\omega_T - \sin\Omega\cos\omega_T\cos I & -\sin\Omega\sin I \\ \sin\Omega\cos\omega_T + \cos\Omega\sin\omega_T\cos I & -\sin\Omega\sin\omega_T + \cos\Omega\cos\omega_T\cos I & \cos\Omega\sin I \\ -\sin\omega_T\sin I & -\cos\omega_T\sin I & \cos I \end{bmatrix}\begin{bmatrix} x \\ y \\ 0 \end{bmatrix}. \tag{105}$$

Ignoring the scaling between the orbital ellipse in the orbital plane and that in the sky plane, the elements of the matrix in the above equation are also known as Thiele–Innes constants (Thiele 1883):

$$\begin{aligned} A' &= \cos\Omega\cos\omega_T - \sin\Omega\sin\omega_T\cos I, \\ B' &= \sin\Omega\cos\omega_T + \cos\Omega\sin\omega_T\cos I, \\ F' &= -\cos\Omega\sin\omega_T - \sin\Omega\cos\omega_T\cos I, \\ G' &= -\sin\Omega\sin\omega_T + \cos\Omega\cos\omega_T\cos I. \end{aligned} \tag{106}$$

Then Equation (105) becomes

$$\begin{bmatrix} X_1 \\ Y_1 \\ Z_1 \end{bmatrix} = \begin{bmatrix} A' & F' & -\sin\Omega\sin I \\ B' & G' & \cos\Omega\sin I \\ -\sin\omega_T\sin I & -\cos\omega_T\sin I & \cos I \end{bmatrix}\begin{bmatrix} x \\ y \\ 0 \end{bmatrix}. \tag{107}$$

[13] The rotation matrices defined in this work are the transposes of the corresponding ones defined in Catanzarite (2010).

A.3. Convention II: Left-handed Coordinate System

In the study of binaries, another convention closely related to convention I is also frequently used. In this convention, the $+Z$ axis is along the increasing distance, leading to a left-handed Cartesian coordinate system. To keep the convention that a counterclockwise orbit on the sky plane viewed from the observer corresponds to an inclination of 0°–90°, we keep the definition of inclination as well as other orbital elements in convention I. Thus the new coordinates in this convention are related to the coordinates in convention I by

$$\begin{aligned} \begin{bmatrix} X_2 \\ Y_2 \\ Z_2 \end{bmatrix} &= \begin{bmatrix} X_1 \\ Y_1 \\ -Z_1 \end{bmatrix} \\ &= \begin{bmatrix} A' & F' & -\sin\Omega\sin I \\ B' & G' & \cos\Omega\sin I \\ \sin\omega_T\sin I & \cos\omega_T\sin I & -\cos I \end{bmatrix}\begin{bmatrix} x \\ y \\ 0 \end{bmatrix}. \end{aligned} \tag{108}$$

A.4. Convention III: Astrometric and Precession-compatible Convention

In this study, we used the right-handed coordinate system formed by the triad $[\boldsymbol{p}, \boldsymbol{q}, \boldsymbol{u}]$. Here, $\boldsymbol{p}$ is in the direction of increasing R.A., $\boldsymbol{q}$ is in the direction of increasing decl., and $\boldsymbol{u}$ is in the direction of increasing distance. Thus, $\boldsymbol{p}$ and $\boldsymbol{q}$ axes in this convention correspond to the Y and X axes in convention II, respectively. Because this $[\boldsymbol{p}, \boldsymbol{q}, \boldsymbol{u}]$ triad is used in the astrometry models of *Hipparcos* and *Gaia* (ESA 1997; Lindegren et al. 2012), we call the corresponding convention of binary motion the "astrometric convention." By using the same definition of orbital elements to avoid unnecessary confusion, we get the new coordinates in this convention by

$$\begin{bmatrix} Y_3 \\ X_3 \\ Z_3 \end{bmatrix} = \begin{bmatrix} X_2 \\ Y_2 \\ Z_2 \end{bmatrix}. \tag{109}$$

From the above transformation, we derive the position of the target relative to TSB as

$$\boldsymbol{r}_{BT} = \begin{bmatrix} X_3 \\ Y_3 \\ Z_3 \end{bmatrix}. \tag{110}$$

This convention is also used in TEMPO2 (E06), although they set the $+x$ direction in the orbital plane as the ascending node considering the precession of periastron. We call this convention the "precession-compatible convention" due to its consideration of precession of periastron. Thus the rotation matrix in Equation (21) is the same as the one in Equation (108) and in Equation (54) of E06 if setting $\omega = 0$ and swapping the first and second rows.

We emphasize that the conventions for coordinate systems are used for transformation from the orbit-plane to the sky-plane frames. Like the choice of TDB and TCB time standards, the choice of coordinate system does not matter as long as the stellar reflex motion is correctly modeled in offset coordinates (i.e., $\Delta\alpha*$ and $\Delta\delta$). Considering the variety of conventions used in binary studies, we recommend a consistent definition and introduction of conventions including orbital elements and coordinate systems in the studies of binaries and exoplanets.

A.5. Comments on Previous Conventions

The conventions for binaries and exoplanets are not always clearly presented and consistently used in the literature. To help the community use conventions consistently, we comment on some of the previous conventions that are not consistently defined or presented.

Although we have used the definition of orbital elements in Catanzarite (2010) for all three conventions of coordinate systems, Catanzarite (2010) did not present his convention consistently in his Figure 1. He used an image from Wikipedia (https://en.wikipedia.org/wiki/Longitude_of_the_ascending_node#/media/File:Orbit1.svg) to illustrate his convention, although this image is more suitable for studies of the solar system. In his Figure 1, the observer views the planetary system from above the reference plane. The target moves toward the observer after crossing the ascending node. Thus the ascending node should be the descending node in the figure according to the definition used by Catanzarite (2010). Although the ascending node would be correct if the observer views the system from the south (or $-Z$ direction), the inclination would be incorrect because the orbit would be retrograde, and thus the inclination should be larger than 90° (i.e., 180° minus the inclination presented in Figure 1).

In solar system studies, the ascending node is a point in the orbit and sky planes where an object moves from the south to the north (or $+Z$ direction) of the reference plane. Because the observer is absent in the definition, we call this definition "observer-independent ascending node." Nevertheless, the ascending node defined in binary studies is the point both in the orbit plane and in the sky plane where the target moves away from the observer. Because it depends on the direction of the observer, we call this definition the "observer-dependent ascending node." The observer-dependent ascending node is consistent with the convention that the radial velocity of a target is positive if it is moving away from us. Therefore, the observer-dependent ascending node is correctly defined by Catanzarite (2010) but is presented as the observer-independent ascending node. The differences between observer-dependent and observer-independent ascending nodes are intrinsic and do not depend on the choice of coordinate systems.

Similarly, Figures 4 and 7 in Murray & Correia (2010) and Figure 31 in Binnendijk (1960) show that they use the observer-independent ascending node to study binaries and exoplanets. Although the ascending node is not consistently defined in Murray & Correia (2010) and Binnendijk (1960), they transform the binary motion from the orbit plane to the sky plane (or reference plane) correctly. Their use of the observer-independent ascending node would lead to a sign flip in the value of radial velocity (i.e., $-Z_1$; see Equation (105)). This sign flip would be absorbed through the fit of ω_T to the radial velocity data, leading to a value of ω_T inconsistent with their definition of ascending node. In particular, it would become problematic for astrometry modeling where the proper motion of the barycenter and the stellar reflex motion need to be combined.

Compared with previous illustrations of binary motion, Figure 2 consistently visualizes the observer-dependent ascending node. The star is moving away from the observer after crossing the ascending node. The longitude of the ascending node Ω is measured counterclockwise from the north to the ascending node from the observer's perspective. The inclination is the angle between the angular momentum and the $-\boldsymbol{u}_b$ direction so that the orbit is prograde for $0° < I < 90°$ and retrograde for $I > 90°$ viewed by the observer. The requirement of consistency makes Figure 2 different from the equivalent ones frequently used in the literature.

Appendix B
Acronyms and Symbols

We show the meaning of the acronyms and symbols, as well as the section where they first appear, in Table 2.

Table 2
Meanings Of Acronyms and the Sections Where They First Appear

Acronym or Symbol	Meaning	Sections
BCRS	Barycentric Celestial Reference System	2
BIPM	International Bureau of Weights and Measures	3.2.2
BIPMXY	BIPM realization of TT in year 19XY if $XY > 20$ or 20XY if $XY < 20$	3.2.2
BJD	Barycentric Julian date	3.2.2
C	Companion in the target system	2
DD	Post-Newtonian binary model proposed by Damour & Deruelle (1986)	3.1
DDGR	General relativity binary model proposed by Damour & Deruelle (1986)	3.1
GR	General relativity	1
JD	Julian date	3.2.2
MJD	Modified Julian date	5.3
NCP	North Celestial Pole	2.3
PEXO	Precision Exoplanetology	1
PPN	Parameterized Post-Newtonian formalism	3.3.1
O	Observatory site	2.1
RV	Radial velocity	1
SS	Solar system	2.1
SSB or S	Solar system barycenter	2
T	Target star	2
TAI	International Atomic Time	3.2.2
TCB	Barycentric Coordinate Time	3.2.2
TCG	Geocentric Coordinate Time	3.2.2
TDB	Barycentric Dynamical Time	3.2.2
TDF	Transit Duration Fraction	5.1
TDV	Transit Duration Variation	5.1
TS	Target System	2.1
TSB or B	Target System Barycenter	2.1
TT	Terrestrial Time or proper time at the geoid	3.2.2
TTV	Transit Timing Variation	5.1
UTC	Coordinated Universal Time	3.2.2
A	1 au	2.1
a	Semimajor axis of the target star with respect to the companion	2.3
a_C	Semimajor axis of the barycentric orbit of the companion	2.3

Table 2
(Continued)

Acronym or Symbol	Meaning	Sections
a_r	Counterpart of $a_{\rm T}$ in the DD model	
$a_{\rm T}$	Semimajor axis of the barycentric orbit of the target star	2.3
c	Speed of light	3.1
$\dot{e}$	Time derivative e in DD model	3.1
e_0	Eccentricity at a reference time in post-Newtonian models	2.3
E	Eccentric anomaly of the barycentric orbit of the target star	2.3
f	True anomaly of the barycentric orbit of the target star	2.3
G	Gravitational constant	3.1
g	Timing model parameter in the DD model	3.1
$h_{\rm O}$	Altitude of the observer	3.2.1
I	Orbital inclination of the target star with respect to the TSB	2.3
$\boldsymbol{l}_e$	Light ray direction at the emission time	3.3.1
$\boldsymbol{l}_i$	Incident light ray before entering atmosphere	3.3.3
$\boldsymbol{l}_l$	Light ray direction after lensing by the companion	3.3.1
$\boldsymbol{l}_o$	Light ray direction at the observation time	3.3.1
L_B	Scaling factor for the transformation between TCB and TDB	3.2.2
L_G	Scaling factor for the transformation between TT and TCG	3.2.2
$\mathcal{L}$	Light ray path in the atmosphere	3.2.1
$m_{\rm C}$	Mass of the companion	2.3
m_h	Mapping function for hydrostatic delay	2.3
$m_{\rm T}$	Mass of the target star	2.3
m_w	Mapping function for wet delay	2.3
$m_\odot$	Mass of the Sun	2.3
n	Mean motion of the target binary orbit	2.3
$n_{\rm O}$	Refraction index at the telescope	3.3.2
$N_{\rm wet}$	Refractivity of wet component	3.2.1
$N_{\rm hydro}$	Refractivity of hydrostatic component	3.2.1
P	Orbital period of the target system	3.6
P_0	Orbital period at a reference time in post-Newtonian models	2.3
$\dot{P}$	Time derivative of P in the DD model	2.3
$p_{\rm O}$	Air pressure at the observation site	3.2.1
$\boldsymbol{p}_b$	Unit vector in the directions of increasing R.A. α at the reference time t_0	2.1
$\boldsymbol{q}_b$	Unit vector in the directions of increasing decl. δ at the reference time t_0	2.1
r_s	Range parameter of Shapiro delay	2.1
$r_s^{\rm GR}$	Range parameter of Shapiro delay assuming general relativity	2.1
$\boldsymbol{r}_{\rm BT}$	Vector from B to T	2.1
$\boldsymbol{r}_{\rm CT}$	Vector from C to T	3.4.2
$\boldsymbol{r}_{\rm OB}$	Vector from O to B	2.1
$\boldsymbol{r}_{\rm OC}$	Vector from O to C	3.4.2
$\boldsymbol{r}_{\rm orb}$	Barycentric position of the target in the orbital plane	2.3
$\boldsymbol{r}_{\rm OS}$	Vector from O to S	2.1
$\boldsymbol{r}_{\rm OT}$	Vector from O to T	2.1
$\boldsymbol{r}_{\rm SB}$	Vector from S to B	2.1
$\boldsymbol{r}_{\rm ST}$	Vector from S to T	3.2.2
$\boldsymbol{r}_\oplus$	Barycentric position of the geocenter	3.2.2
$\boldsymbol{R}$	$[\boldsymbol{r}_{\rm BT}(t) - \boldsymbol{r}_{\rm SO}(t)]\widehat{\omega}^b/A$	2.1
$\boldsymbol{\mathcal{R}}$	Refraction vector	2.1
$\boldsymbol{s}$	Position of observatory with respect to the geocenter	2.1

Table 2
(Continued)

Acronym or Symbol	Meaning	Sections
s_s	Shape parameter of Shapiro delay	2.1
$s_s^{\rm GR}$	Shape parameter of Shapiro delay assuming general relativity	2.1
t	Arbitrary coordinate time	2.1
t_0	Arbitrary reference coordinate time, $t_0 = t_{\rm pos}$ by default	2.1
$t_a^{\rm SSB}$	Light arrival time at SSB	2.1
$t_a^{\rm TSB}$	Light arrival time at TSB	2.1
t_e	Coordinate time of light emission	2.1
t_i	Arrival time of incident light ray without atmospheric refraction	3.4.2
$t_{\mathcal{G}}$	Vacuum light propagation time for straight light ray	3.2.1
$t_{\mathcal{L}}$	Vacuum light propagation time for deflected light ray	3.2.1
t_o	Coordinate time of light arrival at the observatory	2.1
$t_{\rm pos}$	Reference epoch when the position or astrometry of the target star is measured	3
T_0	Proper time of periastron in post-Newtonian models	2.3
T_c	Midtransit time	5.1
$T_\odot$	$Gm_\odot/c^3$; Half the light travel time across the solar Schwarzschild radius	2.3
U	Relativistic eccentric anomaly	2.3
$U_\oplus$	Gravitational potential of all solar system objects apart from the Earth at the observatory	3.2.2
$\boldsymbol{u}_b$	Unit vector from S to B at the reference time t_0	2.1
$\boldsymbol{u}_o$	Observed direction of arriving light ray	3.3.1
$\hat{\boldsymbol{u}}_o$	Model prediction of the observed direction of arriving light ray	3.3.1
$\boldsymbol{u}_{\rm OT}$	Unit vector from O to T	4.2
$\boldsymbol{u}_{\rm SB}$	Unit vector from S to B	3.2.2
$\boldsymbol{u}_{\rm ST}$	Unit vector from S to T	2.1
$\boldsymbol{u}_{\rm Z}$	Unit vector in the zenith direction	2.1
v_e	Escape velocity	3.4.1
$\boldsymbol{v}_{\rm BT}$	Velocity of T with respect to B	3.2.4
$\boldsymbol{v}_{\rm CT}$	Velocity of T with respect to C	3.4.2
$\boldsymbol{v}_{\rm OS}$	Velocity of S with respect to O	4.2
$\boldsymbol{v}_{\rm OT}$	Velocity of T with respect to O	4.2
$\bar{\boldsymbol{v}}_{\rm reflex}$	Average reflex motion of the target star	3.5
$\boldsymbol{v}_r^b$	$\boldsymbol{v}_{\rm OT}$ at the reference epoch t_0	2.1
$\boldsymbol{v}_r^{\rm obs}$	Observed absolute radial velocity	2.1
$\boldsymbol{v}_{\rm SB}$	Velocity of B with respect to S	4.2
$\boldsymbol{v}_{\rm ST}$	Velocity of T with respect to S	3.4.1
$\boldsymbol{v}_{\rm TC}$	Velocity of C with respect to T	5.1
$v_{\rm tot}$	Characteristic radial velocity of a star with respect to the observer	3.5
$v_\oplus$	Barycentric velocity of the geocenter	3.2.2
W_0	Gravitational and spin potential of the Earth at the geoid	3.2.2
x	x Coordinate in the orbital plane	2.3
y	y Coordinate in the orbital plane	2.3
x_a	$a\sin I/c$; Light travel time across the projected semimajor axis	3.1
$\dot{x}_a$	Time derivative of x_a in the DD model	2.3
Z_i	Zenith angle of incident light ray	3.3.2
Z_o	Observed zenith angle	3.3.2
$z_{\rm kS}$	Doppler shift due to kinematic effects in the solar system	3.4.1

Table 2
(Continued)

Acronym or Symbol	Meaning	Sections
$z_{\rm kT}$	Doppler shift due to kinematic effects in the target system	3.4.1
$z_{\rm lS}$	Doppler shift due to kinematic effects in the solar system	3.4.1
$z_{\rm lT}$	Doppler shift due to kinematic effects in the target system	3.4.1
$z_{\rm grS}$	Doppler shift due to general relativity effects in the solar system	3.4.1
$z_{\rm grT}$	Doppler shift due to general relativity effects in the target system	3.4.1
$z_{\rm srS}$	Doppler shift due to special relativity effects in the solar system	3.4.1
$z_{\rm srT}$	Doppler shift due to special relativity effects in the target system	3.4.1
$z_{\rm S}$	Doppler shift due to all effects in the solar system	3.4.1
$z_{\rm T}$	Doppler shift due to all effects in the target system	3.4.1
α^b	BCRS R.A. of the TSB at the reference time t_0	2.1
γ	One PPN parameter	3.3.1
$\phi_{\rm O}$	Latitude of the observer	3.2.1
$\Phi_{\rm T}$	Gravitational potential at the target star center	3.6
δ^b	BCRS decl. of the TSB at the reference time t_0	2.1
δt	Arbitrary time span	3.5
δT	Difference between the BIPM and TAI realizations of TT	3.2.2
$\delta v_r^{\rm grT}$	Radial velocity variation due to general relativity in TS	3.4.1
$\delta v_r^{\rm srT}$	Radial velocity variation due to special relativity in TS	3.4.1
$\delta v_r^{\rm trend}$	Trend decoupling bias in radial velocity	3.5
$\delta v_r^{\rm period}$	Periodic decoupling bias in radial velocity	3.5
$\delta \boldsymbol{u}$	Positional bias	3.5
$\delta u_{\rm trend}$	Trend decoupling bias in target position	3.5
$\delta u_{\rm period}$	Periodic decoupling bias in target position	3.5
$\delta\Delta^{\rm trend}$	Trend decoupling bias in timing	3.5
$\delta\Delta^{\rm period}$	Periodic decoupling bias in timing	3.5
$\delta z_{\rm grT}$	Doppler shift variation due to general relativity in TS	3.4.1
$\delta z_{\rm srT}$	Doppler shift variation due to special relativity in TS	3.4.1
$\delta\mu$	Proper motion bias caused by ignoring the target reflex motion	3.5
$\Delta\alpha*$	Offset in the R.A. direction	5.2
$\Delta\delta$	Offset in the decl. direction	5.2
$\Delta\xi$	ξ of the secondary with respect to the primary	2.1
$\Delta\eta$	η of the secondary 1 with respect to the primary	2.1
$\Delta\boldsymbol{r}$	$\boldsymbol{r}_{\rm BT2}(t) - \boldsymbol{r}_{\rm BT1}(t)$; Position of the secondary with respect to the primary	2.1
$\Delta T_c^{\rm GR}$	Transit timing variation due to general relativity	5.1
Δv_r	Relative radial velocity	4.2
$\Delta\hat{v}_r$	Model estimation of relative radial velocity	4.2
Δv_0	Radial velocity offset	4.2
$\Delta_{\rm ei}$	Einstein delay due to the relative velocity between the SSB to the TSB	3.2
$\Delta_{\rm eS}$	Einstein delay in the solar system	3.2
$\Delta_{\rm eT}$	Einstein delay in the target system	3.2
$\Delta_{\rm geo}$	Time delay due to geometric effects	3.2
$\Delta_{\rm hydro}$	Hydrostatic component in tropospheric delay	3.2
$\Delta_{\rm is}$	Time delay in interstellar medium	3.2

Table 2
(Continued)

Acronym or Symbol	Meaning	Sections
$\Delta_{\rm pS}$	Parallax delay in the solar system	3.2
$\Delta_{\rm pT}$	Parallax delay in the target system	3.2
$\Delta_{\rm sS}$	Shapiro delay in the solar system	3.2
$\Delta_{\rm sT}$	Shapiro delay in the target system	3.2
$\Delta_{\rm rS}$	Roemer delay in the solar system	3.2
$\Delta_{\rm rT}$	Roemer delay in the target system	3.2
$\Delta_{\rm S}$	Time delay in the solar system	3.2
$\Delta_{\rm T}$	Time delay in the target system	3.2
$\Delta_{\rm tropo}$	Tropospheric delay	3.2
$\Delta_{\rm vp}$	Vacuum propagation delay due to the light travel between TSB and SSB	3.2
$\Delta_{\rm wet}$	Wet component in tropospheric delay	3.2
λ_e	Wavelength of light when emitted	3.4.1
λ_o	Wavelength of light when observed	3.4.1
η	Projection of $\boldsymbol{r}_{\rm OT}$ on $\boldsymbol{q}_b$	2.1
Θ	Elevation angle	3.2.1
$\boldsymbol{\mu}$	$\boldsymbol{p}_b\mu_\alpha^b + \boldsymbol{q}_b\mu_\delta^b$; Total proper motion of the TSB at the reference time t_0	2.1
μ_α^b	Proper motion in R.A. of the TSB at the reference time t_0	2.1
μ_δ^b	Proper motion in decl. of the TSB at the reference time t_0	2.1
μ_r^b	$v_r^b\,\widetilde{\omega}^b/A$; Proper motion equivalent of radial velocity at the reference time t_0	2.1
ν_e	Frequency of light when emitted	3.4.1
ν_o	Frequency of light when observed	3.4.1
ξ	Projection of $\boldsymbol{r}_{\rm OT}$ on $\boldsymbol{p}_b$	2.1
τ_e	Proper time of light emission	3.2
τ_o	Proper time of light arrival at the observatory	3.2
τ_p	Proper time of periastron	3.2
ω	Argument of periastron of the target star with respect to the TSB	2.3
ω_0	Argument of periastron at a reference time in post-Newtonian models	2.3
$\tilde{\omega}^b$	Annual parallax of the TSB at the reference time t_0	2.1
$\omega_{\rm C}$	Argument of periastron of the barycentric orbit of the companion star	2.3
$\omega_{\rm T}$	Argument of periastron of the barycentric orbit of the target star	2.3
$\dot{\omega}$	Time derivative of ω in the DD model	2.3
Ω	Longitude of ascending node of the barycentric orbit of the target star	2.3

Note. For vectors with opposite signs, only one of them is shown here. The magnitude or length of a vector is denoted by the same symbol but without boldfaced font. Many secondary variables derived from other variables are not shown. Acronyms are shown first and are followed by English and Greek mathematical symbols. For each category, the acronyms or symbols are listed in alphabetic order.

ORCID iDs

Fabo Feng https://orcid.org/0000-0001-6039-0555

References

Abbott, B. P., Abbott, R., Abbott, T. D., et al. 2016, PhRvL, 116, 061102
Abbott, B. P., Abbott, R., Abbott, T. D., et al. 2017, PhRvL, 119, 161101
Arzoumanian, Z., Baker, P., Brazier, A., et al. 2018, ApJ, 859, 47
Auer, L. H., & Standish, E. M. 2000, AJ, 119, 2472

Banik, I., & Zhao, H. 2018, MNRAS, 480, 2660
Barstow, M. A., Bond, H. E., Holberg, J. B., et al. 2005, MNRAS, 362, 1134
Beichman, C., Benneke, B., Knutson, H., et al. 2014, arXiv:1411.1754
Binnendijk, L. 1960, Properties of Double Stars; A Survey of Parallaxes and Orbits (Philadelphia, PA: Univ. Pennsylvania Press)
Blandford, R., & Teukolsky, S. A. 1976, ApJ, 205, 580
Butkevich, A. G., & Lindegren, L. 2014, A&A, 570, A62
Capitaine, N., & Wallace, P. T. 2006, A&A, 450, 855
Capitaine, N., Wallace, P. T., & Chapront, J. 2003, A&A, 412, 567
Catanzarite, J., Shao, M., Tanner, A., Unwin, S., & Yu, J. 2006, PASP, 118, 1319
Catanzarite, J. H. 2010, arXiv:1008.3416
CHIME/FRB Collaboration, Amiri, M., Bandura, K., et al. 2019, Natur, 566, 235
Cosine-100 Collaboration, Adhikari, G., Adhikari, P., et al. 2018, Natur, 564, 83
Damour, T., & Deruelle, N. 1986, Ann. Inst. Henri Poincaré Phys. Théor., 44, 263
Eastman, J., Gaudi, B. S., & Agol, E. 2013, PASP, 125, 83
Eastman, J., Siverd, R., & Gaudi, B. S. 2010, PASP, 122, 935
Edwards, R. T., Hobbs, G. B., & Manchester, R. N. 2006, MNRAS, 372, 1549
Einstein, A. 1916, AnP, 354, 769
Endl, M., Kürster, M., Els, S., Hatzes, A. P., & Cochran, W. D. 2001, A&A, 374, 675
ESA (ed.) 1997, in ESA Special Publication 1200, The HIPPARCOS and TYCHO Catalogs Astrometric and Photometric Star Catalogues Derived from the ESA HIPPARCOS Space Astrometry Mission (ESA: Noordwijk)
Event Horizon Telescope Collaboration, Akiyama, K., Alberdi, A., et al. 2019, ApJL, 875, L1
Fabian, A. C., Iwasawa, K., Reynolds, C. S., & Young, A. J. 2000, PASP, 112, 1145
Fairhead, L., & Bretagnon, P. 1990, A&A, 229, 240
Feng, F., Lisogorskyi, M., Jones, H., et al. 2019, phillippro/pexo: PEXO v1.0.1, Zenodo, doi:10.5281/zenodo.3474037
Feng, F., Tuomi, M., & Jones, H. R. A. 2017, MNRAS, 470, 4794
Folkner, W. M., Park, R. S., & Jacobson, R. A. 2016, Planetary Ephemeris DE435 Tech. Memo. JPL IOM 392R-16-003, (Pasadena, CA: Jet Propulsion Lab.), ftp://ssd.jpl.nasa.gov/pub/eph/planets/ioms/de435.iom.pdf
Folkner, W. M., Williams, J. G., & Boggs, D. H. 2008, The Planetary and Lunar Ephemeris DE 421 Tech. Memo. JPL IOM 343R-08-003, (Pasadena, CA: Jet Propulsion Lab.)
Folkner, W. M., Williams, J. G., Boggs, D. H., Park, R. S., & Kuchynka, P. 2014, IPNPR, 196, 1
Fomalont, E. B., Kopeikin, S., Titov, O., & Honma, M. 2009, in IAU Symp. 261, Relativity in Fundamental Astronomy: Dynamics, Reference Frames, and Data Analysis, ed. S. Klioner, P. K. Seidelmann, & M. Soffel, (Cambridge: Cambridge Univ. Press), 1503
Fomalont, E. B., & Kopeikin, S. M. 2003, ApJ, 598, 704
Gaia Collaboration, Brown, A. G. A., Vallenari, A., et al. 2018, A&A, 616, A1
Gillon, M., Jehin, E., Lederer, S. M., et al. 2016, Natur, 533, 221
González Hernández, J. I., Pepe, F., Molaro, P., & Santos, N. 2018, in Handbook of Exoplanets, ed. H. J. Deeg & J. A. Belmonte (New York: Springer), 883
Greenstein, J. L., Oke, J. B., & Shipman, H. L. 1971, ApJ, 169, 563
Gravity Collaboration, Abuter, R., Amorim, A., et al. 2018, A&A, 615, L15
Grimm, S. L., Demory, B.-O., Gillon, M., et al. 2018, A&A, 613, A68
Gubler, J., & Tytler, D. 1998, PASP, 110, 738
Hobbs, G. B., Edwards, R. T., & Manchester, R. N. 2006, MNRAS, 369, 655
Hohenkerk, C., & Sinclair, A. 1985, The Computation of Angular Atmospheric Refraction at Large Zenith Angles, NAO Tech. Rep. 63, (London: Royal Observatory Greenwich)
Holczer, T., Mazeh, T., Nachmani, G., et al. 2016, ApJS, 225, 9
Holman, M. J., & Murray, N. W. 2005, Sci, 307, 1288
Hulse, R. A., & Taylor, J. H. 1975, ApJL, 195, L51
Ioannidis, P., Schmitt, J. H. M. M., Avdellidou, C., von Essen, C., & Agol, E. 2014, A&A, 564, A33
Irwin, A. W., & Fukushima, T. 1999, A&A, 348, 642
Ivanov, V. D., Cáceres, C., Minniti, D., et al. 2011, EPJ Web Conf., 11, 05008
Johns-Krull, C. M., McCullough, P. R., Burke, C. J., et al. 2008, ApJ, 677, 657
Jordán, A., & Bakos, G. Á. 2008, ApJ, 685, 543
Kervella, P., Mignard, F., Mérand, A., & Thévenin, F. 2016, A&A, 594, A107
Kjeldsen, H., Bedding, T. R., Butler, R. P., et al. 2005, ApJ, 635, 1281
Klioner, S. A. 2003, AJ, 125, 1580
Klioner, S. A., Capitaine, N., Folkner, W. M., et al. 2010, in IAU Symp. 261, Relativity in Fundamental Astronomy: Dynamics, Reference Frames, and Data Analysis, ed. S. A. Klioner, P. K. Seidelmann, & M. H. Soffel (Cambridge: Cambridge Univ. Press), 79
Klioner, S. A., & Kopeikin, S. M. 1992, AJ, 104, 897
Kopeikin, S. M. 1996, ApJL, 467, L93
Kopeikin, S. M., & Makarov, V. V. 2006, AJ, 131, 1471
Kopeikin, S. M., & Makarov, V. V. 2007, PhRvD, 75, 062002
Kopeikin, S. M., & Ozernoy, L. M. 1999, ApJ, 523, 771
Kopeikin, S. M., & Schäfer, G. 1999, PhRvD, 60, 124002
Lelli, F., McGaugh, S. S., Schombert, J. M., & Pawlowski, M. S. 2017, ApJ, 836, 152
Lindegren, L., & Dravins, D. 2003, A&A, 401, 1185
Lindegren, L., Hernández, J., Bombrun, A., et al. 2018, A&A, 616, A2
Lindegren, L., Lammers, U., Hobbs, D., et al. 2012, A&A, 538, A78
Lisogorskyi, M., Jones, H. R. A., & Feng, F. 2019, MNRAS, 485, 4804
Malkov, O. Y., Tamazian, V. S., Docobo, J. A., & Chulkov, D. A. 2012, A&A, 546, A69
Mamajek, E. E. 2012, arXiv:1210.1616
Mangum, J. G., & Wallace, P. 2015, PASP, 127, 74
McCarthy, D. D., & Luzum, B. J. 2003, CeMDA, 85, 37
McCarthy, D. D., & Petit, G. 2004, ITN, 32, 1
Mignard, F., & Klioner, S. A. 2010, in IAU Symp. 261, Relativity in Fundamental Astronomy: Dynamics, Reference Frames, and Data Analysis, ed. S. A. Klioner, P. K. Seidelmann, & M. H. Soffel (Cambridge: Cambridge Univ. Press), 306
Milgrom, M. 1983, ApJ, 270, 365
Miralda-Escudé, J. 2002, ApJ, 564, 1019
Misner, C. W., Thorne, K. S., Wheeler, J. A., & Kaiser, D. I. 1973, Gravitation (Princeton, NJ: Princeton Univ. Press)
Moe, M., Kratter, K. M., & Badenes, C. 2019, ApJ, 875, 61
Murray, C. D., & Correia, A. C. M. 2010, in Exoplanets, ed. S. Seager (Tucson, AZ: Univ. Arizona Press), 15
Niell, A. E. 1996, JGR, 101, 3227
Nilsson, T., Böhm, J., Wijaya, D. D., et al. 2013, in Atmospheric Effects in Space Geodesy, ed. J. Böhm & H. Schuh (Berlin: Springer), 73
Nordtvedt, K., Jr., & Will, C. M. 1972, ApJ, 177, 775
Perryman, M., Hartman, J., Bakos, G. Á., & Lindegren, L. 2014, ApJ, 797, 14
Petit, G. 2004, in Proc. Journées 2003 Conf., Systèmes Deréférence Spatio-temporels, ed. A. Finkelstein & N. Capitaine (St. Petersburg: IAA), 314
Petit, G., & Luzum, B. 2010, ITN, 36, 1
Plavchan, P., Cale, B., Newman, P., et al. 2018, arXiv:1803.03960
Pound, R. V., & Rebka, G. A., Jr 1959, PhRvL, 3, 439
Pourbaix, D., & Boffin, H. M. J. 2016, A&A, 586, A90
Pourbaix, D., Neuforge-Verheecke, C., & Noels, A. 1999, A&A, 344, 172
Pourbaix, D., Nidever, D., McCarthy, C., et al. 2002, A&A, 386, 280
Psaltis, D. 2004, in AIP Conf. Ser. 714, X-ray Timing 2003: Rossi and Beyond, ed. P. Kaaret, F. K. Lamb, & J. H. Swank (Melville, NY: AIP), 29
Ricker, G. R., Winn, J. N., Vanderspek, R., et al. 2014, JATIS, 1, 014003
Rickman, H. 2001, IAUTB, 24, 13
Rüeger, J. 2002, Refractive Index Formulae for Electronic Distance Measurement with Radio and Millimetre Waves Unisurv Rep. S-68, (Sydney: Univ. New South Wales)
Sana, H., & Evans, C. J. 2011, in IAU Symp. 272, Active OB Stars: Structure, Evolution, Mass Loss, and Critical Limits, ed. C. Neiner (Cambridge: Cambridge Univ. Press), 474
Shapiro, I. I. 1964, PhRvL, 13, 789
Standish, E. 2006, JPL Planetary Ephemerides DE414 Tech. Memo. JPL IOM 343R-06-002, (Pasadena, CA: Jet Propulsion Lab.)
Standish, E. M. 1998, JPL Planetary and Lunar Ephemerides, DE405/LE405 Tech. Memo. IOM 3.12F-98-048, (Pasadena, CA: Jet Propulsion Lab.), ftp://ssd.jpl.nasa.gov/pub/eph/planets/ioms/de405.iom.pdf
Tanaka, Y., Nandra, K., Fabian, A. C., et al. 1995, Natur, 375, 659
Taylor, J. H., & Weisberg, J. M. 1982, ApJ, 253, 908
Taylor, J. H., & Weisberg, J. M. 1989, ApJ, 345, 434
Taylor, J. H., Wolszczan, A., Damour, T., & Weisberg, J. M. 1992, Natur, 355, 132
Thiele, T. N. 1883, AN, 104, 245
Unwin, S. C., Shao, M., Tanner, A. M., et al. 2008, PASP, 120, 38
Viswanathan, V., Fienga, A., Gastineau, M., & Laskar, J. 2017, NSTIM, 108
Wallace, P. T., & Capitaine, N. 2006, A&A, 459, 981
Wang, J., Coles, W., Hobbs, G., et al. 2017, MNRAS, 469, 425
Weisberg, J. M., & Taylor, J. H. 2005, in ASP Conf. Ser. 328, Binary Radio Pulsars, ed. F. A. Rasio & I. H. Stairs (San Francisco, CA: ASP), 25
Wex, N. 2014, arXiv:1402.5594
Whitmore, J. B., & Murphy, M. T. 2014, MNRAS, 447, 446
Winn, J. N., Holman, M. J., Torres, G., et al. 2008, ApJ, 683, 1076
Wright, J. T., & Eastman, J. D. 2014, PASP, 126, 838
Zechmeister, M., Kürster, M., Endl, M., et al. 2013, A&A, 552, A78
Zhao, L., Fischer, D. A., Brewer, J., Giguere, M., & Rojas-Ayala, B. 2018, AJ, 155, 24